First-principles Study of Phonon Drag Effect in SiGe Alloys

by

Qian Xu

Submitted to the Department of Mechanical Engineering
in partial fulfillment of the requirements for the degree of

Master of Science in Mechanical Engineering

at the

MASSACHUSETTS INSTITUTE OF TECHNOLOGY

February 2019

© Massachusetts Institute of Technology 2019. All rights reserved.

Signature redacted

Author . . . .
Department of Mechanical Engineering
January 15, 2019

Signature redacted

Certified by . . . .
Gang Chen
Carl Richard Soderberg Professor of Power Engineering
Thesis Supervisor

Signature redacted

Accepted by . . . .
Nicolas Hadjiconstantinou
Chairman, Department Committee on Graduate Theses

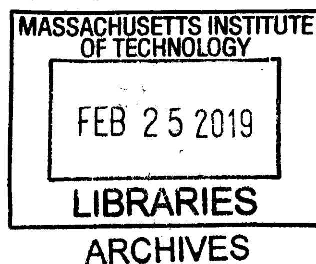

ARCHIVES

77 Massachusetts Avenue
Cambridge, MA 02139
http://libraries.mit.edu/ask

DISCLAIMER NOTICE

Due to the condition of the original material, there are unavoidable flaws in this reproduction. We have made every effort possible to provide you with the best copy available.

Thank you.

The images contained in this document are of the best quality available.

First-principles Study of Phonon Drag Effect in SiGe Alloys

by

Qian Xu

Submitted to the Department of Mechanical Engineering
on January 15, 2019, in partial fulfillment of the
requirements for the degree of
Master of Science in Mechanical Engineering

Abstract

Thermoelectric materials with large figures of merit zT ($zT = \frac{S^2\sigma T}{\kappa}$, where S, T, σ, κ are the Seebeck coefficient, absolute temperature, electrical conductivity and thermal conductivity) are promising candidate materials for efficient solid-state devices for electricity generation, cooling and refrigeration. Over the past decades, there has been great progress in enhancing the zT values of thermoelectric materials above 300K, but not much in thermoelectric performance below room temperature due to the relatively small Seebeck coefficient and high thermal conductivity at low temperatures, which limits the efficiency of thermoelectric coolers and refrigerators.

First discovered in the 1950s, phonon drag effect describes the phenomenon that the Seebeck coefficients of semiconductors are often enormously augmented at low temperatures. More recent works have shown that it can play an important role in many materials' thermoelectric performance even at room temperature. One recent study of silicon has pointed out that the major phonons contributing to phonon drag are with longer mean free path and lower frequency than those carrying heat. Meanwhile, alloying has been found to be an effective tool to enhance thermoelectric performance. The point defects in alloys tend to scatter phonons with short mean free path and high frequency which contribute more to thermal conductivity rather than phonon drag. Therefore, combining phonon drag effect with alloying might be a new approach to design better low-temperature thermoelectric materials. However, most of trial-and-error experiments on optimizing the alloys' composition and doping concentration are very time-consuming and theoretical studies with predictive power are much desired as guidelines. While good progress has been made on first-principles studies on alloys' thermal conductivity, along with a few recent first-principles works on alloying effects on electron mobility, there is little first-principles work done on alloying effect on the Seebeck coefficient, which is another important factor affecting the overall thermoelectric performance, and even less on computing zT within a fully first-principles approach.

In this work, we calculate the Seebeck coefficient, electrical conductivity, thermal conductivity and zT of n-type SiGe alloys with different carrier concentrations (from $10^{15}\,\mathrm{cm}^{-3}$ to $10^{20}\,\mathrm{cm}^{-3}$) over the complete range of compositions within the virtual crystal approximation at 300K and 150K. In particular, we have included the phonon drag part contribution in our Seebeck calculation and taken both alloy scattering of phonons and alloy scattering of electrons into account. We found that phonon drag effect contributes significantly to the total Seebeck coefficient in SiGe alloys, especially at lower temperatures. There are peaks both in the normal (diffusive) part of Seebeck coefficient and the phonon drag part of Seebeck coefficient around the composition of $Si_{0.13}Ge_{0.87}$. The agreement of our calculated results and reported experimental data validates the methodology that we have adopted. Our first-principles calculations with improved accuracy in the Seebeck coefficient is able to predict the thermoelectric properties of typical alloy materials and provide guidelines for the design of better thermoelectric materials utilizing alloying and phonon drag effect.

Thesis Supervisor: Gang Chen
Title: Carl Richard Soderberg Professor of Power Engineering

Acknowledgments

I would like to thank my advisor, Professor Gang Chen, for providing me the great opportunity to work in this top-notch research environment, offering me the precious guidance on how to qualify as a good researcher while being a wonderful role model himself.

I want to express special thanks to my senior labmates Jiawei Zhou and Te-Huan Liu for their patient guidance, without which it would be impossible for me to complete this research work. I would like to thank Qichen Song, Samuel Huberman, Zhiwei Ding, Vazrik Chiloyan, Professor Mingda Li for helpful discussion and also NanoEngineering research group as whole for their great support.

Outside of the lab, I owe debts to Yajing Zhao, Qing Zhang, Zhumei Sun, Thi Mai Anh Nguyen, Carlos A. Ros Ocampo, Liwen Cai, Phillip Ferguson and Prianka Bhatia for being my supportive and caring friends, helping me through my times at MIT.

Last but not the least, I dedicate this thesis to my family for everything they have done for me.

Contents

1 Introduction **19**

1.1 Thermoelectrics 20

1.2 Phonon Drag Effect 22

1.3 SiGe Alloys 24

1.4 Virtual Crystal Approximation 27

1.5 Boltzmann Transport Equation 29

1.6 Thesis Outline 34

2 First-principles Simulation of Transport Properties in SiGe Alloy System **35**

2.1 The Many-body Hamiltonian and Density Functional Theory 36

2.2 Wannier Function-based Interpolation 45

2.3 Electron Calculations 48

2.3.1 Electron Scattering by Phonons 49

2.3.2 Alloy Scattering of Electrons 54

2.3.3 Ionized Impurity Scattering 60

2.4 Phonon Calculations 65

2.4.1 Phonon-phonon Interaction 66

2.4.2 Phonon Scattering by Electrons 70

2.4.3 Alloy Scattering of Phonons 74

2.4.4 Boundary Scattering 77

3 Calculations of Thermoelectric Properties in SiGe Alloys 79

3.1 Electrical Properties 80

3.1.1 Electrical Conductivity and Mobility 80

3.1.2 Diffusive Seebeck Coefficient 85

3.2 Thermal Conductivity 87

3.2.1 Lattice Thermal Conductivity 87

3.2.2 Electronic Thermal Conductivity 94

3.3 Seebeck Coefficient Contributed by Phonon Drag 97

3.3.1 Formula Derivation 97

3.3.2 Validation in Silicon 102

3.3.3 SiGe Alloys Results 103

3.3.4 Convergence Test Results 106

3.4 Thermoelectric Figure of Merit 109

4 Summary and Future Work **115**

4.1 Summary 115

4.2 Future Work 116

List of Figures

1-1 Measured Seebeck coefficient and thermal conductivity of Bi_2Te_3 as functions of temperature [1], where κ_e is estimated from measured electrical conductivity using the Wiedemann-Franz law (see section 3.2), and $\kappa_l = \kappa_{\text{total}} - \kappa_e$. 22

2-1 Calculated electronic band structure of SiGe alloys.The figure in the lower left corner shows the band convergence region (around the composition of $Si_{0.13}Ge_{0.87}$) where the L valley and the valley near X point are aligned. 49

2-2 Fermi-Dirac distribution, where E denotes the electron's energy, E_f denotes the Fermi level. In SiGe alloys, k_BT at room temperature is typically around or smaller than $E_f/200$. 52

2-3 Calculated electron scattering rate by phonons vs. electron energy with respect to conduction band minimum, n denotes the n-type carrier concentration. T = 300K and 150K. (a)(c) of lightly doped n-type SiGe alloys (b)(d) of heavily doped n-type SiGe alloys. 53

2-4 Calculated intervalley and intravalley electron scattering rates by phonons in $Si_{0.15}Ge_{0.85}$ at T = 300K, n-type carrier concentration $n = 1 \times 10^{20}\,cm^{-3}$. The conduction band minimum for silicon is near X valley $[0, 0.85(\frac{2\pi}{a}), 0]$ with $|k| = 0.85(\frac{2\pi}{a})$ and for germanium it is at L valley $[\frac{\pi}{a}, \frac{\pi}{a}, \frac{\pi}{a}]$ with $|k| = 0.866(\frac{2\pi}{a})$, where a denotes the lattice constant. Scattering rates for the electron states with energy out of the range that we consider are not calculated and taken as zero. 55

2-5 Calculated intervalley and intravalley electron scattering rates by phonons vs. electron energy near the band convergence region at T = 300K, n-type carrier concentration $n = 1 \times 10^{20}\,cm^{-3}$. 56

2-6 Alloy-electron scattering rate of SiGe alloys on logarithmic scale and linear scale. 59

2-7 Calculated intervalley and intravalley alloy-electron scattering rates in $Si_{0.2}Ge_{0.8}$. The conduction band minimum for silicon is near X valley $[0, 0.85(\frac{2\pi}{a}), 0]$ with $|k| = 0.85(\frac{2\pi}{a})$ and for germanium it is at L valley $[\frac{\pi}{a}, \frac{\pi}{a}, \frac{\pi}{a}]$ with $|k| = 0.866(\frac{2\pi}{a})$. Scattering rates for the electron states with energy out of the range that we consider are not calculated and taken as zero. 60

2-8 Calculated intervalley and intravalley alloy-electron scattering rates vs. electron energy near the band convergence point. 61

2-9 Definition of $\hbar\beta$, the momentum change resulting from scattering. . . 62

2-10 Calculated ionized impurity scattering rate of lightly doped and heavily doped SiGe alloys both on logarithmic scale and linear scale. n denotes the n-type carrier concentration. 63

2-11 Calculated phonon dispersion of SiGe alloys around the center of the Brillouin zone. 65

2-12 Possible three-phonon interactions involving phonons with wavevectors of $\boldsymbol{q}$, $\boldsymbol{q}'$, $\boldsymbol{q}''$. n denotes the distribution of phonon with wavevector of $\boldsymbol{q}$ at branch λ, so as n' for phonon of $\boldsymbol{q}'\lambda'$, n'' for phonon of $\boldsymbol{q}''\lambda''$. . . 68

2-13 Calculated phonon-phonon scattering rate of SiGe alloys at 300K and 150K. 69

2-14 Calculated mode-weighted Gruneisen parameter vs. alloy composition. 70

2-15 Possible electron-phonon interactions involving phonons with wavevector of $\boldsymbol{q}$ and electrons of wavevectors $\boldsymbol{k}$ and $\boldsymbol{k}'$. 71

2-16 Calculated phonon scattering rate by electrons vs. phonon frequency, n denotes the n-type carrier concentration. T = 300K and 150K. (a)(c) of lightly doped n-type SiGe alloys (b)(d) of heavily doped n-type SiGe alloys. 73

2-17 Phonon scattering rate due to mass disorder of SiGe alloys. 76

3-1 Mobilities of SiGe alloys at 300K. Electron-phonon scattering, alloy-electron scattering and ionized impurity scattering are considered. . . 82

3-2 Calculated mobilities of SiGe alloys at four different carrier concentrations at 150K. Electron-phonon scattering, alloy-electron scattering and ionized impurity scattering are considered. 83

3-3 Mobilities of Ge and $Si_0.2Ge_{0.8}$ vs. doping concentration at 300K. The experimental data for germanium is from [2], the experimental data for $Si_{0.2}Ge_{0.8}$ is from [3]. 84

3-4 Calculated lattice thermal conductivity of SiGe alloys at four different carrier concentrations at 300K compared to experiments [3, 4]. 89

3-5 Calculated lattice thermal conductivity at four different carrier concentrations of SiGe alloys at 150K. 90

3-6 Reduction in SiGe alloys' lattice thermal conductivity in terms of percentage due to electron-phonon interaction. 91

3-7 Accumulated lattice thermal conductivity vs. phonon mean free path in lightly doped and heavily doped SiGe alloys. (a)(b)T = 300K, (c)(d) T = 150K. The y-axis is cut and the maximum value is set to $30W/mK$ to show the difference between the curves of alloys at different temperatures and different doping concentrations more clearly. 92

3-8 Phonon mean free path determined by intrinsic phonon scattering, alloy-phonon scattering and electron-phonon scattering vs. phonon frequency, taking $Si_{0.1}Ge_{0.9}$ as an example. 93

3-9 Intrinsic phonon scattering rate, alloy-phonon scattering rate and electron-phonon scattering rate vs. phonon frequency, taking $Si_{0.1}Ge_{0.9}$ as an example. 94

3-10 Thermal conductivity (including the electronic part) of SiGe alloys at 300K compared to experiments [3, 4] 96

3-11 Seebeck coefficient of silicon ($n = 2.75 \times 10^{14}\,\mathrm{cm}^{-3}$) as a function of temperature. The experimental data is from [5]. 103

3-12 Calculated Seebeck coefficients of SiGe alloys vs. composition. The experimental data is from [6]. (a)(b)T = 300K, (c)(d) T =150K. . . . 104

3-13 Density of states of SiGe alloys in the band convergence region. At $Si_{0.87}Ge_{0.13}$ the density of states is the highest. 106

3-14 Calculated lattice thermal conductivity vs. sampling mesh density . . 107

3-15 Calculated mobility vs. sampling mesh density for lightly doped and heavily doped SiGe alloys. (a)(b)T = 300K, (c)(d) T = 150K. 108

3-16 Calculated diffusive part of Seebeck coefficient vs. sampling mesh density for lightly doped and heavily doped SiGe alloys. (a)(b)T = 300K, (c)(d) T = 150K. 109

3-17 Calculated phonon drag part of Seebeck coefficient vs. sampling mesh density for lightly doped and heavily doped SiGe alloys. (a)(b)T = 300K, (c)(d) T = 150K. 110

3-18 Calculated zT values of SiGe alloys vs. composition at four different carrier concentrations. (a) T = 300K, the experimental data is from [3], (b) T = 150K. 111

3-19 Calculated zT values of SiGe alloys vs. composition, at carrier concentration of $10^{19}\,\text{cm}^{-3}$ and $10^{20}\,\text{cm}^{-3}$, with and without phonon drag. (a)(b) T = 300K, (a)(b) T = 150K. 112

List of Tables

2.1 Approximations (exchange-correlation functionals) 41

2.2 Possible electron-phonon scattering events for an electron 50

2.3 Possible electron-phonon scattering events for a phonon 70

2.4 Characteristic lengths used in boundary scattering calculations 77

Chapter 1

Introduction

The global demand for energy output keeps growing as our society develops. As the dominant and traditional energy resource, fossil fuels are non-renewable and combustion of them produces waste heat which means a large portion of energy input into different industries is lost. In addition to the waste heat, fuel burning is harmful to the environment as it releases a large amount of greenhouse gases to the atmosphere. Sustainable development requires renewable energy sources and energy recycling techniques that are environmentally-friendly and energy-efficient.

Thermoelectric devices can directly convert heat into electricity as well as electrical power into cooling or heating. The former conversion can help recover some of the lost energy in the fuel burning process and the latter can be used for low-temperature applications (e.g. refrigeration). Compared with conventional refrigeration, thermoelectric devices feature no moving part or environmentally unfriendly refrigerant, invulnerability to leaks, long life time, rapid response time, accurate and constant temperature control, portability, and flexible shape that can accommodate to smaller or more severe environments.

1.1 Thermoelectrics

Thermoelectric materials can realize the direct conversion between heat and electricity based on the thermoelectric effects caused by temperature difference or current flow. The most important two thermoelectric effects are the Seebeck effect and the Peltier effect.

Named after the Baltic German physicist Thomas Johann Seebeck for his findings of a circuit made from two dissimilar metals, with junctions at different temperatures would deflect a compass magnet [7], the Seebeck effect can be understood as follows. When a temperature gradient is applied to a material in an open circuit, the charge carriers at the hot side have larger kinetic energy and travel faster than the charge carriers at the cold side. The high-energy carriers diffuse from the hot side to the cold side and this forms a net electric current within the material. As the charge carriers accumulate at the cold side, an electric field will be formed and the drift current induced by this electric field will finally balance out the one generated by the temperature gradient. By this means, the Seebeck coefficient S is defined locally as the ratio of the generated electric field E_{emf} to the temperature gradient ∇T when these two electric currents are balanced out: $E_{\mathsf{emf}} = -S\nabla T$.

Named after the French physicist Jean Charles Athanase Peltier for his discovery of an electrical current would produce heating or cooling at the junction of two dissimilar metals [8], the Peltier effect is the underlying principle of thermoelectric cooling. As the electricity carriers carry charge as well as heat, an electric current passing through the material will generate a heat current, which can be regarded as the reverse phenomenon of the Seebeck effect. Similarly, the Peltier coefficient Π is defined as the ratio of the induced heat current J_q to the electric current J as $J_q = \Pi J$, representing how much heat is carried per unit charge. The second Thomson relation gives $\Pi = TS$, which can be proven using Onsager reciprocal relation [9, 10] for a time-reversal symmetric material, we will also prove this in chapter 3 where we derive the expressions of the normal (diffusive) Seebeck coefficient and of the normal Peltier

coefficient. The ability of a given material at a given absolute temperature T to efficiently convert heat to electricity or vice versa is related to its dimensionless figure of merit zT given by

$$zT = \frac{S^2 \sigma T}{\kappa} \tag{1.1}$$

where S is the Seebeck coefficient, σ is the electrical conductivity and κ is the thermal conductivity. The thermal conductivity could be divided into two parts, $\kappa = \kappa_l + \kappa_e$, where κ_e denotes the electronic thermal conductivity and κ_l denotes the lattice thermal conductivity (more details will be discussed in section 3.2). The maximum thermoelectric energy conversion efficiency of a thermoelectric material is expressed as [11]

$$\eta = \left(\frac{T_H - T_C}{T_H}\right) \cdot \frac{\sqrt{z\bar{T}+1}-1}{\sqrt{z\bar{T}+1}+T_C/T_H} \tag{1.2}$$

with T_H and T_C are the absolute temperatures of the hot side and the cold side, and $\bar{T} = \frac{T_H+T_C}{2}$. It should be noticed that equation (1.2) assumes constant materials properties (S, σ and κ) [12, 13] at different temperatures that zT is assumed to have the same value ($z\bar{T}$) along the direction of the thermal gradient in the thermoelectric material. However, this approximation is not valid when the temperature gradient is large or the material properties are strongly temperature-dependent. Anyway, equation (1.2) makes it clear that high zT materials are needed to make efficient solid-state devices for heat-to-electricity conversion, cooling and refrigeration.

The past decades have seen excellent progress in enhancing the zT values of thermoelectric materials above 300K [11, 14, 15, 16], but not much in thermoelectric performance below room temperature due to the relatively small Seebeck coefficient and high thermal conductivity at low temperatures. This is due to, as figure 1-1 shows the case of bismuth telluride, the Seebeck coefficients of materials usually decreases as the temperature gets lower for there are less high-energy charge carriers. The lattice thermal conductivity, which is the dominant part of the total thermal conductivity in most of thermoelectric materials, goes higher at lower temperatures (but not ex-

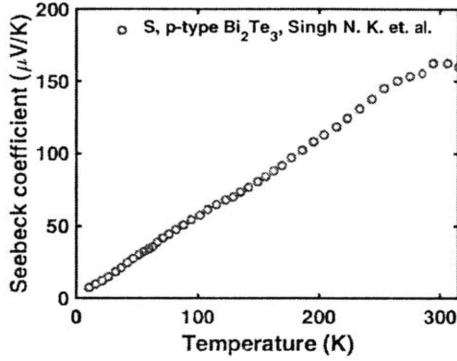

(a) Seebeck coefficient [1]

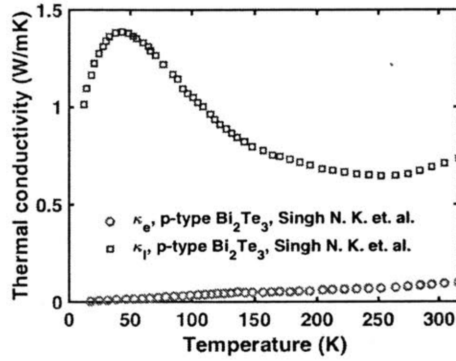

(b) Thermal conductivity [1]

Figure 1-1: Measured Seebeck coefficient and thermal conductivity of Bi_2Te_3 as functions of temperature [1], where κ_e is estimated from measured electrical conductivity using the Wiedemann-Franz law (see section 3.2), and $\kappa_l = \kappa_{\text{total}} - \kappa_e$.

tremely low for at very low temperatures there will be less phonons and the lattice thermal conductivity will be reduced) since intrinsic phonon-phonon interaction is weaker at lower temperatures. Those together limit the efficiency of thermoelectric coolers and refrigerators.

1.2 Phonon Drag Effect

Phonon drag effect describes the phenomenon first discovered in the 1950s [17] that the Seebeck coefficients of many non-magnetic semiconductors are often enormously augmented at low temperatures (the Kondo effect [18] that involves scattering of conduction electrons due to magnetic impurities can also lead to an increase in the Seebeck coefficient below certain temperature [19], which will not be discussed in our work). The previous diffusive picture in section 1.1 where we introduced the Seebeck effect does not consider the phonons flowing between the two ends. However, as long as there is a temperature gradient, there are phonons travelling from the hot side to the cold side. During this process, phonons and electrons would interact with each other and part of phonons' momentum will transfer to electrons. Electrons would gain extra momentum from phonons in the forward direction and be able to travel

from the hot side to the cold side, contributing to extra current to be balanced out by the generated electric field, and therefore increasing the Seebeck coefficient. The extra part of the Seebeck coefficient is dubbed as the phonon drag part of Seebeck for it is like the phonons that are travelling forward drag the electrons to travel with them [17]. This phonon drag part is particularly important and would increase the Seebeck coefficient of thermoelectric materials dramatically at low temperatures since the phonon-phonon interaction will be weak and phonons could transfer more momentum to electrons. However, not all materials would have significant phonon drag effect. To have a large phonon drag effect, phonons in the material should not be strongly scattered and should have long mean free path, while the electron-phonon interaction should be strong. For example, phonons in Bi_2Te_3 are intrinsically heavily scattered due to the complex crystal structure and the heavy atoms, which leads to the low thermal conductivity. Plus the electron-phonon coupling in Bi_2Te_3 is proven to be weak [20], there is little phonon drag effect in Bi_2Te_3 as shown in figure 1-1.

More recent experimental works have shown that phonon drag effect can play an important role in many materials thermoelectric performance even at room temperature [21, 22, 23, 24]. Early theoretical works [25, 26, 17, 27] tried to quantitatively determine the phonon drag contribution by solving the coupled electron-phonon Boltzmann transport equations using a variational approach [25] and reasonable agreements with experiments were achieved [28, 29]. However, the calculations adopted simplified scattering models where there were a number of adjustable parameters and the variational method was limited to the lowest orders of the trial functions. All these impaired their predictive power. Another approach to solve the coupled electron-phonon Boltzmann transport equations is to partially decouple the electron and the phonon transport [30]. Compared with the variational method, it gives better interpretation of the results in terms of contributions from different phonon modes. Recently, this approach has been applied to bulk silicon and achieved good agreements with experiments. Mahan et al. [31] incorporated the accurate phonon-phonon scattering rates obtained from first-principles calculation and the electron-phonon scattering rates

calculated using the adjustable material-dependent parameters (deformation potentials) into the model at low carrier concentrations. Zhou et al. [32] further enhanced the predictive power by obtaining the electron-phonon scattering rates from first-principles calculation without any adjustable parameters at several temperatures and carrier concentrations. They pointed out that the major phonons contributing to the phonon drag are with longer mean free path and lower frequency than those carrying heat, and suggested if proper filtering of phonons can be designed, it is possible to lower the thermal conductivity and increase the Seebeck coefficient simultaneously by utilizing phonon drag effect at low temperatures.

1.3 SiGe Alloys

Alloying has been found to be an effective tool to enhance thermoelectric performance and the key idea is to enhance the electrical to thermal conductivity ratio by a selective scattering on phonons that scatters phonons more effectively than electrons (or holes). The large mass contrast in alloys serves as scattering centers and disrupts the phonon transport in the material and therefore reduce the lattice thermal conductivity [33, 34]. This strategy has been applied to a wide variety of traditional thermoelectric materials including BiSbTe alloys for room-temperature use, PbTeSe alloys for moderate-temperature use, and the SiGe alloys for high-temperature use [34]. A recent study of Pei et al. [35] has also shown that alloying is able to converge the valence or conduction bands to achieve high valley degeneracy, and the high density of states near the Fermi level can enhance the power factor .

Similar to Rayleigh scattering, it is well understood that the atom-size point defects in alloys tend to scatter phonons with short wavelength which are typically of high frequency, and according to Zhou et al. [32], those are the phonons contributing more to thermal conductivity rather than phonon drag. As Klemens [36] pointed out that in semiconductors, only phonons below certain frequency are considered to

interact with electrons and one can optimize the figure of merit by introducing point defects that scatter high-frequency phonons to reduce the lattice thermal conductivity while phonon drag would not be much affected, we think alloying might be able to filter the phonons that contribute more to the thermal conductivity while retaining the phonons that contribute to phonon drag. Though phonon drag effect has been studied in many alloys [37, 38, 39], almost all of those alloy systems are metal alloys and are of little practice use for thermoelectrics. Also, as said in the last section, the most studied thermoelectric material for low-temperature (around and below room temperature) use, Bi_2Te_3 and its common alloy BiSbTe, do not exhibit large phonon drag effect. Since phonon drag was first seen in germanium at low temperatures and theoretically explained by Herring [17], as well as it has been shown that phonon drag effect is large in silicon even at room temperature [31, 32], we think SiGe alloys should be a suitable system for us to study to see if the method above will be effective in enhancing the Seebeck coefficient and lowering the thermal conductivity simultaneously in the materials with significant phonon drag effect.

SiGe alloys are relatively well-studied thermoelectric materials that feature high reliability, abundance of elements and non-toxicity. NASA uses SiGe alloys on Radioisotope Thermoelectric Generators (RTGs) operating from 600-1000 °C for space missions [34]. Early measurements of mobility in p-type SiGe alloys were reported by Levitas [40] and n-type by Glicksman [41] in 1955. The thermal conductivity was first measured by Joffe et al. [42], Steele et al. [4] and Abeles et al. [43] in 1950s and early 1960s. The Seebeck coefficient was first measured by Steele et al. in 1958 [4] and later SiGe alloys have become the established material for high temperature power generation applications. In the 1960s and 1970s, studies were carried out on the grain size effect on the lattice thermal conductivity in fine-grained SiGe alloys [44, 45, 46]. The study on the grain boundary scattering in SiGe alloys has been further pushed forward by more recent studies on the thermoelectric properties in SiGe nanocomposites [47, 48], which show that the increased phonon scattering at the grain boundaries of the nanostructures leads to a large reduction of thermal conductivity.

More information of SiGe alloys including preparation methods, mechanical properties, more detailed development of SiGe thermoelectrics from the earliest research efforts at RCAs Princeton Laboratory to the use in more recent space applications can be found in reviews by Rosi [49, 50], Bhandari and Rowe [51], Rowe [52] and Wood [53].

Most of trial-and-error experiments on finding and optimizing alloy recipes for thermoelectric use are very time-consuming. To make the screening and optimizing processes more efficient, guidelines on optimizing the alloys' composition and doping concentration are much desired. The first-principles methods within the virtual crystal approximation that will be introduced in more detail in the next section and chapter 2, have been used to study alloys' electronic band structure since the late 1980s [54]. Electronic band structure provides important information (e.g. band gap, effective mass) that determines many of materials' electrical properties, thus obtaining alloys' band structures using first-principles methods can give useful insights into their thermoelectric performance. Recent first-principles studies [55, 56, 57, 32] that incorporates theories of scattering mechanisms for electrons and phonon, are able to calculate materials' transport properties (in particular, the thermal conductivity, the Seebeck coefficient, the electrical conductivity) based on Boltzmann transport equations. First-principles thermal transport calculations that take phonon-phonon interaction, electron-phonon interaction, grain size effect and effect of alloying into account have gained success in obtaining results with accuracy comparable to experiments [55, 58, 32, 59]. In comparison with the first-principles calculations for thermal transport, calculations of electrical transport in semiconductors have only received attention recently and so far only a few materials (e.g. silicon, SiGe, phosphorene, MoS_2, GaAs, BP, BAs, BSb) are calculated within a fully first-principles approach for the electrical transport properties [56, 57, 60, 61, 62, 32, 63, 64, 65]. These works demonstrate the inclusion of carrier scattering by equilibrium phonons, carrier scattering by polar optical phonons, scatterings due to impurities and alloying, as well as the phonon drag effect. One of the biggest challenges in electrical transport first-

principles calculations for more materials is to obtain more accurate electronic band structures (e.g. extra care is needed when dealing with spin-orbit coupling for heavy elements) with reasonable computational cost. More advanced quantum chemistry methods (e.g. GW calculation [66, 67]) than the current density functional theory (DFT) method are being developed but so far are still much less popular than the DFT method due to their heavy computational load. In the case of SiGe alloys, several first-principles works [56, 57, 55, 59] using the virtual crystal approximation (which is adopted in our work) have achieved good agreement with the early experiments mentioned in the last paragraph. This shows that the VCA method works well for the SiGe alloys system on thermal transport calculation [55, 59] and electron transport calculation [56, 57]. These above give us the confidence to study the phonon drag effect in SiGe alloys system using first-principles methods to exam if the method of combining phonon drag and the alloying will be effective in enhancing the thermoelectric properties.

1.4 Virtual Crystal Approximation

To simulate a non-alloy system, by that we mean a real single-crystal material, we always start our calculation by constructing its unit cell that has atoms of particular elements that can be found on periodic table. All calculations can be performed on the unit cell through the use of periodic boundary conditions (such as the Block theorem) to represent the entire crystal. However, in a real alloy material, the arrangement of atoms is usually not ordered. Atoms of different elements could sit randomly on the lattice sites and there can be defects like vacancies, interstitial atoms and dislocations that break the periodicity of the structure and no longer allow the simulation of the system with a simple unit cell. It would require very large supercell to capture all these disorders and hence drastically increase the computation complexity. Unfortunately, the first-principles calculations using this kind of supercells are extremely heavy and current computing power cannot handle such daunting tasks.

Right now, one of the most widely-used and computationally practical approaches to deal with alloys is the virtual crystal approximation (VCA) [68, 33]. First proposed by Nordheim [68], VCA treats the actual alloy system as a superposition of two parts: (1) the virtual single-crystal with perfect periodicity, composed of fictitious virtual atoms that interpolate between the behavior of the atoms in the parent materials, and (2) a random part to account for the difference between the actual crystal potential and the virtual crystal potential at lattice points. Early theoretical work applied VCA to electronic band calculation, as well as phonon scattering due to anharmonicity and mass disorder [69, 33, 70]. With the development of computational power, VCA has been adopted to study alloy materials in density functional theory calculations since the late 1980s [54].

Despite of its advantages of simplicity and computational efficiency, we need to be very careful about its use for it may not apply to every alloy system. As described above, VCA does not deal with the crystal defects like vacancies, interstitial atoms and dislocations. The disorder is only treated as a first-order perturbation (single scattering) despite the presence of possible large impurity concentration, which might or might not work satisfactorily depending on the complexity of the system. For instance, Mendoza et al. [71] studied the elastic phonon scattering in SiGe alloys and examined the validity of the VCA for phonon heat conduction using the Green's function approach. The Green's function approach allows inclusion of the resonant effect that stems from the constructive interference of the multiple scattering processes in a system with impurities while these multiple scattering processes are not taken into account in the VCA approach. The calculated density of states of phonon is distinctly different from that of the VCA approximation at high frequencies. However, at these high frequencies, the lifetimes obtained for these phonon modes are small in both the full scattering theory and the VCA, resulting in their negligible contribution to thermal transport. Several first-principles studies [56, 57, 55, 59] have also shown that the VCA method works well for the calculations of SiGe alloys' thermal conductivity and electron mobility. This indicates that the VCA method captures the phonons' and

the electrons' dynamics in SiGe alloys reasonably well in term of describing thermal transport and electron transport. Therefore, we like to expand this methodology to calculate the Seebeck coefficients (including the contribution from phonon drag) of SiGe alloys.

We follow Abeles' work [33] to construct our virtual SiGe alloy systems and determine the atomic masses and the pseudopotentials by interpolating between the masses and the pseudopotentials of the parent elements silicon and germanium. The $\mathrm{Si}_x\mathrm{Ge}_{1-x}$ alloy system is generated by compositionally averaging the masses and the pseudopotentials of Si and Ge as below

$$m_{\mathrm{vca}} = xm^{\mathrm{Si}} + (1-x)m^{\mathrm{Ge}} \tag{1.3}$$

The averaging of pseudopotentials can be done using the virtual.x program in QUANTUM ESPRESSO [72] package, which is doing

$$V_{\mathrm{vca}} = xV^{\mathrm{Si}} + (1-x)V^{\mathrm{Ge}} \tag{1.4}$$

We also interpolate the lattice constants in the same way. However, in practice, we relax the lattice parameters once we have determined the atomic masses and the pseudopotentials using the linearly-interpolated values as initial input. The final relaxed lattice constants are used in our calculations.

1.5 Boltzmann Transport Equation

In this work, transport properties of materials are studied based on Boltzmann transport equation. Devised by Ludwig Boltzmann in 1872, Boltzmann transport equation describes dilute gases where only binary collisions are considered at the kinetic level so it is not valid for dense fluids such as liquids. It also has found applications

in fields involving dilute carrier mediated transport like the ones of electron gases, phonon gases and photon gases. The original Boltzmann transport equation tracks the number of the particles in one-particle phase space and does not include explicitly wave effects such as interference or tunneling so it is applicable to classical system only. Extension to quantum system requires special treatment [73]. Despite these restrictions, Boltzmann transport equation is powerful and can be applied to a wide range of problems from nanoscale to macroscale [74].

More specifically, Boltzmann transport equation characterizes all the particles' motion in the system using the single particle distribution $f(\boldsymbol{r}, \boldsymbol{p}, t)$ in the phase space made of the particle's real-space position $\boldsymbol{r}$, momentum $\boldsymbol{p}$ and time t. And the single particle distribution $f(\boldsymbol{r}, \boldsymbol{p}, t)$ is the expected number of particles in a differential phase space element located at $(\boldsymbol{r}, \boldsymbol{p})$ at time t. The particle's changing states can be caused by the external forces along their trajectories, or more generally, the potential gradients acting on the particle as well as the scattering events, i.e., the interaction between particles.

We will use velocity $\boldsymbol{v}(\boldsymbol{p} = m\boldsymbol{v})$ or wavevector $\boldsymbol{k}(\boldsymbol{p} = \hbar\boldsymbol{k})$ rather than momentum $\boldsymbol{p}$ below. In this way, the general form of Boltzmann transport equation is [74]

$$\frac{\partial f}{\partial t} + \boldsymbol{v} \cdot \nabla_{\boldsymbol{r}} f + \frac{\boldsymbol{F}}{\hbar} \cdot \nabla_{\boldsymbol{k}} f = \left(\frac{\partial f}{\partial t}\right)_{\text{coll}} \tag{1.5}$$

where $\boldsymbol{F}(\boldsymbol{r}, t)$ is the external force (i.e., not due to other particles) on the particle. For example, $\boldsymbol{F} = q\boldsymbol{E}$ where q is the charge of the electron when the particle is the electron in an electric field $\boldsymbol{E}$, and $F = 0$ when the particle is the phonon since there is no external force for the phonon. The terms on the left-hand side include the evolution of f with respect to t, $\boldsymbol{r}$ and $\boldsymbol{k}$, which are balanced out by the collision term on the right hand side that represents the net gain of the particle in one quantum state due to scattering events. The collision term lumps the interaction of this one particle with the rest of the particles in the system and it represents the non-conserving nature of the single particle distribution. While collision is a time-dependent process

and the rigorous way of dealing with it is to solve the time-dependent Schrödinger equation, this approach is usually extremely complicated and not practical. An easier way is to use the perturbation method [75] that considers the time-dependent interaction between the particles as a small perturbation in energy. Take the two-particle interaction as an example, the total system Hamiltonian H is represented as $H = H_0(\boldsymbol{r}) + H'(\boldsymbol{r}, t)$, where $H'(\boldsymbol{r}, t)$ is the small perturbation from the original steady-state, non-interacting unperturbed Hamiltonian $H_0(\boldsymbol{r})$ of the two particles. In this way, the solution of the Schrödinger equation with the new Hamiltonian H can be obtained through the perturbation method and expressed in terms of the wavefunction Φ of the unperturbed Hamiltonian H_0. Using the perturbation solution, the transition rate (probability of transition per unit time) from one quantum state Φ_i to another quantum state Φ_f is given by Fermi's golden rule

$$W_i^f = \frac{2\pi}{\hbar} \left| \int \Phi_f^* H' \Phi_i d^3\boldsymbol{r} \right|^2 \delta(\epsilon_f - \epsilon_i) \tag{1.6}$$

where $d^3\boldsymbol{r}$ means integration over the whole volume of the system and the delta function $\delta(\epsilon_f - \epsilon_i)$ manifests the requirement of energy conservation. In fact, depending on the detailed scattering mechanism, before and after the scattering event, the momentum, or the energy, or both, of the system should conserve. For instance, electron scattering by ionized impurity is an elastic process, i.e. the energy of the electron does not change after the scattering event happens, while the momentum of it could change. For electron-phonon scattering, the total energy of the electrons and the phonons involved should conserve: the energy of the phonon that participates in the electron-phonon interaction should equal the energy difference between the electron's initial state and final state. The crystal momentum conserves only when the wavevector of the final state is within the first Brillouin zone: the wavevector of the phonon connects the initial wavevector and the final wavevector of the electron that being scattered (known as the normal process [76]). If the wavevector of the final state falls outside the first Brillouin zone, it will be mathematically folded back to the first Brillouin zone by some reciprocal-lattice vector and in this case the crystal momentum

is not conserved (known as the Umklapp process [76]). As will be discussed in more detail in chapter 2, these above introduce a restriction on the phonon wave vector and energy, and search for conditions that meet these conservations is required in our first-principles calculations.

According to Fermi's golden rule, the collision term can be evaluated using the scattering probability of the particle by summing over all the initial states and final states. Again, take the two-particle scattering process as an example. the initial wavevector and distribution function of one particle are $\boldsymbol{k}$, $f(t, \boldsymbol{r}, \boldsymbol{k})$ and it collides with another particle with the wavevector $\boldsymbol{k}_1$ and distribution function $f(t, \boldsymbol{r}_1, \boldsymbol{k}_1)$. After the scattering, the wavevectors and distribution functions become $\boldsymbol{k}'$, $f(t, \boldsymbol{r}', \boldsymbol{k}')$ and $\boldsymbol{k}_1'$, $f(t, \boldsymbol{r}_1', \boldsymbol{k}_1')$. The scattering term for the particle at state $\boldsymbol{k}$ can be expressed as

$$\begin{aligned}
\left(\frac{\partial f}{\partial t}\right)_{\text{coll}} =& - \sum_{\boldsymbol{k}_1, \boldsymbol{k}', \boldsymbol{k}_1'} f(t, \boldsymbol{r}, \boldsymbol{k}) f(t, \boldsymbol{r}, \boldsymbol{k}_1) W(\boldsymbol{k}, \boldsymbol{k}_1 \rightarrow \boldsymbol{k}', \boldsymbol{k}_1') \\
&+ \sum_{\boldsymbol{k}_1, \boldsymbol{k}', \boldsymbol{k}_1'} f(t, \boldsymbol{r}, \boldsymbol{k}') f(t, \boldsymbol{r}, \boldsymbol{k}_1') W(\boldsymbol{k}', \boldsymbol{k}_1' \rightarrow \boldsymbol{k}, \boldsymbol{k}_1) \\
=& - \frac{V^3}{(2\pi)^9} \int f(t, \boldsymbol{r}, \boldsymbol{k}) f(t, \boldsymbol{r}, \boldsymbol{k}_1) W(\boldsymbol{k}, \boldsymbol{k}_1 \rightarrow \boldsymbol{k}', \boldsymbol{k}_1') d^3\boldsymbol{k}_1 d^3\boldsymbol{k}' d^3\boldsymbol{k}_1' \\
&+ \frac{V^3}{(2\pi)^9} \int f(t, \boldsymbol{r}, \boldsymbol{k}') f(t, \boldsymbol{r}, \boldsymbol{k}_1') W(\boldsymbol{k}', \boldsymbol{k}_1' \rightarrow \boldsymbol{k}, \boldsymbol{k}_1) d^3\boldsymbol{k}_1 d^3\boldsymbol{k}' d^3\boldsymbol{k}_1'
\end{aligned} \tag{1.7}$$

where the $\frac{V^3}{(2\pi)^9}$ term is the factor that converts the summation over wavevector into integration over the phase space. The minus terms indicate the particle is being scattered out of the state to some other state and the plus terms indicate the particle is being scattered into this state from some other state.

However, this integral-differential equation (1.7) is very difficult to solve. A widely used simplification is the relaxation time approximation (RTA) that characterizes the scattering event by the relaxation time τ, which is a measure of how long it takes for a nonequilibrium system to relax back to an equilibrium distribution.

$$\left(\frac{\partial f}{\partial t}\right)_{\text{coll}} = -\frac{f - f^0(T, \varepsilon, \varepsilon_f)}{\tau(\varepsilon)} \tag{1.8}$$

ε is the energy of the state and ε_f is the chemical potential, f^0 represents the equilibrium distribution of the particles, such as Fermi-Dirac distribution ($f^0 = \frac{1}{e^{(\varepsilon-\varepsilon_f)/k_BT}+1}$, will be shown in figure 2-2) for electrons and Bose-Einstein distribution ($n^0 = \frac{1}{e^{\varepsilon/k_BT}-1}$) for phonons. Relaxation time approximation is a mean-field approximation and it assumes isotropic scattering for a given energy. For elastic scattering, it is valid for low-field transport. Despite for the limitation, it is used widely even for processes including inelastic scattering, with correct end results for most situations [74].

Denote $g = f - f^0$, we rewrite the Boltzmann transport equation under the relaxation time approximation [74]

$$\frac{\partial g}{\partial t} + \frac{\partial f^0}{\partial t} + \boldsymbol{v} \cdot \nabla_{\boldsymbol{r}} f^0 + \boldsymbol{v} \cdot \nabla_{\boldsymbol{r}} g + \frac{\boldsymbol{F}}{\hbar} \cdot \nabla_{\boldsymbol{k}} f^0 + \frac{\boldsymbol{F}}{\hbar} \cdot \nabla_{\boldsymbol{k}} g = -\frac{g}{\tau} \tag{1.9}$$

In our work, in order to solve the coupled electron-phonon Boltzmann transport equations, we make the following approximations: (1) the transient terms are negligible, i.e. the first two terms on the left hand side of equation (1.9) will be neglected; (2) the gradient of g is much smaller than the gradient of f^0, i.e. the fourth and the last terms on the left hand side of equation (1.9) will be neglected; (3) g is much smaller than f^0 and we can use this to solve the coupled electron-phonon Boltzmann transport equations (as the electron-phonon interaction would affect both electrons' and phonons' states, the Boltzmann transport equation for electrons and the Boltzmann transport equation for phonons will be coupled when we take electron-phonon interaction into account) in chapter 2 and chapter 3. With these approximation, we can simplify equation (1.9) and get the linearized Boltzmann transport equation [74]

$$\boldsymbol{v} \cdot \nabla_{\boldsymbol{r}} f^0 + \frac{\boldsymbol{F}}{\hbar} \cdot \nabla_{\boldsymbol{k}} f^0 = -\frac{f - f^0}{\tau} \tag{1.10}$$

We will use equation (1.10) to calculate the thermoelectric properties in chapter 3. In particular, the coupled electron-phonon Boltzmann transport equations along with the detailed phonon drag formula derived from solving these equations will be given in section 3.3.

1.6 Thesis Outline

In this work, we study phonon drag effect in alloys by calculating the Seebeck coefficients, electrical conductivity and thermal conductivity of n-type SiGe alloys with different carrier concentrations (from $10^{15}\,\mathrm{cm}^{-3}$ to $10^{20}\,\mathrm{cm}^{-3}$) over the complete range of compositions using first-principles method within the virtual crystal approximation at 300K and 150K, considering electron-phonon interaction, phonon scattering due to anharmonicity, alloy and boundary, as well as electron scattering due to ionized impurity and alloy.

Chapter 1 gives the background of this study and introduces the basic concepts. Chapter 2 provides the details of the first-principles method adopted in this work for transport properties calculations. Chapter 3 shows that how we use the results from first-principles calculations to obtain transport properties based on Boltzmann transport equations. Finally, a summary of the current work and an outlook for the future work are given in chapter 4.

Chapter 2

First-principles Simulation of Transport Properties in SiGe Alloy System

To quantitatively evaluate phonon drag effect, we partially decouple the electron and phonon transport to solve the coupled electron-phonon linearized Boltzmann transport equations within the relaxation time approximation, and resort to first-principles calculations to obtain the detailed electron's information including the electronic band structure (the energy and the group velocity of the electron, $\varepsilon_{\boldsymbol{k}\alpha}$ and $v_{\boldsymbol{k}\alpha}$, where $\boldsymbol{k}$ and α denote the wavevector and the band number of an electron), the electron relaxation time $\tau_{\boldsymbol{k}\alpha}$, phonon's information including the phonon dispersion (the frequency and the group velocity of the phonon, $\omega_{\boldsymbol{q}\lambda}$ and $v_{\boldsymbol{q}\lambda}$, where $\boldsymbol{q}$ and λ denote the wavevector and the branch number of a phonon), the phonon relaxation time $\tau_{\boldsymbol{q}\lambda}$ and the electron-phonon interaction matrix element. The electronic band structure is the equilibrium property that describes the eigenstates of the electrons, which can be calculated using density functional theory (DFT). Density functional perturbation theory (DFPT) can be used to obtain phonon dispersion, electron-phonon and phonon-phonon interactions for it calculates the second and third derivatives of the

total energy at any arbitrary wavelength. The relaxation times describe the dynamics of the particle taking the interactions between the particle and different elements of its environment into account.

In this chapter, we start with introducing the basics of the many-body problem, especially density functional theory as well as density functional perturbation theory, then move to discussion on each scattering mechanism for electrons and phonons that is included in our first-principles calculations.

2.1 The Many-body Hamiltonian and Density Functional Theory

As we know, though we can solve the Schrödinger equation exactly for a single hydrogen atom, the problem will get much trickier if we are trying to do the same thing for the hydrogen molecule. As the system that we are looking at gets more complex, it is impossible to solve the many-electron problem without approximations except for small molecules. One of the most common approximations made in the many-body problem is the Born-Oppenheimer approximation. It assumes that the motion of atomic nuclei and electrons in a molecule can be separated because electrons travel much faster than atomic nuclei due to the large mass difference between them. Mathematically, it allows the wavefunction of a molecule to be broken into its electronic and nuclear (vibrational, rotational) components: $\Phi = \phi_{\text{electronic}} \times \phi_{\text{nuclear}}$. The many-body Hamiltonian for an electronic system with N_e electrons and N_n nuclei may be written in atomic unit as

$$H = -\frac{1}{2}\sum_{i}^{N_e}\nabla_i^2 - \sum_{i}^{N_e}\sum_{I}^{N_n}\frac{Z_I}{|\boldsymbol{r_i} - \boldsymbol{R_I}|} + \frac{1}{2}\sum_{i}^{N_e}\sum_{j\neq i}^{N_e}\frac{1}{|\boldsymbol{r_i} - \boldsymbol{r_j}|} + \frac{1}{2}\sum_{I}^{N_n}\sum_{J}^{N_n}\frac{Z_I Z_J}{|\boldsymbol{R_I} - \boldsymbol{R_J}|} \quad (2.1)$$

where Z is the charge of the ion, $\boldsymbol{r_i}$ is the position of electron i, $\boldsymbol{R_I}$ is the position of nucleus I. Indices i and j run over the electronic degrees of freedom and I and J rum

over nuclei. From left to right, the four terms on the right in equation (2.1) describe (1) kinetic energy, (2) nucleus-electron interaction: a Coulombic interaction involving one electron at a time. Electrons are considered as quantum mechanical particles and thus this interaction behaves like an external single-body potential acting on the electrons. In practice, this part is taken care of by replacing the true potentials of the nuclei with pseudopotentials, (3) electron-electron interaction: a Coulombic interaction involving pairs of electrons and (4) nucleus-nucleus interaction: nuclei are taken as classical particles that interact via the Coulombic forces. For the time being we can only consider the electronic Hamiltonian, and take the final term to be a constant.

Although the many-body Hamiltonian in equation (2.1) seems very straightforward, its exact solution is almost impossible to obtain for systems with more than a few electrons, largely due to the complexity in dealing with the correlation among electrons. As the number density of free electrons in any real semiconductor material can easily be greater than $10^{15}\,\mathrm{cm}^{-3}$, it will be impossible for us to solve the wavefunction considering every electron's interaction with one or multiple other electrons. Almost all electronic structure calculation methods resort to approximations which simplify the electron-electron interaction. The quality of the particular calculation used for a system depends on how well this approximation is chosen. Several methods have been devised to find accurate approximations. There are two broad classes of methods: (1) wavefunction-based methods (e.g. Hartree-Fock method [77, 78, 79]) where an explicit form for the wavefunction is written down and observables are calculated using this wavefunction, (2) density-based methods (e.g. density functional theory) in which the focus is shifted from the wavefunction to the electronic density and the wavefunction is not written explicitly.

A year after the publication of the Schrödinger equation, Hartree assumed that the nucleus together with the electrons formed a spherically symmetric field, and the charge distribution of each electron was the solution of the Schrödinger equation for an electron in an effective potential derived from the field. Each electron feels the

presence of the other electrons indirectly through the effective potential. The electrons are considered as occupying single-particle orbitals making up the wavefunction and each orbital is affected by the presence of electrons in other orbitals [80]. The starting point of the Hartree-Fock method is to write a variational wavefunction, which is built from these single particle orbitals. The simplest wavefunction that can be formed from these orbitals is their direct product

$$\Phi(\boldsymbol{r_1}, ..., \boldsymbol{r_N}) = \phi_1(\boldsymbol{r_1})\phi_2(\boldsymbol{r_2})...\phi_N(\boldsymbol{r_N}) \tag{2.2}$$

This is the Hartree approximation and it is straightforward to calculate the variational lowest energy. It allows us to to change the 3N dimensional Schrödinger equation (N electrons in 3 dimensions) into a 3 dimensional equation for each electron. However, pointed out by Slater and Fock independently [77, 78], the Pauli exclusion principle demands that the many-body wavefunction should be antisymmetric with respect to interchange of any two electron coordinates, for example

$$\Phi(\boldsymbol{r_1}, \boldsymbol{r_2}, ..., \boldsymbol{r_N}) = -\Phi(\boldsymbol{r_2}, \boldsymbol{r_1}, ..., \boldsymbol{r_N}) \tag{2.3}$$

which clearly can not be satisfied by equation (2.2).

In order to satisfy the antisymmetry condition, a more sophisticated form than that of the Hartree wavefunction is needed. It was then shown that a Slater determinant, a determinant of one-particle orbitals first used by Heisenberg [81] and Dirac [82] in 1926, trivially satisfies the antisymmetric property of the exact solution and hence is a suitable ansatz for applying the variational principle. For an N-electron system where the orbitals are taken to satisfy orthonormality, the wavefunction can be written as

$$\Phi = \frac{1}{\sqrt{N!}} \begin{vmatrix} \phi_1(\boldsymbol{r_1}) & \phi_2(\boldsymbol{r_1}) & \dots & \phi_N(\boldsymbol{r_1}) \\ \phi_1(\boldsymbol{r_2}) & \phi_2(\boldsymbol{r_2}) & \dots & \phi_N(\boldsymbol{r_2}) \\ \vdots & \vdots & \ddots & \vdots \\ \phi_1(\boldsymbol{r_N}) & \phi_2(\boldsymbol{r_N}) & \dots & \phi_N(\boldsymbol{r_N}) \end{vmatrix} \tag{2.4}$$

where the factor in front ensures normalization. Then we minimize the expectation value of the Hamiltonian in equation (2.1) $\langle\Phi|H|\Phi\rangle$ with respect to the basis functions. This requires functional differentiation where any change affected in the expectation value above due to an infinitesimal change in any of the orbitals wavefunction should be zero.

Solving the many-particle Schrödinger equation for the ground state wavefunction and energy is a daunting task even for the smallest system. An alternative route to the direct solution of the Schrödinger equation is shifting focus of the problem from $\Phi(\boldsymbol{r})$ to a fundamental observable of the problem, namely the density $n(\boldsymbol{r})$. This route is based on the Hohenberg-Kohn theorem [83], which asserts that the electron density of any system consisting of electrons moving under the influence of an external potential determines all ground-state properties of the system. In other words, the underlying principle of DFT is that the total energy of the system is a unique functional of the electron density, hence it is unnecessary to compute the full many-body wavefunction of the system. The functional that delivers the ground state energy of the system gives the lowest energy if and only if the input density is the true ground state density. However, the precise functional dependence of the energy on the density is not known, and since the solutions are for the ground state of the system, the temperature of the system is assumed to be 0K. Walter Kohn and Lu Jeu Sham [84] introduced the idea that the intractable many-body problem of interacting electrons in a static external potential can be reduced to a tractable problem of non-interacting electrons moving in an effective potential. The effective potential includes the external potential (the second term on the right hand side of equation (2.6)) and the effects of the Coulomb interactions between the electrons (the third term on the right hand side of equation

(2.6)). To eliminate the wavefunction by writing all terms making up the total ground state energy of the electronic system in terms of density, the density can be written as the sum of norm squares of a collection of single-particle orbitals

$$n(\boldsymbol{r}) = \sum_{n}^{N_e} |\phi_n(\boldsymbol{r})|^2 \tag{2.5}$$

Then the total ground state energy may be written as

$$\begin{aligned} E = & -\frac{1}{2}\sum_{n}^{N_e}\int d\boldsymbol{r}\phi_n^*(\boldsymbol{r})\nabla^2\phi_n(\boldsymbol{r})d\boldsymbol{r} + \int n(\boldsymbol{r})V_{\text{ne}}(\boldsymbol{r})d\boldsymbol{r} \\ & + \frac{1}{2}\int\int d\boldsymbol{r}d\boldsymbol{r}'\frac{n(\boldsymbol{r})n(\boldsymbol{r}')}{|\boldsymbol{r}-\boldsymbol{r}'|} + \Delta T + \Delta E_{\text{ee}} \end{aligned} \tag{2.6}$$

The kinetic energy as written cannot be differentiated directly with respect to $n(\boldsymbol{r})$ but it can be minimized with respect to the orbitals which is equivalent to minimizing with respect to $n(\boldsymbol{r})$. ΔT comes from the difference between the kinetic energy of the real many-particle system and the kinetic energy as the sum of the kinetic energies of the Kohn-Sham orbitals, and ΔE_{ee} is to correct the self-interaction term included in the third term. The last two correction terms together is named as the exchange-correlation energy (E_{xc}). More concisely, the origin of this term is the difference between a system of N interacting and non-interacting particles. Exchange energy (for same spins) is due to Pauli repulsion while correlation energy (more for opposite spins since they are more likely to occupy nearby locations) is due to collective behavior of electrons to screen and decrease the Coulombic interaction. Nonetheless, writing the exchange-correlation term in terms of the density becomes the difficulty within Kohn-Sham DFT. In practice, there are many approximations to model this, as the most popular ones are listed in Table 2.1.

For example, the oldest and simplest approximation, the local density approximation (LDA), is based upon exact exchange energy for a uniform electron gas. Non-interacting systems are relatively easy to solve as the wavefunction can be rep-

Table 2.1: Approximations (exchange-correlation functionals)

Exchange-correlation functionals	E_{xc} depends on
Local Density Approximation (LDA)	the particle density at that point
Generalized Gradient Approximations (GGA)	+ the local density gradient
Meta-GGAs	+ the Laplacian of the density

resented as a Slater determinant of orbitals. The kinetic energy functional of such a system is known exactly, but the exchange-correlation part of the total energy functional remains unknown and must be approximated. LDA assumes a simple form which is a linear functional of the density:

$$E_{xc}^{LDA} = \int d\boldsymbol{r} n(\boldsymbol{r}) \epsilon_{xc}^{hom}(n(\boldsymbol{r})) \tag{2.7}$$

where $\epsilon_{xc}^{hom}(n(\boldsymbol{r}))$ is the exchange correlation energy density of an interacting homogeneous electron gas at the density $n(\boldsymbol{r})$. Its exchange part is calculated exactly in the Hartree-Fock sense whereas the correlation part is a result of a fit to accurate MC data. Although LDA is a very crude approximation for systems that are not as homogeneous as an electron gas, it has proven to be a huge success. This is in part due to the cancellation of errors where LDA typically overestimates exchange energy while it underestimates correlation energy.

The quality of a DFT calculation is determined by how close the approximate exchange and correlation term comes to the exact value. As there is no known universal functional, nor even a framework in which to improve exchange-correlation approximations systematically, the performance of an exchange-correlation functional may only be tested by comparison to simple model systems, known experimental results or high-quality, computationally intensive post-DFT quantum chemistry calculations (e.g. GW calculation [66, 67]).

Compared to many conventional models that lack predictive power for they include adjustable parameters, and determine the parameters by fitting the calculated one or several measurable properties to the experimental data, density functional the-

ory starts directly at the level of established laws of quantum mechanics and does not make assumptions such as empirical model and fitting parameters. It is a computational quantum mechanical modelling method to study the ground-state properties of a many-electron system. In practical, we calculate the electronic band structure by using QUANTUM ESPRESSO package [72], which calculates the Kohn-Sham orbitals and energies to obtain the ground-state energies. There are some other approximations, e.g. using the effective interaction (pseudopotential) and a plane waves basis set with a finite number of plane waves, that do not alter the quantum mechanical framework of the first-principles method and usually have been carefully justified before use. We use a finite number of discrete reciprocal space points to sample the Brillouin zone in order that the calculation remains finite. This is justified as long as the orbitals vary smoothly with respect to the sampling points. A Monkhorst-Pack grid [85] is an unbiased method of choosing a set of points for sampling the Brillouin zone. In fractional coordinates, it is a rectangular grid of points of dimensions $n_x \times n_y \times n_z$, spaced evenly throughout the Brillouin zone. The larger the dimensions of the grid, the finer and more accurate will be the sampling. Hereinafter we refer k-points or k-mesh to the reciprocal space sampling in electronic band calculations, q-points or q-mesh mostly to the reciprocal space sampling in phonon calculations. Much like the cut-off energy, the size of grid required depends on the system under study, but the appropriate size can be established by means of a convergence test (we will provide our convergence test in section 3.3.4). In this sense, our DFT calculations can not be entirely accurate. However, with careful exam on the approximations above, realistic modeling of materials based on the solution of the density functional theory from the nanoscale upwards with accuracy comparable to experiment can be achieved.

Ground-state DFT calculations solve the wavefunctions with corresponding band energies, while the density functional perturbation theory [86, 87, 88] is a powerful and flexible theoretical technique that allows calculation of properties depending upon a system's response to some form of perturbation within the density functional framework. Many physical properties depend upon a system response to some form of

perturbation, examples include polarisabilities, phonons, Raman intensities. The basic ansatz behind DFPT is that quantities such as the wavefunction, electron density, or potential can be written as a perturbation series

$$X(\lambda) = X^{(0)} + \lambda X^{(1)} + \lambda^2 X^{(2)} + ... \tag{2.8}$$

where $X(\lambda)$ is a generic physical quantity that could, for example, be the Kohn-Sham orbitals $\phi(\lambda)$, the Kohn-Sham energy $E(\lambda)$, or the electronic density $n(\lambda)$, and λ is a perturbing parameter, assumed to be small. The expansion coefficients are given by

$$X^{(n)} = \frac{1}{n!}\frac{d^n X}{d\lambda^n}\bigg|_{\lambda=0} \tag{2.9}$$

Starting from

$$H(\lambda)|\Phi_i(\lambda)\rangle = \epsilon_i(\lambda)|\Phi_i(\lambda)\rangle \quad \forall\lambda \tag{2.10}$$

and inserting:

$$\begin{aligned} H(\lambda) &= H^{(0)} + \lambda H^{(1)} + \lambda^2 H^{(2)} + ... \\ \Phi_i(\lambda) &= \Phi_i^{(0)} + \lambda\Phi_i^{(1)} + \lambda^2\Phi_i^{(2)}... \\ \epsilon_i(\lambda) &= \epsilon_i^{(0)} + \lambda\epsilon_i^{(1)} + \lambda^2\epsilon_i^{(2)} + ... \end{aligned} \tag{2.11}$$

We will have the 0th order terms:

$$H^{(0)}|\Phi_i^{(0)}\rangle = \epsilon_i^{(0)}|\Phi_i^{(0)}\rangle \tag{2.12}$$

the 1st order terms:

$$H^{(0)}|\Phi_i^{(1)}\rangle + H^{(1)}|\Phi_i^{(0)}\rangle = \epsilon_i^{(0)}|\Phi_i^{(1)}\rangle + \epsilon_i^{(1)}|\Phi_i^{(0)}\rangle \tag{2.13}$$

the 2nd order terms:

$$H^{(0)}|\Phi_i^{(2)}\rangle + H^{(1)}|\Phi_i^{(1)}\rangle + H^{(2)}|\Phi_i^{(0)}\rangle = \epsilon_i^{(0)}|\Phi_i^{(2)}\rangle + \epsilon_i^{(1)}|\Phi_i^{(1)}\rangle + \epsilon_i^{(2)}|\Phi_i^{(0)}\rangle \tag{2.14}$$

And the expansion of the normalization condition that $\langle\Phi_i(\lambda)|\Phi_i(\lambda)\rangle = 1 \ \forall\lambda$ gives

the 0th order terms:

$$\langle\Phi_i^{(0)}|\Phi_i^{(0)}\rangle = 1 \tag{2.15}$$

the 1st order terms:

$$\langle\Phi_i^{(0)}|\Phi_i^{(1)}\rangle + \langle\Phi_i^{(1)}|\Phi_i^{(0)}\rangle = 0 \tag{2.16}$$

the 2nd order terms:

$$\langle\Phi_i^{(0)}|\Phi_i^{(2)}\rangle + \langle\Phi_i^{(1)}|\Phi_i^{(1)}\rangle + \langle\Phi_i^{(2)}|\Phi_i^{(0)}\rangle = 0 \tag{2.17}$$

Premultiply the 1st order of Schrödinger equation (equation (2.13)), we will get to the Hellman-Feynman theorem:

$$\epsilon_i^{(1)} = \langle\Phi_i^{(0)}|H^{(1)}|\Phi_i^{(0)}\rangle \tag{2.18}$$

that the 0th order of wavefunctions are thus the only required ingredient to obtain the 1st order corrections to the energies. Similarly for higher order terms, the nth order wavefunctions give access to the $2n^{\text{th}}$ and $2n+1^{\text{th}}$ order energy ("2n+1" theorem). There are 4 different methods to get the 1st order wavefunctions: (1) solving the Sternheimer equation $(H^{(0)} - \epsilon_i^{(0)})|\Phi_i^{(1)}\rangle = -(H^{(1)} - \epsilon_i^{(1)})|\Phi_i^{(0)}\rangle$ directly, complemented by a condition derived from the normalization requirement, (2) using the Green's function technique, (3) exploiting the sum over states expression, (4) minimizing the constrained functional for the $2n^{\text{th}}$ order corrections to the energies. More information on the detailed methods of DFPT can be found in literature [89].

As the atomic displacement corresponding the wavevector of a phonon can be regarded as a perturbation to the Hamiltonian of the electron system, we use DFPT method incorporated in QUANTUM ESPRESSO code [72] to obtain the force constant, phonon dispersion and the perturbed potential $\partial V_{\boldsymbol{q}\lambda}$ for later use in the electron-phonon interaction matrix element calculation. Starting with the electronic structure of the undistorted crystal obtained from a conventional DFT self-consistent calculation, the charge response to lattice distortions of definite wavevector $\boldsymbol{q}$ is calculated.

A different charge response must be calculated for each of the 3N independent atomic displacements, or for any equivalent combination thereof. Once the charge response to all atomic displacements (the computing effort is cut down by exploiting symmetry) have been processed, the dynamical matrix for the given $\boldsymbol{q}$ is obtained. However, dynamical matrix for any $\boldsymbol{q}$ is required in order to calculate the full phonon dispersion and all quantities depending on integrals over the Brillouin zone. This is accomplished by the inverse Fourier transform of dynamical matrices that are calculated on a finite uniform q-mesh to get the real-space interatomic force constants [90, 89], and constructing as well as diagonalizing the dynamical matrix at any given $\boldsymbol{q}$ in the Brillouin zone to obtain the phonon eigenstates.

2.2 Wannier Function-based Interpolation

Using the methods introduced in the last section, we calculate the electronic band structure and phonon dispersion using the QUANTUM ESPRESSO software [72], with norm-conserving pseudopotentials (Si.pz-n-nc.UPF and Ge.pz-n-nc.UPF, both are LDA) and a kinetic energy cut-off for wavefunctions of 80 Rydberg, a convergence threshold for self-consistency of 10^{-12} Rydberg. Electronic band structure is calculated using a $12 \times 12 \times 12$ k-mesh and phonon dispersion is calculated using a $6 \times 6 \times 6$ q-mesh.

However, for electron-phonon interaction matrix calculation, we need much denser meshes (e.g. $80 \times 80 \times 80$ k-mesh and q-mesh) than those above to meet the stringent convergence demands of the calculation of the electron-phonon interaction matrix element for the search of all possible electron-phonon scattering events that satisfy the conservation of energy and momentum rules. Limited by current computing power, we cannot use the same routine as above to obtain wavefunctions and perturbed potentials on the dense meshes as required. Our current best solution is to use the Wannier function-based [91] interpolation which interpolates between the matrix

elements from the coarse meshes to finer meshes with reasonably good accuracy and speed.

The simplest way of interpolation is linear interpolation that averages the contribution from sampling points and thus it has little physical significance. Interpolation methods that can capture and utilize the physical feature of the system will be much more efficient in sampling with limited number of sampling points. In systems where short-range interaction is dominant, single particle wavefunctions are localized around atomic sites, and tight-binding model is often used to calculate the band structure and single-particle Bloch states of the system. It assumes that in the vicinity of each lattice point the full periodic crystal Hamiltonian can be approximated by the Hamiltonian of a single atom located at the lattice point (H_{at}). Take the unit cell that contains only one atom as an example (can be extended to any unit cell [92]), the tight-binding model represents the crystal states as a linear superposition of the wavefunctions for isolated atoms on different sites, with coefficients incorporating the overlap

$$\Phi_{n\boldsymbol{k}}(\boldsymbol{r}) = \sum_{m,\boldsymbol{R}} c_{nm}\phi_n(\boldsymbol{r}-\boldsymbol{R})e^{i\boldsymbol{R}\cdot\boldsymbol{k}} \tag{2.19}$$

where ϕ_n is a bound level that meets $H_{at}\phi_n = E_n\phi_n$, $\boldsymbol{R}$ indicates different unit cells. Above is considering the wavefunctions as a function of $\boldsymbol{k}$ for fixed $\boldsymbol{r}$, while the wavefunction and associated band energy will vary as the wavevector $\boldsymbol{k}$ changes across the first Brillouin zone, the band structure is determined by the superposition coefficients c_{nm} for that the interaction is essentially short ranged. These coefficients can be obtained from the information on a coarse k-mesh in the reciprocal space, and once the coefficients are determined, the wavefunction and band energy on a finer k-mesh can be interpolated. This is the key concept of the Wannier interpolation method. Replacing the atomic wavefunctions ϕ_n in equation (2.19) with Wannier functions (denoted as f), the Bloch functions for any band can always be similarly written as [92]

$$\Phi_{n\boldsymbol{k}}(\boldsymbol{r}) = \sum_{\boldsymbol{R}} f_n(\boldsymbol{R},\boldsymbol{r})e^{i\boldsymbol{R}\cdot\boldsymbol{k}} \tag{2.20}$$

where the coefficients in the sum depend on $\boldsymbol{r}$ as well as on the "wavevector" $\boldsymbol{R}$, since for each $\boldsymbol{r}$ it is a different function of $\boldsymbol{k}$ that is being expanded, and the Fourier coefficients are given by the inversion formula

$$f_n(\boldsymbol{R}, \boldsymbol{r}) = \frac{1}{V_0} \int d\boldsymbol{k} e^{-i\boldsymbol{R}\cdot\boldsymbol{k}} \Phi_{n\boldsymbol{k}}(\boldsymbol{r}) \tag{2.21}$$

This shows if $\boldsymbol{r}$ and $\boldsymbol{R}$ are both shifted by the Bravais lattice vector $\boldsymbol{R_0}$, f is indeed unchanged as a consequence of Bloch's theorem. Thus, $f_n(\boldsymbol{R}, \boldsymbol{r})$ has the form of $f_n(\boldsymbol{R}, \boldsymbol{r}) = f_n(\boldsymbol{r} - \boldsymbol{R})$. However, the Wannier states given by equation (2.21) are not necessarily localized in the real space, while the tight-binding model first assumes that the electrons are strongly localized. To make a meaningful analogy from tight-binding model in terms of interpolating information on a coarse mesh to a fine mesh, effort has been made on achieving the maximal localization of Wannier states via the Fourier transform of the Bloch wavefunctions to the real space, e.g. the concept known as the maximally-localized Wannier functions [93] adopted in our calculations. It has been shown to connect with local orbitals in the material and achieve a successful mapping between points in the real space and in the reciprocal space.

Apart from electron's information, in order to obtain the electron-phonon matrix element, the perturbed potential and phonon's information are also required. It has been shown that extreme localization is achievable in the case of lattice vibrations because of the discrete number of degrees of freedom associated with the classical ions [94, 95], which means the maximally localized Wannier functions can be safely used to represent phonon dispersion. The perturbed potential $\partial V_{\boldsymbol{q}\lambda}$ for a phonon of given mode λ and wavevector $\boldsymbol{q}$ is due to a collective motion of atoms sitting on different atomic sites. Its Fourier transform gives the perturbed potential of which the spatial localization can be quantitatively assessed by the spatial decay of the interatomic force constants as long as the system under consideration can be described by the local density approximation to density functional theory [96]. Therefore, as long as the dominant forces among atoms are short ranged (which is the case for SiGe alloys), the same Wannier function-based method as above can be applied to interpolate the

perturbed potential.

In summary, in our calcualtions, electronic Wannier functions and phonon perturbation in the Wannier representation in the real space are first constructed from the information on coarse meshes, and they are interpolated to finer reciprocal meshes to obtain the electron-phonon matrix element. The interpolation is implemented in the EPW code [97] which uses routines from Wannier90 code [98] to calculate the Wannier functions, and is part of the Quantum ESPRESSO suite [72].

2.3 Electron Calculations

As described in section 2.1, the electronic band structure of SiGe alloys is calculated using DFT method and the results are shown in figure 2-1. Since the VCA method we adopted is basically weighted averaging pure Si's and pure Ge's properties, we can see starting from pure Si, as Ge content increases, the band shape gradually changes from Si's band structure to Ge's. Si and Ge have different band structures, and their conduction band minima are located at different valleys (Ge's is at L valley and Si's is near the X valley). When the two materials are being alloyed, their conduction bands start to cross over each other, and there will be a particular composition at which the two conduction band minima align with each other (as shown in the lower left figure in figure 2-1). This is the band convergence feature that will affect many of the alloys' transport properties, and we will discuss more about this when looking at different scattering mechanisms in the following sections as well as justifying our calculated thermoelectric properties in chapter 3.

The scattering mechanisms on electron considered in our calculations are electron-phonon interaction (EPI), alloy scattering on electron and ionized impurity scattering. In the following sections, we will discuss in detail how to obtain the relaxation times decided by these different scattering mechanisms under the relaxation time approximation. After obtaining those relaxation times, using the Matthiessen's rule [92], the

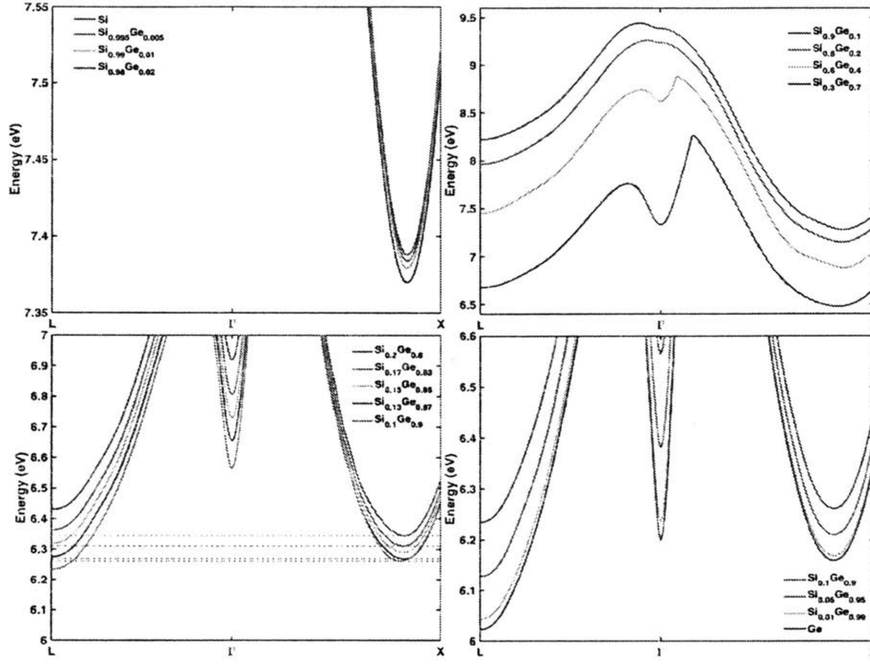

Figure 2-1: Calculated electronic band structure of SiGe alloys.The figure in the lower left corner shows the band convergence region (around the composition of $Si_{0.13}Ge_{0.87}$) where the L valley and the valley near X point are aligned.

effective relaxation time of the electron, $\tau_{\boldsymbol{k}\alpha}$ can be calculated as below

$$\frac{1}{\tau_{\boldsymbol{k}\alpha}} = \frac{1}{\tau_{\boldsymbol{k}\alpha,\,\text{electron-phonon}}} + \frac{1}{\tau_{\boldsymbol{k}\alpha,\,\text{alloy-electron}}} + \frac{1}{\tau_{\boldsymbol{k}\alpha,\,\text{impurity-electron}}} + \ldots$$

2.3.1 Electron Scattering by Phonons

In the electron-phonon scattering rate calculations, in order to reduce the computation complexity, we make the first-order approximation and assume phonons are at their equilibrium, that is, phonons obey Bose-Einstein distribution and we do not take the effect of scattering events on phonons' state into account. Later we will use these results for nonequilibrium case when we are calculating the transport properties, assuming the deviation of the phonons' state from equilibrium is small.

First, we enumerate all the possible electron-phonon scattering events relating to

the electron with wavevector $\boldsymbol{k}$ at band α in Table 2.2 where α and β denote the bands of the electron's initial and final states, and $\boldsymbol{k}$ and $\boldsymbol{k'}$ denote the wavevectors of the electron's initial and final states. $\boldsymbol{q}$, λ and ω denote the wavevector, the branch and the frequency of the phonon. The EPW code [97] allows $\boldsymbol{k'}$ to fall outside the first Brillouin zone and can calculate the energy of an electron state with wavevector that is outside the first Brillouin zone directly without folding the wavevector back to the first Brillouin zone, getting the same energy as for its counterpart inside the first Brillouin zone. Therefore, we can loop over the initial and the final states using the relations between $\boldsymbol{k}$, $\boldsymbol{k'}$ and $\boldsymbol{q}$ in Table 2.2 and do not need to differentiate between the normal process (crystal momentum conserves) and the Umklapp process (crystal momentum does not conserve).

Table 2.2: Possible electron-phonon scattering events for an electron

case	phonon	initial state	final state	momentum relation	energy relation
1	emitted	$\boldsymbol{k}\alpha$	$\boldsymbol{k'}\beta$	$\boldsymbol{k}-\boldsymbol{k'}-\boldsymbol{q}=0$	$\varepsilon_{\boldsymbol{k}\alpha}-\varepsilon_{\boldsymbol{k'}\beta}-\hbar\omega_{\boldsymbol{q}\lambda}=0$
2	absorbed	$\boldsymbol{k}\alpha$	$\boldsymbol{k'}\beta$	$\boldsymbol{k}+\boldsymbol{q}-\boldsymbol{k'}=0$	$\varepsilon_{\boldsymbol{k}\alpha}+\hbar\omega_{\boldsymbol{q}\lambda}-\varepsilon_{\boldsymbol{k'}\beta}=0$
3	emitted	$\boldsymbol{k'}\beta$	$\boldsymbol{k}\alpha$	$\boldsymbol{k}+\boldsymbol{q}-\boldsymbol{k'}=0$	$\varepsilon_{\boldsymbol{k}\alpha}+\hbar\omega_{\boldsymbol{q}\lambda}-\varepsilon_{\boldsymbol{k'}\beta}=0$
4	absorbed	$\boldsymbol{k'}\beta$	$\boldsymbol{k}\alpha$	$\boldsymbol{k}-\boldsymbol{k'}-\boldsymbol{q}=0$	$\varepsilon_{\boldsymbol{k}\alpha}-\varepsilon_{\boldsymbol{k'}\beta}-\hbar\omega_{\boldsymbol{q}\lambda}=0$

The total transition rate will be the sum of these transition rates above. Recall that we use equation (1.6) Fermi's golden rule to calculate the transition rates

$$\left(\frac{\partial f_{\boldsymbol{k}\alpha}}{\partial t}\right)_{\text{e-ph}}=\frac{2}{N_q}\frac{2\pi}{\hbar}\sum_{\boldsymbol{q}\lambda,\boldsymbol{k'}\beta}\Big[F_1+F_2+F_3+F_4\Big] \tag{2.22}$$

where the factor of 2 accounts for the electron spin. As introduced in section 2.1, a q-mesh of $N_q=N_{q1}\times N_{q2}\times N_{q3}$ to discretize the Brillouin zone into a Γ-centered regular grid is used for summation. The 4 cases of scattering elements in Table 2.2 correspond to F_1 to F_4. Write F_1 to F_4 out specifically using $\partial_{\boldsymbol{q}\lambda}V$ as the perturbed potential (caused by the ionic displacement corresponding to a phonon with wavevector $\boldsymbol{q}$ and at branch λ) in equation (1.6),

$$F_1=-f_{\boldsymbol{k}\alpha}(1-f_{\boldsymbol{k'}\beta})(n_\lambda+1)\left(\frac{\hbar}{2m_0\omega_{\boldsymbol{q}\lambda}}\right)|\langle\boldsymbol{k'}\beta|\partial_{\boldsymbol{q}\lambda}V|\boldsymbol{k}\alpha\rangle|^2\delta(\boldsymbol{k}-\boldsymbol{k'}-\boldsymbol{q})\delta(\varepsilon_{\boldsymbol{k}\alpha}-\varepsilon_{\boldsymbol{k'}\beta}-\hbar\omega_{\boldsymbol{q}\lambda})$$

$$F_2 = -f_{\boldsymbol{k}\alpha}(1 - f_{\boldsymbol{k}'\beta})n_\lambda \left(\frac{\hbar}{2m_0\omega_{\boldsymbol{q}\lambda}}\right) |\langle \boldsymbol{k}'\beta|\partial_{\boldsymbol{q}\lambda}V|\boldsymbol{k}\alpha\rangle|^2 \delta(\boldsymbol{k}+\boldsymbol{q}-\boldsymbol{k}')\delta(\varepsilon_{\boldsymbol{k}\alpha}+\hbar\omega_{\boldsymbol{q}\lambda}-\varepsilon_{\boldsymbol{k}'\beta})$$

$$F_3 = +f_{\boldsymbol{k}'\beta}(1-f_{\boldsymbol{k}\alpha})(n_\lambda+1) \left(\frac{\hbar}{2m_0\omega_{\boldsymbol{q}\lambda}}\right) |\langle \boldsymbol{k}'\beta|\partial_{\boldsymbol{q}\lambda}V|\boldsymbol{k}\alpha\rangle|^2 \delta(\boldsymbol{k}+\boldsymbol{q}-\boldsymbol{k}')\delta(\varepsilon_{\boldsymbol{k}\alpha}+\hbar\omega_{\boldsymbol{q}\lambda}-\varepsilon_{\boldsymbol{k}'\beta})$$

$$F_4 = +f_{\boldsymbol{k}'\beta}(1-f_{\boldsymbol{k}\alpha})n_\lambda \left(\frac{\hbar}{2m_0\omega_{\boldsymbol{q}\lambda}}\right) |\langle \boldsymbol{k}'\beta|\partial_{\boldsymbol{q}\lambda}V|\boldsymbol{k}\alpha\rangle|^2 \delta(\boldsymbol{k}-\boldsymbol{k}'-\boldsymbol{q})\delta(\varepsilon_{\boldsymbol{k}\alpha}-\varepsilon_{\boldsymbol{k}'\beta}-\hbar\omega_{\boldsymbol{q}\lambda})$$

The $\left(\frac{\hbar}{2m_0\omega_{\boldsymbol{q}\lambda}}\right)^{\frac{1}{2}} |\langle \boldsymbol{k}'\beta|\partial_{\boldsymbol{q}\lambda}V|\boldsymbol{k}\alpha\rangle|$ is the electron-phonon interaction matrix element, m_0 is the mass of one unit cell, $|\boldsymbol{k}\alpha\rangle$ and $|\boldsymbol{k}'\beta\rangle$ describe the eigenstates of electrons.

Similar to equation (1.8), the rate at which $f_{\boldsymbol{k}\alpha}$ relaxes can be defined as

$$\frac{1}{\tau_{\boldsymbol{k}\alpha}} \equiv -\frac{\delta}{\delta f_{\boldsymbol{k}\alpha}}\frac{\partial f_{\boldsymbol{k}\alpha}}{\partial t} \tag{2.23}$$

where $\frac{\delta}{\delta f_{\boldsymbol{k}\alpha}}$ is the variational derivative respect to $f_{\boldsymbol{k}\alpha}$. After some algebra, the electron scattering rate by equilibrium phonons can be expressed as

$$\frac{1}{\tau_{\boldsymbol{k}\alpha,\,\text{el-ph}}} = \frac{2}{N_q}\frac{2\pi}{\hbar}\left[\sum_{\boldsymbol{q}\lambda,\boldsymbol{k}'\beta}(n^0_{\boldsymbol{q}\lambda}+f^0_{\boldsymbol{k}'\beta})G^- + (n^0_{\boldsymbol{q}\lambda}+1-f^0_{\boldsymbol{k}'\beta})G^+\right] \tag{2.24}$$

where

$$\begin{aligned} G^+ &= \left(\frac{\hbar}{2m_0\omega_{\boldsymbol{q}\lambda}}\right) |\langle \boldsymbol{k}'\beta|\partial_{\boldsymbol{q}\lambda}V|\boldsymbol{k}\alpha\rangle|^2 \delta(\boldsymbol{k}-\boldsymbol{k}'-\boldsymbol{q})\delta(\varepsilon_{\boldsymbol{k}\alpha}-\varepsilon_{\boldsymbol{k}'\beta}-\hbar\omega_{\boldsymbol{q}\lambda}) \\ G^- &= \left(\frac{\hbar}{2m_0\omega_{\boldsymbol{q}\lambda}}\right) |\langle \boldsymbol{k}'\beta|\partial_{\boldsymbol{q}\lambda}V|\boldsymbol{k}\alpha\rangle|^2 \delta(\boldsymbol{k}+\boldsymbol{q}-\boldsymbol{k}')\delta(\varepsilon_{\boldsymbol{k}\alpha}+\hbar\omega_{\boldsymbol{q}\lambda}-\varepsilon_{\boldsymbol{k}'\beta}) \end{aligned} \tag{2.25}$$

We will go through this again when we derive the expression of phonon drag in section 3.3.1.

As said before, we first obtain the information (e.g. electronic band, the perturbed potential, phonon dispersion) on coarse meshes and then use the EPW code [97] to interpolate them onto an $80 \times 80 \times 80$ k-mesh and an $80 \times 80 \times 80$ q-mesh. The tetrahedra integration method [99] that incorporates the energy conservation is used when we are doing the integration by looping over the wavevectors $\boldsymbol{k}$ at the initial states and $\boldsymbol{k}'$ at the final states that conserve the momentum. The tetrahe-

dral method [99] linearly interpolates the information on the discrete mesh to the continuous reciprocal space, allowing analytic evaluation of the integration involving delta functions. Compared to many other smearing methods that require increasing the mesh density and decreasing the broadening parameter simultaneously, it contains only one parameter, the mesh density. We adopt the tetrahedral integration in our calculations for it features only one tuning parameter and easier check on the convergence. As shown in figure 2-1, SiGe alloys are semiconductor with non-zero

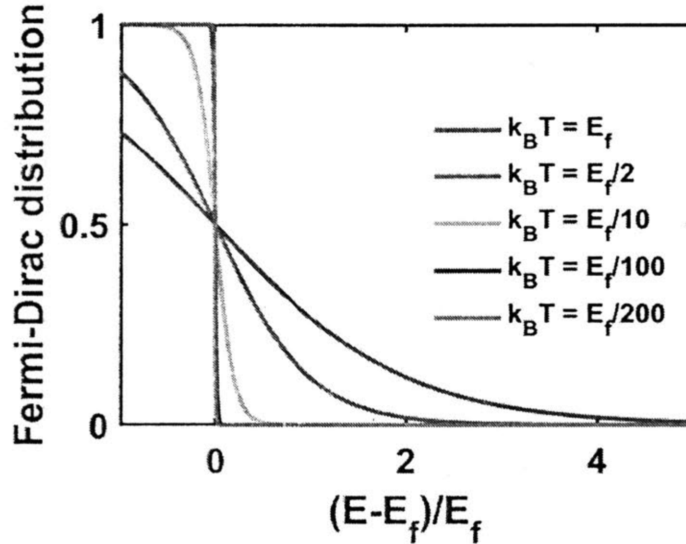

Figure 2-2: Fermi-Dirac distribution, where E denotes the electron's energy, E_f denotes the Fermi level. In SiGe alloys, k_BT at room temperature is typically around or smaller than $E_f/200$.

band gap. Remember the assumption that the deviation of the electron distribution function from the equilibrium Fermi-Dirac distribution function is small as we are using the linearized Boltzmann equation. And as shown in figure 2-2, the Fermi-Dirac distribution function decays exponentially as the energy goes above the Fermi level. Electrons with energy far above the Fermi level will only have negligible contribution to the transport properties. So for n-type semiconductors, the major contribution to the electrical transport properties comes from the electrons near the conduction band edge (as long as the material is not so heavily doped that the Fermi level has gone much higher than the conduction band edge). Hence, we further reduce the compu-

tational effort by setting an energy range of electrons that will be considered in our calculations. We set the highest energy of the electron that will be taken into account to 0.2 eV above conduction band edge or 0.2 eV above the Fermi level, whichever is higher. We add another 0.2 eV while we are searching for possible final states that satisfy the conservation of energy and momentum rules to ensure a full count of electron-phonon scattering events. The calculated electron scattering rate by phonons

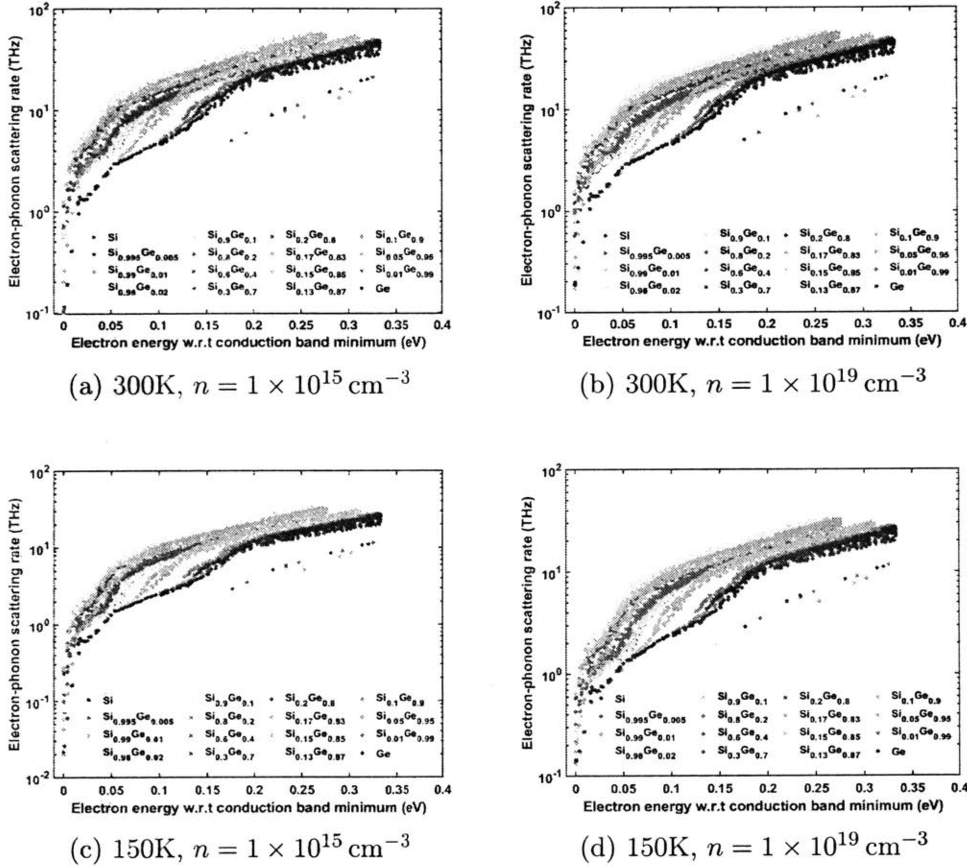

(a) 300K, $n = 1 \times 10^{15}\,\mathrm{cm}^{-3}$

(b) 300K, $n = 1 \times 10^{19}\,\mathrm{cm}^{-3}$

(c) 150K, $n = 1 \times 10^{15}\,\mathrm{cm}^{-3}$

(d) 150K, $n = 1 \times 10^{19}\,\mathrm{cm}^{-3}$

Figure 2-3: Calculated electron scattering rate by phonons vs. electron energy with respect to conduction band minimum, n denotes the n-type carrier concentration. T = 300K and 150K. (a)(c) of lightly doped n-type SiGe alloys (b)(d) of heavily doped n-type SiGe alloys.

of lightly doped and heavily doped SiGe alloys at 300K and 150K are shown in figure 2-3. In the very vicinity of the conduction band minimum, only phonon absorption process is allowed to happen and electron's scattering phase space is pretty restricted by the energy and momentum selection rules. As electron energy gets higher, more

phonon emission events can happen and more electron states that meet the energy conservation and momentum conservation are available for electron-phonon scattering events. This is proved in the drastic increase near the band edge in the scattering rate in figure 2-3, as well as visualized in figure 2-4. Figure 2-4 shows the strength of intervalley and intravalley scattering at the band edge of $Si_{0.15}Ge_{0.85}$, the comparison between the two subfigures tells that the intervalley scattering is the dominant process. Silicon has six equivalent valleys in the conduction band and germanium has four, plus the Γ valley that is not far above the conduction band edge for germanium, we count any scattering event in which the electron' initial and final states are at any two different valleys among the eleven as an intervalley process and the ones in which the electron' initial and final states are at the same one valley as an intravalley process. We can see that the electron-phonon scattering rate is the highest in the band convergence region (around the composition of $Si_{0.13}Ge_{0.87}$). This is partially due to that, when the conduction band minima are aligned, there are more available electron states that meet the energy conservation and momentum conservation conditions of the electron-phonon scattering events, which would especially lead to an increase in electrons' intervalley scattering. As shown in figure 2-5, the intravalley scattering rate does not vary much with composition around the band convergence composition and indeed the increase is in the intervalley scattering rate at the band convergence point. In figure 2-3 we also notice that at higher temperatures, larger phonon population leads to higher electron-phonon scattering rates. Changing the doping concentration would affect the Fermi level and thus the electron population. Its effect on electron-phonon scattering rate is more significant at lower temperatures for Fermi-Dirac distribution has the form of $f^0 = \frac{1}{1+e^{(\varepsilon-\varepsilon_f)/k_B T}}$.

2.3.2 Alloy Scattering of Electrons

The model of alloy scattering of electrons rests on the VCA theory. As introduced in section 1.4, Nordheim was the first to consider the problem of calculating the resistiv-

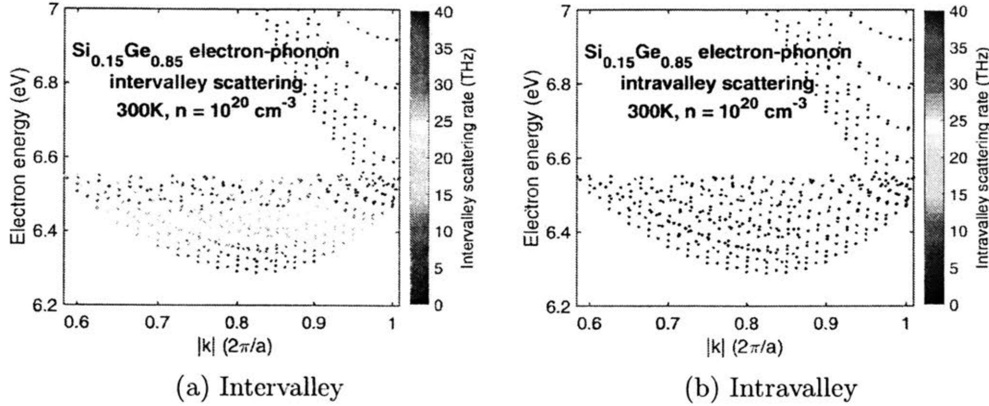

(a) Intervalley (b) Intravalley

Figure 2-4: Calculated intervalley and intravalley electron scattering rates by phonons in $Si_{0.15}Ge_{0.85}$ at T = 300K, n-type carrier concentration $n = 1 \times 10^{20}\,\mathrm{cm}^{-3}$. The conduction band minimum for silicon is near X valley $[0, 0.85(\frac{2\pi}{a}), 0]$ with $|k| = 0.85(\frac{2\pi}{a})$ and for germanium it is at L valley $[\frac{\pi}{a}, \frac{\pi}{a}, \frac{\pi}{a}]$ with $|k| = 0.866(\frac{2\pi}{a})$, where a denotes the lattice constant. Scattering rates for the electron states with energy out of the range that we consider are not calculated and taken as zero.

ity of alloys within a quantum mechanics picture, where he dealt with the perfectly random crystal by introducing the concept of virtual crystal [68]. The actual crystal was considered to be divided into a perfectly periodic array of potentials, the virtual crystal that is composed of the composition weighted potentials from different species of atoms in the crystal, and a random part due to the difference between the actual crystal potential and the virtual crystal potential at a given lattice point. This random part was used as a perturbed potential, leading to a matrix element for transitions between electron states. In 1956, Flinn developed the electronic theory of local order and obtain an expression for the energy that includes a local order dependent term by applying the perturbed free-electron approximation to a binary metallic solid solution [100]. Later Hall [101] extended Nordheim's theory to account for ionic potentials that extend outside the unit cell and order of any range, and pointed out that Flinn's electronic theory of order can be extended similarly. Based on Nordheim's theory for purely random alloys and Hall's extension for nonrandom alloys, Asch and Hall [102] further developed a quantum theory of the residual electrical resistivity of binary disordered alloys for atomic potentials extending outside the unit cell that is valid for any degree of order, including the change in lattice parameter

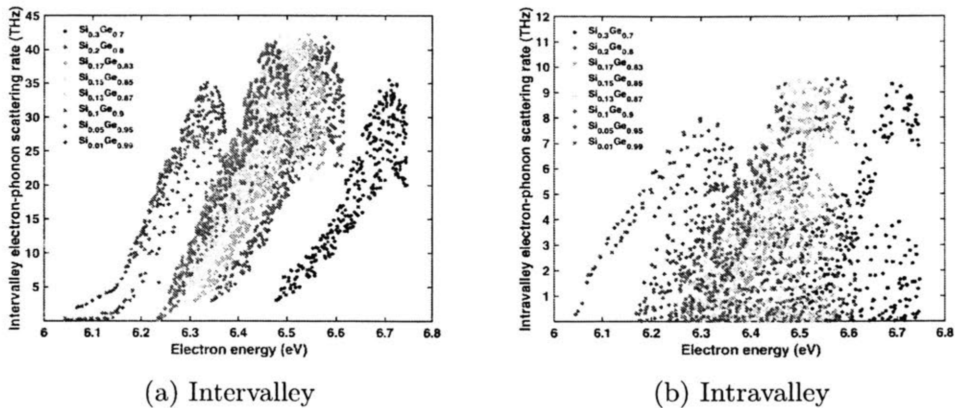

(a) Intervalley

(b) Intravalley

Figure 2-5: Calculated intervalley and intravalley electron scattering rates by phonons vs. electron energy near the band convergence region at T = 300K, n-type carrier concentration $n = 1 \times 10^{20}\,\mathrm{cm}^{-3}$.

with alloying and the change in effective number of conduction electrons per atom with composition. Harrison and Hauser [103] calculated the alloy scattering rate for ternary III-V compounds where one of the elements is common to both of the constituent compounds using a pseudobinary alloy model and a "square-well" potential. These early theoretical works suffice as the formal framework for our first-principles calculations.

Here in our work, we adapt an approach from the VCA method in F. Murphy-Armando and S. Fahy's work [56, 104], where they used first-principles electronic structure methods to find the rates of intravalley and intervalley n-type carrier scattering due to alloy disorder in SiGe alloys. Our first-principles approach starts with the construction of the supercells (each supercell is a $2 \times 2 \times 2$ conventional cubic cell containing 64 atoms) modeling a unperturbed virtual crystal (VC) system, for which we find the ground-state density and the Hamiltonian of the system via the supercell eigenvalues and eigenstates. Later we need to find out the perturbed potential, so we also construct supercells of the same size as above modeling a perturbed VC system by substituting one VC atom with a Si atom, and a perturbed VC system by substituting one VC atom with a Ge atom. Limited by computing power, we cannot deal with an infinitely large alloy system as in the formal model of alloy scattering,

however, we are able to capture the alloy scattering behavior by averaging within the $2 \times 2 \times 2$ conventional cubic supercell containing 64 atoms. We interpret the number of ions in the system N as the number of atoms in the supercell and the volume of the system Ω as the supercell volume. As described by Nordtheim, the potential can be decomposed into two parts: the VCA potential, being an average potential weighted according to the proportions of each species, which can be obtained from the case of the unperturbed VC system, and a random part due to the difference in potential arising from the substitution of one atomic species for the other that we get from subtracting the potential of one of the perturbed cases from the other perturbed case. It is this random part that provides a perturbation giving rise to scattering. Hereafter, we refer to $\Delta V(\boldsymbol{r})$ as the alloy scattering potential and we use this perturbed potential to calculate the transition rate between an initial state ϕ_k and final state $\phi_{k'}$ in Fermi's golden rule within the first Born approximation where ϕ represents the undisturbed Bloch wavefunction of the periodic host lattice.

$$\langle V_{ab}\rangle = \langle V_{ab}^{Ge}\rangle - \langle V_{ab}^{Si}\rangle = \langle \phi_{\boldsymbol{k}'b}|\Delta V^{Ge}|\phi_{\boldsymbol{k}a}\rangle - \langle \phi_{\boldsymbol{k}'b}|\Delta V^{Si}|\phi_{\boldsymbol{k}a}\rangle = \langle \phi_{\boldsymbol{k}'b}|\Delta V(\boldsymbol{r})|\phi_{\boldsymbol{k}a}\rangle$$

where ΔV^A (with A = Si or Ge) is the perturbed potential caused by the substitution of one atom in the periodic VC host $2 \times 2 \times 2$ supercell by a type-A atom. a and b mark different valleys and both intravalley ($a = b$) and intervalley ($a \neq b$) terms are included in the total scattering rate.

With the assumptions that (1) the alloy is completely random, there is no correlation between the atomic species on different sites, the scattering matrix element is independent of the wavevectors of the initial and the final states, $\boldsymbol{k}$ and $\boldsymbol{k}'$; (2) Si and Ge are relatively weak scatterers that each site scatters carriers independently; (3) the average of the scattering matrix is zero for the average crystal does not scatter, the scattering rate of electron of wavevector $\boldsymbol{k}$ in valley a due to alloy disorder in the random binary substitutional alloy is given by [104]

$$
\begin{aligned}
\frac{1}{\tau(\varepsilon_{\boldsymbol{k}a})_{\text{alloy-electron}}} &= \frac{2\pi}{\hbar}x(1-x)N\sum_{b}\int\frac{\Omega}{(2\pi)^3}d^3k'|\langle V_{ab}\rangle|^2\delta(\varepsilon_{\boldsymbol{k}a}-\varepsilon_{\boldsymbol{k}'b}) \\
&= \frac{2\pi x(1-x)N}{\hbar N_k}\sum_{\boldsymbol{k}'b}|\langle V_{ab}\rangle|^2\delta(\varepsilon_{\boldsymbol{k}a}-\varepsilon_{\boldsymbol{k}'b})
\end{aligned} \tag{2.26}
$$

where x is the Ge content, b labels the valley into which scattering occurs. As introduced in section 2.1, a k-mesh of $N_k = N_{k1} \times N_{k2} \times N_{k3}$ to discretize the Brillouin zone is used for summation in the reciprocal space. The undisturbed Bloch wavefunction of the periodic host lattice is obtained from the DFT calculation using VC unit cell. By changing the phase factor, this undisturbed Bloch wavefunction is mapped to the VC supercell. And after normalization within the supercell, the wavefunction is used in the integral on the right hand of equation (2.26). While in theory this integral is over the full real space, due to the fact that the perturbed potential is very localized, we assume the supercell is large enough that outside the supercell the perturbed potential is zero, thus we equate the integral within the supercell with the integral over the full space.

Again we first obtain the information (e.g. alloy scattering matrix element) on coarse meshes and interpolate them onto an $80 \times 80 \times 80$ k-mesh and an $80 \times 80 \times 80$ q-mesh (similar to ionized impurity scattering, alloy electron scattering does not involve phonon and is an elastic process, unlike in electron-phonon scattering calculations that $\boldsymbol{q}$ can represent phonon's wavevector, here the q-mesh is only for the loop over final state $\boldsymbol{k}' = \boldsymbol{k} + \boldsymbol{q}$) with Wannier interpolation. The tetrahedra integration method [99] that incorporates the energy conservation is used when we are doing the integration by looping over the initial states $\boldsymbol{k}$ and the the change in electron wavevector $\boldsymbol{q}$ (equivalent of looping over the final states $\boldsymbol{k}'$ for $\boldsymbol{k}' = \boldsymbol{k} + \boldsymbol{q}$) that conserve the energy. The alloy-electron scattering results are shown in figure 2-6. The plot on the logarithmic scale clearly shows the trend of alloy-electron scattering rate to electron energy that at the conduction minimum, constrained by the energy conservation rule, there are very few states that electron can be scattered into thus the scattering rate is

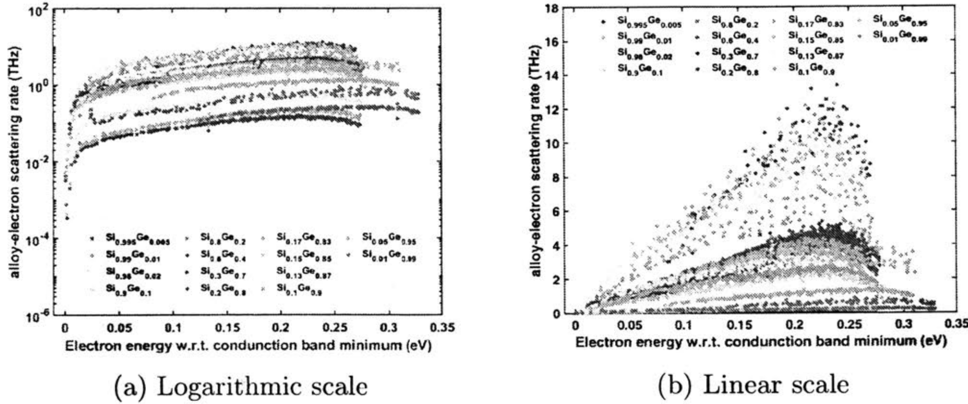

(a) Logarithmic scale (b) Linear scale

Figure 2-6: Alloy-electron scattering rate of SiGe alloys on logarithmic scale and linear scale.

very low. As electron energy gets higher, there are more initial and final states that meet the energy conservation and thus the scattering rate increases and gradually saturates (note that the drop at the tail of the curves is due to our cut-off in electron energy, we stop searching for final states when electron energy is out of the range that we consider), which is also visualized in figure 2-7. Figure 2-7 takes $Si_{0.2}Ge_{0.8}$ as an example and gives the comparison between the intervalley and intravalley scattering rates and shows the intervalley scattering is more significant than the intravalley scattering. We also notice in figure 2-6, more valleys would be involved at higher electron energy and electron at different valleys would scatter differently because of the different band shapes of those valleys, thus the scattering curves would split into several branches. From the electron energy we can determine that the upper branches with higher scattering rates correspond to the scattering happening at L valley where the conduction band minimum locates for germanium and the lower branches correspond to the scattering happening at the valley near X point where the conduction minimum for silicon locates. We can see from figure 2-6, starting from pure silicon side, as the content of germanium increases, the alloy-electron scattering increases and then decreases, which can be intuitively interpreted as that the "randomness" of the alloy increases and then decreases. We notice from the plot on the linear scale that the alloy-electron scattering rate is the highest in the band convergence region

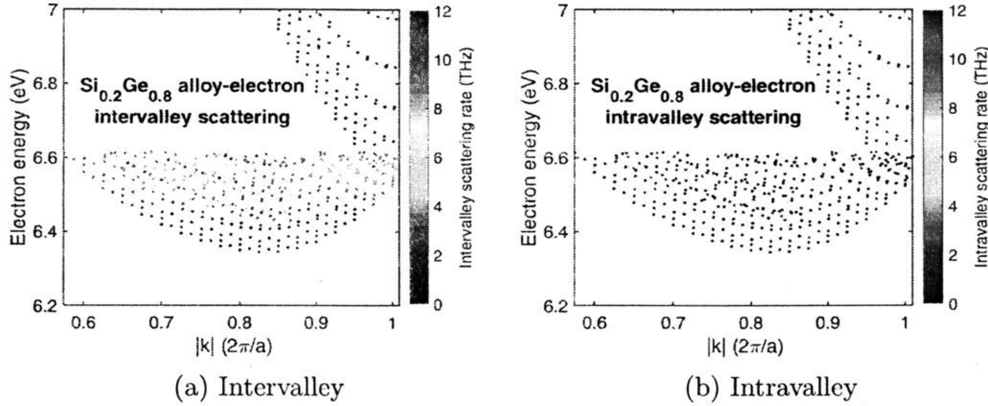

(a) Intervalley (b) Intravalley

Figure 2-7: Calculated intervalley and intravalley alloy-electron scattering rates in $Si_{0.2}Ge_{0.8}$. The conduction band minimum for silicon is near X valley $[0, 0.85(\frac{2\pi}{a}), 0]$ with $|k| = 0.85(\frac{2\pi}{a})$ and for germanium it is at L valley $[\frac{\pi}{a}, \frac{\pi}{a}, \frac{\pi}{a}]$ with $|k| = 0.866(\frac{2\pi}{a})$. Scattering rates for the electron states with energy out of the range that we consider are not calculated and taken as zero.

(around the composition of $Si_{0.13}Ge_{0.87}$) for there are more available electron states that meet the energy conservation condition when the conduction band minima are aligned. We plot the intervalley and intravalley scattering rates at the conduction band edge around near the band convergence point in figure 2-8. We can see both intervalley and intravalley scattering happening at the valley near X point increase with the increasing "randomness" of the alloy. Though the scattering happening at L valley is stronger than the one happening at the valley near X point, the electrons population at L valley gets smaller as the "randomness" of the alloy becomes greater. In short, the "randomness" of the alloy, the shape of conduction band minimum and the band population would all affect alloy-electron scattering.

2.3.3 Ionized Impurity Scattering

Charge carriers are scattered when they encounter the electric field of an ionized impurity, thus ionized impurity scattering should be considered when we study the electron transport properties in heavily doped samples. The classical theories of ionized impurity scattering based on the Born approximation (the Born approximation

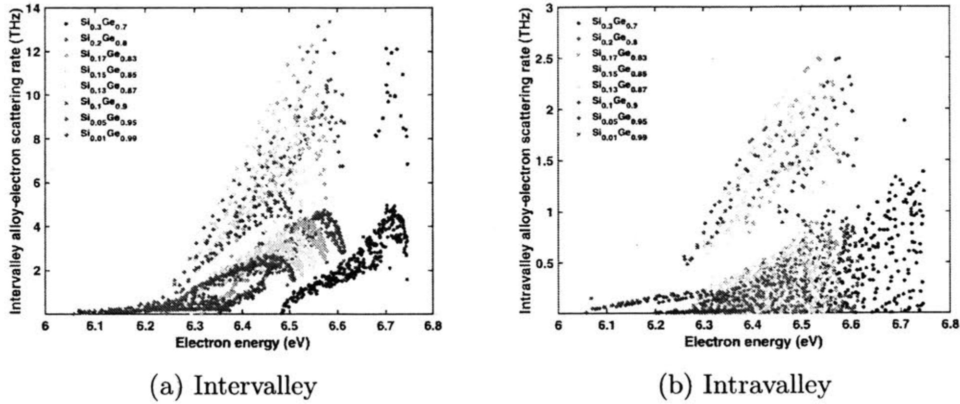

(a) Intervalley

(b) Intravalley

Figure 2-8: Calculated intervalley and intravalley alloy-electron scattering rates vs. electron energy near the band convergence point.

will be good if the scattering potential falls off rapidly at large distances, and if the carrier energy or the temperature is high, which should be satisfied in our case) includes the Conwell-Weisskopf model (unscreened Coulomb scattering) [105] and the Brooks-Herring model (screened Coulomb scattering) [106, 107]. Their subsequent refinements and other methods beyond Born approximation like the phase-shift method are nicely summarized in Chattopadhyay et al. 's review [108]. For the sake of simplicity, in this work we adopt the Brooks-Herring model to estimate the effect of ionized impurity scattering.

We start by assuming that the ionized impurity scattering potential is Coulombic (in this model, the atomic core potential of the ionized impurity atom is neglected thus the core scattering of ionized impurity is not included), however, the ionized impurity attracts mobile carriers that screens the potential. For an n-type semiconductor, the screened Coulomb potential is [107]

$$U_s(r) = \frac{Zq^2}{4\pi\epsilon_r\epsilon_0}e^{-r/L_D} \tag{2.27}$$

where q is the elementary charge and Z is the charge of the impurity, ϵ_r is the dielectric constant of the host material, ϵ_0 is the permittivity of vacuum, L_D is the Debye length

given by

$$L_D = \sqrt{\frac{\epsilon_r \epsilon_0}{q^2 \frac{\partial n}{\partial \varepsilon_f}}} \tag{2.28}$$

where n is the carrier density. With the scattering potential in equation (2.27), the matrix element can be obtained [107, 108]

$$H_{\boldsymbol{p}'\boldsymbol{p}} = \frac{1}{\Omega}\left(\frac{Zq^2}{4\pi\epsilon_r\epsilon_0}\right)\int e^{-i\boldsymbol{p}'\cdot\boldsymbol{r}/\hbar}\left(\frac{e^{-r/L_D}}{r}\right)e^{-i\boldsymbol{p}\cdot\boldsymbol{r}/\hbar}d^3r \tag{2.29}$$

or in a spherical coordinate system according to the geometry of the scattering event shown in figure 2-9.

$$H_{\boldsymbol{p}'\boldsymbol{p}} = \frac{1}{\Omega}\left(\frac{Zq^2}{4\pi\epsilon_r\epsilon_0}\right)\int_0^{2\pi} d\phi \int_0^{\pi}\int_0^{\infty} e^{-r/L_D}e^{i(\boldsymbol{p}-\boldsymbol{p}')\cdot\boldsymbol{r}/\hbar} r\,dr\sin\theta d\theta \tag{2.30}$$

The scattering by ionized impurities is an elastic process, that is, in figure 2-9, $\hbar\boldsymbol{\beta} = \boldsymbol{p}' - \boldsymbol{p}$, and $\hbar\beta = 2p\sin(\frac{\alpha}{2})$. The triple integrals give the expression of the matrix element as a function of β

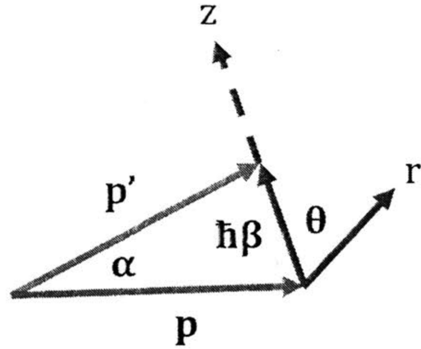

Figure 2-9: Definition of $\hbar\boldsymbol{\beta}$, the momentum change resulting from scattering.

$$\begin{aligned} H_{\boldsymbol{p}'\boldsymbol{p}} &= \frac{1}{\Omega}\left(\frac{Zq^2}{4\pi\epsilon_r\epsilon_0}\right)\int_0^{\infty}\int_0^{2\pi}\int_{-1}^{+1} re^{r/L_D}e^{-i\beta r\cos\theta}d(\cos\theta)d\phi dr \\ &= \frac{q^2}{\Omega\epsilon_r\epsilon_0}\frac{1}{\beta^2 + 1/L_D^2} \end{aligned} \tag{2.31}$$

Again with Fermi's golden rule and similar algebra in the last section, and multiply

by the number of impurities ($N_1\Omega$) in the normalization volume, the scattering rate due to scattering from ionized impurities in the normalization volume can obtained

$$\frac{1}{\tau_{\boldsymbol{k}\alpha,\,\text{impurity-electron}}} = \frac{2\pi}{\hbar}\frac{N_1 Z^2 q^4}{\epsilon_r^2\epsilon_0^2\Omega N_k}\sum_{\boldsymbol{k}'}\frac{\delta(\varepsilon(\boldsymbol{k}') - \varepsilon(\boldsymbol{k}))}{(\beta^2 + 1/L_D^2)^2} \tag{2.32}$$

We calculate ionized impurity scattering rate on an $80\times80\times80$ k-mesh (for the initial states) by summing over an $80 \times 80 \times 80$ q-mesh (represents $\boldsymbol{\beta}$). The tetrahedra integration method [99] is used to deal with the energy conservation. The results are shown in figure 2-10. The plots on the logarithmic show the trend that at the

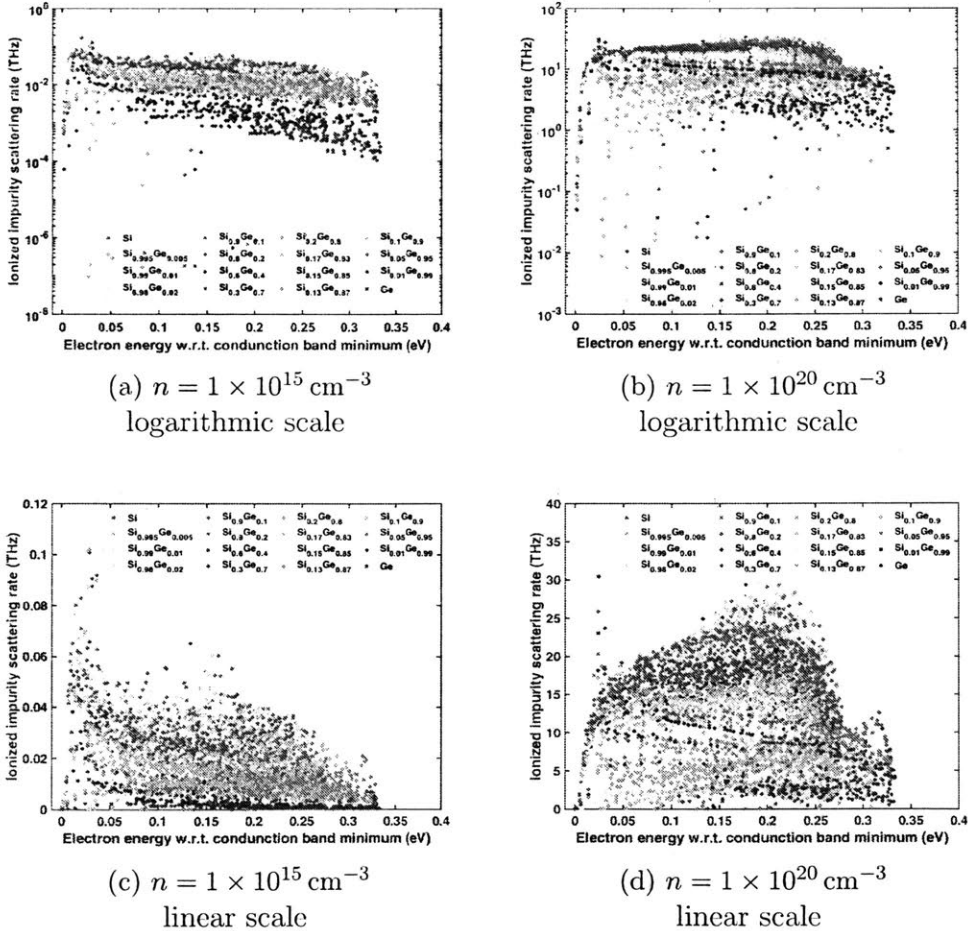

(a) $n = 1 \times 10^{15}\,\text{cm}^{-3}$ logarithmic scale

(b) $n = 1 \times 10^{20}\,\text{cm}^{-3}$ logarithmic scale

(c) $n = 1 \times 10^{15}\,\text{cm}^{-3}$ linear scale

(d) $n = 1 \times 10^{20}\,\text{cm}^{-3}$ linear scale

Figure 2-10: Calculated ionized impurity scattering rate of lightly doped and heavily doped SiGe alloys both on logarithmic scale and linear scale. n denotes the n-type carrier concentration.

conduction minimum, constrained by the energy conservation rule, there are very few states that electron can be scattered into thus the scattering rate is very low. As electron energy gets higher, there are more initial and final states that meet the energy conservation. Also, equation (2.32) shows scattering events with smaller β are more likely to happen (actually β is assumed to be small in the derivation of the Brooks-Herring model [108] hence we only take intravalley scattering into account). This together with the energy conservation rule lead to the large scattering rates around 0.02-0.05 eV above the conduction band minimum, and the slight decrease in scattering rate when electron energy gets higher than 0.05 eV above the conduction band minimum. At the higher doping concentration, the $1/L_D^2$ becomes the dominant term in the denominator in equation (2.32), change in β^2 would affect the scattering rate less and the decreasing trend alters. We notice from the plots on the linear scale that the highest impurity scattering rate is neither at the pure silicon nor in the band convergence region. This is because that, first the several deciding parameters of the VC alloys in equation (2.32) (dielectric constant, cell volume) are more or less weighted averaged from those parameters of pure Si and of pure Ge's, therefore virtual crystal alloys generally show some averaging feature, that the ionized impurity scattering rates are higher at the Si-rich side than at the Ge-rich side. Second, as discussed in the previous sections, the scattering phase space of electrons near the band edge becomes larger in the band convergence region, and larger scattering phase space will increase the scattering rate. A combined effect of these two influencing factors account for that the highest ionized impurity scattering rate is in the Si-rich alloys. It is confirmed by the comparison between the scattering rates at two carriers concentration that ionized impurity scattering become more significant as the doping concentration gets higher.

The electron mobilities, calculated using the scattering rate from

$$\frac{1}{\tau_{\boldsymbol{k}\alpha}} = \frac{1}{\tau_{\boldsymbol{k}\alpha,\,\text{electron-phonon}}} + \frac{1}{\tau_{\boldsymbol{k}\alpha,\,\text{alloy-electron}}} + \frac{1}{\tau_{\boldsymbol{k}\alpha,\,\text{impurity-electron}}} + \ldots$$

based on linearized Boltzmann transport equation in the relaxation time approxima-

tion, are compared with experimental data on bulk, unstrained germanium and SiGe alloy in section 3.1.1, followed with discussion on possible causes of error.

2.4 Phonon Calculations

The phonon dispersion of SiGe alloys has been calculated based on the DFPT method as described in section 2.1, and the results are shown in figure 2-11. We can see the shapes of SiGe alloys' phonon dispersion are very similar since Si and Ge both have the same face-centered diamond-cubic crystal structure, but with different phonon frequencies because of the different atomic weights. And as the VCA method we adopted is basically weighted averaging pure Si's and pure Ge's properties, starting from pure Si, as Ge content increases, the phonon frequency changes from Si's to Ge's.

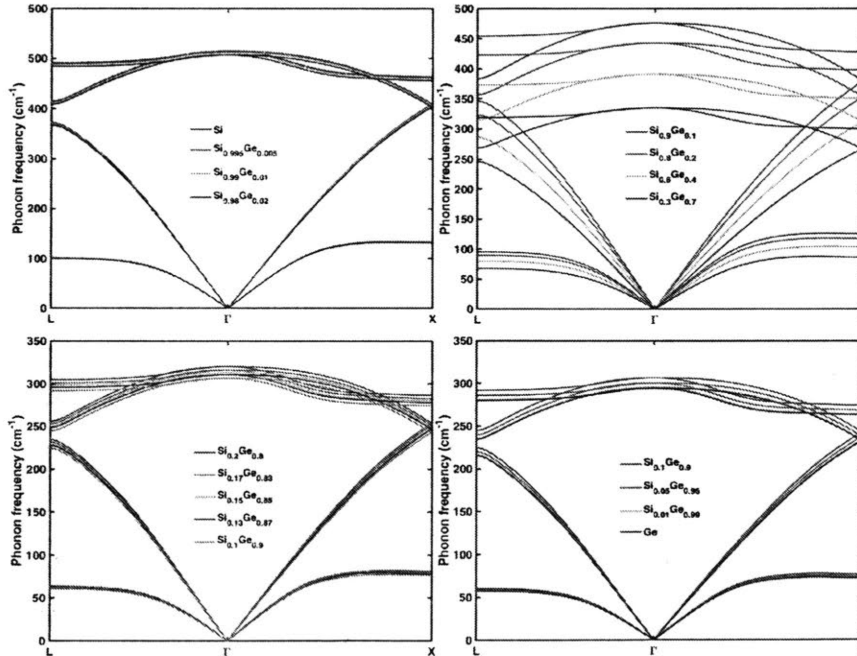

Figure 2-11: Calculated phonon dispersion of SiGe alloys around the center of the Brillouin zone.

The scattering mechanisms on phonon considered in our calculations are intrin-

sic phonon-phonon scattering, electron-phonon interaction (EPI), alloy scattering on phonon (mass disorder scattering) and boundary scattering. We will discuss in detail how to obtain the relaxation times decided by these different scattering mechanisms under the relaxation time approximation in the following sections. After obtaining those relaxation times, the effective relaxation time of the phonon, $\tau_{q\lambda}$ can be calculated using Matthiessen's rule [92] as below

$$\frac{1}{\tau_{q\lambda}} = \frac{1}{\tau_{q\lambda,\,\text{phonon-phonon}}} + \frac{1}{\tau_{q\lambda,\,\text{electron-phonon}}} + \frac{1}{\tau_{q\lambda,\,\text{alloy-phonon}}} + \frac{1}{\tau_{q\lambda,\,\text{boundary}}} + ...$$

which will be used for thermal transport calculations in chapter 3.

2.4.1 Phonon-phonon Interaction

If we make the first-order approximation to express the total energy of the system as a quadratic function of the atom displacements, we can obtain the harmonic phonon properties, including dispersion, heat capacity, group velocity by using DFPT method as introduced in section 2.1. This harmonic approximation treats phonons as independent oscillators, which means they have infinite lifetimes. In an "ideal" insulating crystal, the possibility for harmonic phonons to scatter off electrons can be removed and they would propagate without hinderance as free particles. However, infinite thermal conductivity is unrealistic in this kind of materials that we are left to attribute the finite thermal conductivity to phonons' scattering by crystal imperfections, i.e., defects and ultimately the surfaces of the crystal. Scattering of phonons from crystal imperfections does produce a finite thermal conductivity but with a different temperature dependence from experiments'. To address the issue above, the anharmonic effect is required and the phonon-phonon scattering needs to be included to model heat transport. The anharmonicity is a perturbation to the harmonic system that allows transitions of phonons between different states. In fact, when the temperature is not very low, the dominant scattering mechanism of phonons is the phonon-phonon interaction and it is the key component determining phonons' relaxation times.

As given in equation (2.8), in perturbation theory, the crystal potential can be expanded as a power of displacement and the Hamiltonian may be written as

$$H(\lambda) = H^{(0)} + \lambda H^{(1)} + \lambda^2 H^{(2)} + ... \tag{2.33}$$

where $H^{(0)}$ is the harmonic Hamiltonian and $H^{(1)}$, $H^{(2)}$, ... are the perturbation terms involving three, four or more interacting phonons. The simplest phonon-phonon interaction and usually the dominant one in most of materials is the three-phonon interaction where a phonon decays into two other phonons or vice-versa (as shown in figure 2-12). The Hamiltonian for three-phonon process reads [25, 109]

$$\begin{aligned} H^{(1)} =& \frac{1}{3!} \sum_{\boldsymbol{q}\lambda,\boldsymbol{q}'\lambda',\boldsymbol{q}''\lambda''} \left(\frac{\hbar}{2}\right)^{\frac{3}{2}} \frac{1}{\sqrt{N_q}} \frac{V_{\lambda\lambda'\lambda''}}{\sqrt{\omega_\lambda \omega_{\lambda'} \omega_{\lambda''}}} \delta(\boldsymbol{q} + \boldsymbol{q}' + \boldsymbol{q}'', \boldsymbol{Q}) \\ & \times (a^\dagger_{\boldsymbol{q}\lambda} - a_{-\boldsymbol{q}\lambda})(a^\dagger_{\boldsymbol{q}'\lambda'} - a_{-\boldsymbol{q}'\lambda'})(a^\dagger_{\boldsymbol{q}''\lambda''} - a_{-\boldsymbol{q}''\lambda''}) \end{aligned} \tag{2.34}$$

where $a^\dagger$ and a are the phonon creation and annihilation operators, $\boldsymbol{q}$, $\boldsymbol{q}'$, $\boldsymbol{q}''$, λ, λ', λ'', ω_λ, $\omega_{\lambda'}$,$\omega_{\lambda''}$ are the wavevectors, phonon branches and frequencies of the 3 phonons involved. The scattering matrix element $V^{\pm}_{\lambda\lambda'\lambda''}$ is

$$V_{\lambda\lambda'\lambda''} = \sum_{i \in \text{unit cell}} \sum_{j,k} \sum_{\alpha\beta\gamma} \Phi^{\alpha\beta\gamma}_{ijk} \frac{e^\alpha_{\boldsymbol{q}\lambda}(i) e^\beta_{\boldsymbol{q}'\lambda'}(j) e^\gamma_{\boldsymbol{q}''\lambda''}(k)}{\sqrt{M_i M_j M_k}} \tag{2.35}$$

where $\boldsymbol{e}$ is the normalized eigenfunctions of the three phonons involved, $\Phi^{\alpha\beta\gamma}_{ijk}$ is the third-order anharmonic interatomic force constants and M_i is the mass of the ith atom. i, j, k run over atomic indices while α, β and γ denote Cartesian coordinates. Again $N_q = N_{q1} \times N_{q2} \times N_{q3}$ is the number of q-points on the discrete q-mesh used for summation in the reciprocal. Conservation of quasimomentum requires that $\boldsymbol{q}'' = \boldsymbol{q} \pm \boldsymbol{q}' + \boldsymbol{Q}$ for some reciprocal lattice vector $\boldsymbol{Q}$ such that $\boldsymbol{q}''$ is in the same image of the Brillouin zone as $\boldsymbol{q}$ and $\boldsymbol{q}'$. Take case 1 in figure 2-12 as an example, Fermi's golden rule (equation (1.6)) gives the transition rate of

$$W_1 = \frac{\pi\hbar}{4N_q} \frac{|V_{\lambda\lambda'\lambda}|^2}{\omega_\lambda \omega_{\lambda'} \omega_{\lambda''}} n_{\omega_\lambda}(n_{\omega_{\lambda'}}+1)(n_{\omega_{\lambda''}}+1)\delta(\boldsymbol{q} + \boldsymbol{q}' + \boldsymbol{q}'', \boldsymbol{Q})\delta(\omega_\lambda - \omega_{\lambda'} - \omega_{\lambda''}) \tag{2.36}$$

where n represents the phonon's distribution. The factor 1/3! is cancelled out due to

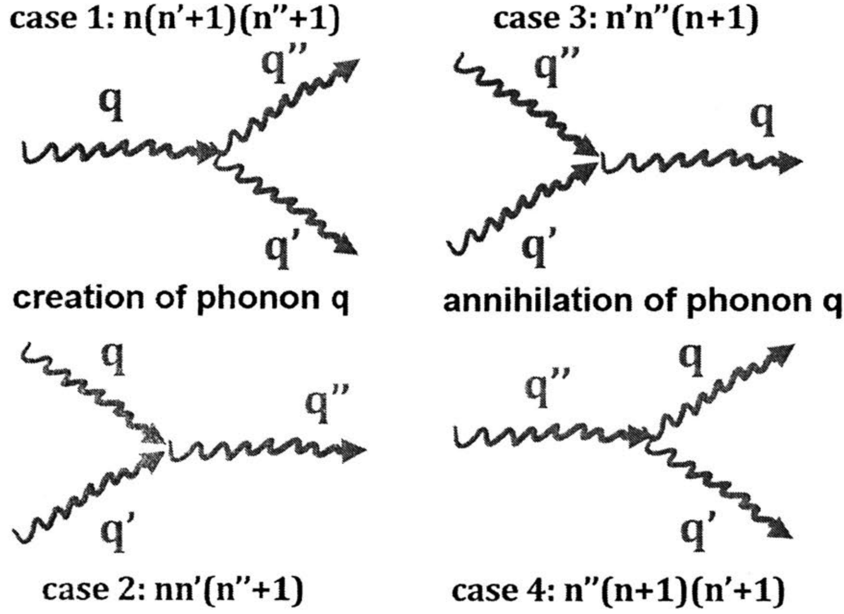

Figure 2-12: Possible three-phonon interactions involving phonons with wavevectors of $\boldsymbol{q}$, $\boldsymbol{q'}$, $\boldsymbol{q''}$. n denotes the distribution of phonon with wavevector of $\boldsymbol{q}$ at branch λ, so as n' for phonon of $\boldsymbol{q'}\lambda'$, n'' for phonon of $\boldsymbol{q''}\lambda''$.

the 3! equivalent terms from the summation in equation (2.34). In the single-mode relaxation time approximation (only phonons in mode $\boldsymbol{q}\lambda$ has a displaced distribution, and all other phonons have their equilibrium distribution), after some algebra, the life time determined by phonon-phonon scattering of the phonon with wavevector $\boldsymbol{q}$, frequency ω and at branch λ, $\tau_{\boldsymbol{q}\lambda,\,\text{phonon-phonon}}$ can be given as [25, 109]

$$\frac{1}{\tau_{\boldsymbol{q}\lambda,\,\text{phonon-phonon}}} = \frac{1}{N_q}\left(\sum_{\lambda'\lambda''}^{+}\Gamma^{+}_{\lambda\lambda'\lambda''} + \sum_{\lambda'\lambda''}^{-}\frac{1}{2}\Gamma^{-}_{\lambda\lambda'\lambda''}\right) \tag{2.37}$$

where "+" indicates the processes in which a phonon is absorbed (two phonons are combined into one) and "-" indicates the processes in which a phonon is emitted (one phonon is split into two). n^0 denotes the Bose-Einstein distribution. The factor 1/2

in the second term is introduced to avoid double counting of equivalent terms.

$$\Gamma^{+}_{\lambda\lambda'\lambda''} = \frac{\hbar\pi}{4}\frac{n^0_{\omega_{\lambda'}} - n^0_{\omega_{\lambda''}}}{\omega_\lambda\omega_{\lambda'}\omega_{\lambda''}}|V_{\lambda\lambda'\lambda}|^2\delta(\omega_\lambda + \omega_{\lambda'} - \omega_{\lambda''}) \tag{2.38}$$

$$\Gamma^{-}_{\lambda\lambda'\lambda''} = \frac{\hbar\pi}{4}\frac{n^0_{\omega_{\lambda'}} + n^0_{\omega_{\lambda''}} + 1}{\omega_\lambda\omega_{\lambda'}\omega_{\lambda''}}|V_{\lambda\lambda'\lambda}|^2\delta(\omega_\lambda - \omega_{\lambda'} - \omega_{\lambda''}) \tag{2.39}$$

The calculation above is carried out in the ShengBTE package [110] using an $80 \times 80 \times 80$ q-mesh and the phonon Boltzmann transport equation is solved under the relaxation time approximation. The calculated phonon-phonon scattering rate is shown in figure 2-13 (since the thermal conductivity that will be discussed in detail in section 3.2 is mostly contributed by phonons with both relatively long life time and large group velocity, which are typical with low phonon frequency, we here only show the scattering rate of those low-frequency phonons). The general trend

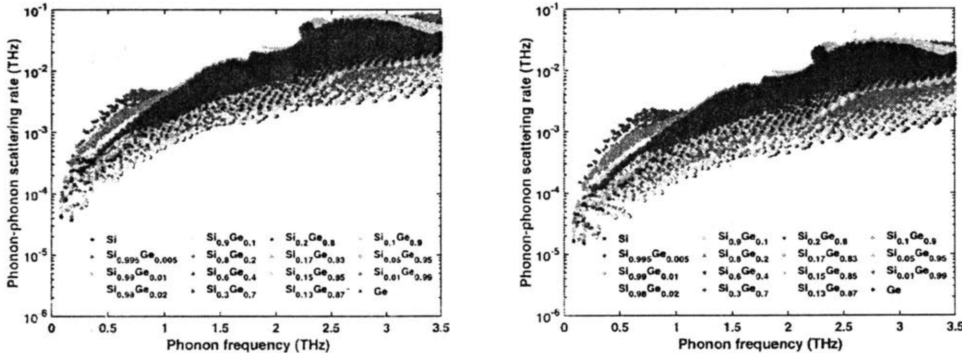

(a) Phonon-phonon scattering rate at 300K

(b) Phonon-phonon scattering rate at 150K

Figure 2-13: Calculated phonon-phonon scattering rate of SiGe alloys at 300K and 150K.

is that phonon-phonon scattering rate is higher at the germanium side than at the silicon side, partially due to the germanium side has lower phonon frequencies (as shown in the phonon dispersion in figure 2-11) thus larger phonon population at a given temperature. However, the anharmonicity, another deciding parameter on the strength of phonon-phonon interaction that is related to the third-order anharmonic interatomic force constants, characterized by the mode-weighted Gruneisen parame-

ter [111], does not change monotonically with composition under our virtual crystal approximation as shown in figure 2-14. The comparison between the scattering rates at the two temperatures shows that phonon-phonon scattering is more prominent at higher temperatures because of larger phonon population.

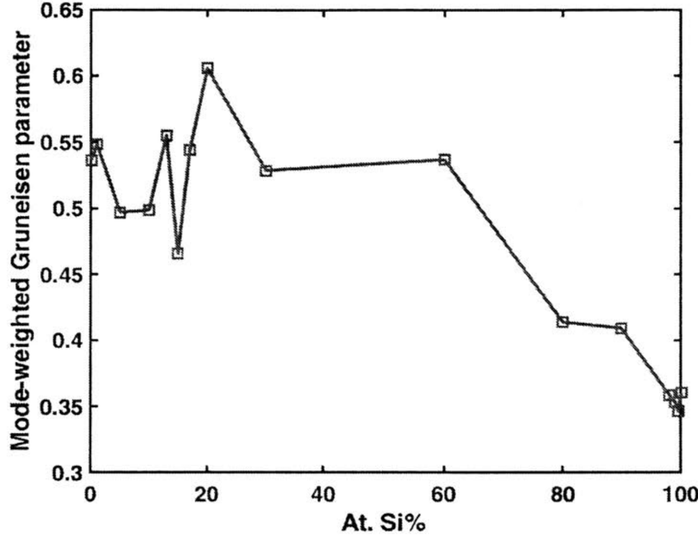

Figure 2-14: Calculated mode-weighted Gruneisen parameter vs. alloy composition.

2.4.2 Phonon Scattering by Electrons

To reduce the computation complexity of the electron-phonon calculations, we make the first-order approximation and assume electrons are at their equilibrium, that is, electrons obey Fermi-Dirac distribution and we do not take the effect of scattering events on electrons' state into account. Later we will use these results for nonequilibrium case when we are calculating the transport properties, assuming the deviation of the electrons' state from equilibrium is small. Same as listing the possible

Table 2.3: Possible electron-phonon scattering events for a phonon

phonon	initial state	final state	momentum relation	energy relation
emitted	$\boldsymbol{k}\alpha$	$\boldsymbol{k}'\beta$	$\boldsymbol{k} - \boldsymbol{k}' - \boldsymbol{q} = 0$	$\varepsilon_{\boldsymbol{k}\alpha} - \varepsilon_{\boldsymbol{k}'\beta} - \hbar\omega_{\boldsymbol{q}\lambda} = 0$
absorbed	$\boldsymbol{k}\alpha$	$\boldsymbol{k}'\beta$	$\boldsymbol{k} + \boldsymbol{q} - \boldsymbol{k}' = 0$	$\varepsilon_{\boldsymbol{k}\alpha} + \hbar\omega_{\boldsymbol{q}\lambda} - \varepsilon_{\boldsymbol{k}'\beta} = 0$

electron-phonon scattering events for an electron in Table 2.2, we list the possible electron-phonon scattering events for a phonon in Table 2.3, which is actually a simplified version of the electron case since the phonon will either be emitted or absorbed (shown in figure 2-15) and there is no need to differentiate between electron's initial and final states. From equation (1.6) Fermi's golden rule, the transition rate of phonon

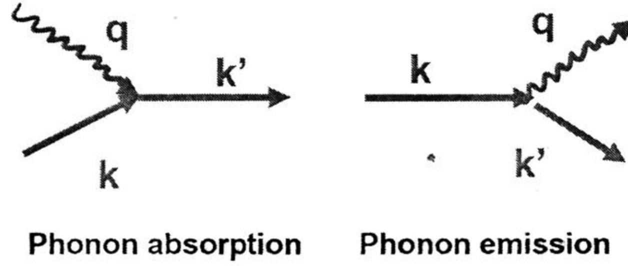

Figure 2-15: Possible electron-phonon interactions involving phonons with wavevector of $\boldsymbol{q}$ and electrons of wavevectors $\boldsymbol{k}$ and $\boldsymbol{k'}$.

of wavevector $\boldsymbol{q}$ at branch λ due to electron-phonon interaction can be expressed as

$$\begin{aligned}\left(\frac{\partial n_{\boldsymbol{q}\lambda}}{\partial t}\right)_{\text{e-ph}} = \frac{1}{N_k}\frac{2\pi}{\hbar}\sum_{\alpha,\beta}\sum_{\boldsymbol{k},\boldsymbol{k'}}\Big[&+ f_{\boldsymbol{k}\alpha}(1-f_{\boldsymbol{k'}\beta})(n_\lambda+1)N_{emit} \\ &- f_{\boldsymbol{k}\alpha}(1-f_{\boldsymbol{k'}\beta})n_\lambda N_{absorb}\Big]\end{aligned} \tag{2.40}$$

where we represent the emission and absorption rate elements as N_{emit} and N_{absorb}.

$$\begin{aligned}N_{emit} &= \left(\frac{\hbar}{2m_0\omega_{\boldsymbol{q}\lambda}}\right)|\langle\boldsymbol{k'}\beta|\partial_{\boldsymbol{q}\lambda}V|\boldsymbol{k}\alpha\rangle|^2\delta(\boldsymbol{k}-\boldsymbol{k'}-\boldsymbol{q})\delta(\varepsilon_{\boldsymbol{k}\alpha}-\varepsilon_{\boldsymbol{k'}\beta}-\hbar\omega_{\boldsymbol{q}\lambda}) \\ N_{absorb} &= \left(\frac{\hbar}{2m_0\omega_{\boldsymbol{q}\lambda}}\right)|\langle\boldsymbol{k'}\beta|\partial_{\boldsymbol{q}\lambda}V|\boldsymbol{k}\alpha\rangle|^2\delta(\boldsymbol{k}+\boldsymbol{q}-\boldsymbol{k'})\delta(\varepsilon_{\boldsymbol{k}\alpha}+\hbar\omega_{\boldsymbol{q}\lambda}-\varepsilon_{\boldsymbol{k'}\beta})\end{aligned} \tag{2.41}$$

Noticing the summations of α and β are over the same possible electronic bands so they are equivalent, same as $\boldsymbol{k}$ and $\boldsymbol{k'}$, we can switch α with β and $\boldsymbol{k}$ with $\boldsymbol{k'}$ at the same time in N_{absorb} to combine N_{emit} and N_{absorb} terms. Again, go through what we did for the electron case in equation (2.23), we will get to the phonon scattering rate

by electrons [25]

$$\begin{aligned}\frac{1}{\tau_{q\lambda,\,\text{el-ph}}} =& \frac{1}{N_k}\frac{2\pi}{\hbar}\sum_{\alpha,\beta}\sum_{k,k'}\left(\frac{\hbar}{2m_0\omega_{q\lambda}}\right)|\langle k'\beta|\partial_{q\lambda}V|k\alpha\rangle|^2(f_{k\alpha}-f_{k'\beta}) \\ & \delta(k-k'-q)\delta(\varepsilon_{k\alpha}-\varepsilon_{k'\beta}-\hbar\omega_{q\lambda})\end{aligned} \quad (2.42)$$

in which the notations are the same with the ones in equation (2.24).

Similar to the calculation of electron scattering rate by phonons in section 2.3.1, we use Wannier method to interpolate the information obtained from DFT and DFPT calculations on the coarse meshes onto an $80 \times 80 \times 80$ k-mesh and an $80 \times 80 \times 80$ q-mesh, use tetrahedra integration method [99] for the integration that loops over the initial and final states while conserving energy. According to the study of Zhou et al. on silicon [32], the major phonons contributing to phonon drag are those near Γ point. We have also tested and justified this in our phonon drag calculations: the calculated phonon drag part of Seebeck of the calculations that only include phonons with wavevector length $|q| \leq 0.2(\frac{2\pi}{a})$ have negligible difference from the results of the calculations that include the full spectrum of phonons. So we further reduce the computational effort by setting a wavevector length range of phonons that will be taken in to account to $|q| \leq 0.2(\frac{2\pi}{a})$, and only calculate those phonons' scattering rate on the dense mesh.

The calculated phonon scattering rate by electrons of SiGe alloys at 300K and 150K are shown in figure 2-16. Because electrons' energy scale is much larger than the energy scale of phonons, that the energy difference between electrons of two very different wavevectors will be way too large for a phonon to provide or carry, phonon with larger wavevectors are less likely to be scattered by electrons. In other words, since the phonon frequency is proportional to the phonon wavevector near the Γ point, as phonon frequency increases, the scattering phase space of phonons will be more restricted by the energy and momentum selection rules and thus get smaller, as we can see the scattering rate decreases with increasing phonon frequency. The trend is that phonon scattering by electrons is higher at the silicon side than at the germanium

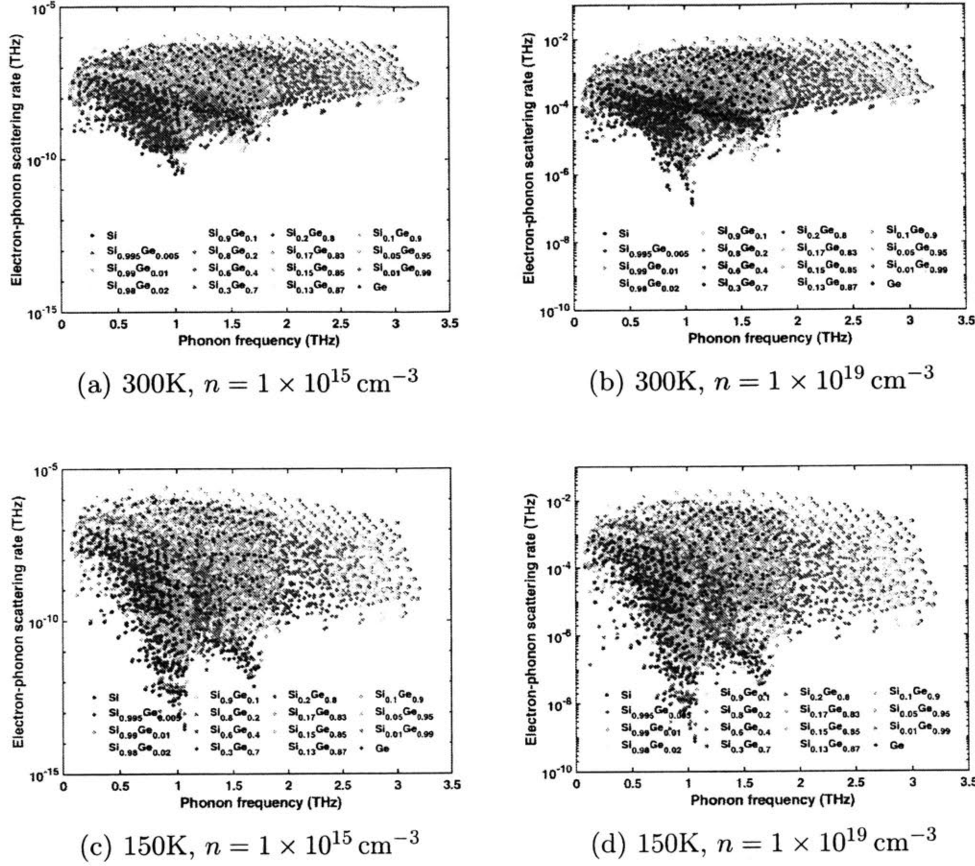

(a) 300K, $n = 1 \times 10^{15}\,\mathrm{cm}^{-3}$

(b) 300K, $n = 1 \times 10^{19}\,\mathrm{cm}^{-3}$

(c) 150K, $n = 1 \times 10^{15}\,\mathrm{cm}^{-3}$

(d) 150K, $n = 1 \times 10^{19}\,\mathrm{cm}^{-3}$

Figure 2-16: Calculated phonon scattering rate by electrons vs. phonon frequency, n denotes the n-type carrier concentration. T = 300K and 150K. (a)(c) of lightly doped n-type SiGe alloys (b)(d) of heavily doped n-type SiGe alloys.

side, which can be explained by the size of the scattering phase space determined by their different phonon dispersion and electronic band structure, as well as the electron-phonon interaction strength that is related to the perturbed potential $\partial V_{\boldsymbol{q}\lambda}$. Generally speaking, the electron-phonon coupling that relates to the perturbed potential $\partial V_{\boldsymbol{q}\lambda}$ is stronger at the Si side than at the Ge side. Figure 2-16 also tells that the phonon scattering rate by electrons is more significant at higher carrier concentrations, for electron-phonon "collisions" in figure 2-15 are more likely to happen when carrier concentration gets higher. Another feature is that the scattering rate decreases faster at lower temperatures with increasing phonon frequency for electron's Fermi-Dirac distribution decays faster with increasing electron energy at lower temperatures.

2.4.3 Alloy Scattering of Phonons

The lattice thermal conductivity of a semiconducting or insulating single crystal alloy is usually lower than the average of the thermal conductivities of the constituent materials. This can be attributed to phonon's scattering by a combined effect of the mass difference, the difference in the elastic constants of the nearest linkages, and of the strain field in alloys [112]. However, taking into account the strain and interatomic force constants difference effects in first-principles calculation would require the self-consistent atomic relaxation of extremely large supercells. Given the difficulties and the minor resulting effect on the total thermal conductivity [113, 59], the force constants differences and strain effect will be neglected here, and the alloy scattering on phonon will be treated as mass-difference scattering.

We adapt an approach from the virtual crystal approximation method in Garg et al.'s work [55] for alloy-phonon scattering rate calculation, where they calculated the phonon modes of the virtual crystal of any given composition, derived from those the frequencies, group velocities, and populations that enter into the calculation of thermal conductivity. As introduced in section 1.4, we construct the virtual crystals using the atomic masses calculated from equation (1.3) and the pseudopotentials calculated from equation (1.4). The lattice parameters are relaxed around their linearly-interpolated values. For each individual composition, the phonon scattering from anharmonicity, electron and boundary can be treated as described in other sections in this chapter. The disordered lattice in the real alloy is replaced by the ordered virtual crystal and the disorder is treated as a perturbation. An atom of the virtual crystal is replaced by an atom of the alloy (Si or Ge) and it acts as a virtual impurity and scatters phonons. In general, the virtual impurity atom would differ from the atoms of the virtual crystal in its mass, size as well as the coupling forces to its neighbors. And as a result of anharmonicity, the coupling forces are modified by the misfit strain field in the neighborhood of the impurity [33]. However, as mentioned above, we here only consider mass-difference scattering.

Klemens [112] has studied the scattering of phonons by static imperfections. By using perturbation theory he has derived expressions for the single-mode phonon relaxation time due to scattering by a substitutional atom of different mass. Tamura's work [70] on isotope scattering also comes down to phonon scattering caused by mass disorder. Their results both show that in highly disordered alloys, high-frequency phonons are strongly scattered (scattering rate $\propto \omega^4$) and the heat is mostly transported by low-frequency phonons that have long mean free path.

Let f_i be the atomic fraction of the atom i, $m_{\text{vca}} = \sum_i f_i m_i$ (this is essentially the same with equation (1.3)) is the average mass in the solid. The perturbation due to mass difference H_{md} is [109]

$$H_{md} = \sum_n \frac{1}{2}(m_{\text{vca}} - m_i)\dot{\boldsymbol{u}}_n^2 \tag{2.43}$$

where $\boldsymbol{u}_n$ is the lattice displacement vector

$$\boldsymbol{u}_n(\boldsymbol{r}) = -i\left(\frac{\hbar}{2N_0 m_0}\right)^{\frac{1}{2}} \sum_{q\lambda} (\omega_{q\lambda})^{-\frac{1}{2}} (a_{q\lambda} - a^{\dagger}_{-q\lambda}) \boldsymbol{e}_{q\lambda} \exp\left[i(\boldsymbol{q}\cdot\boldsymbol{r}_n - \omega t)\right] \tag{2.44}$$

N_0 is the number of unit cell in the crystal and m_0 is the mass of the unit cell. Again with Fermi's golden rule and single-mode relaxation time approximation, the mass-difference scattering rate can be obtained [112, 70]

$$\frac{1}{\tau_{q\lambda}} = \frac{\pi\omega^2}{2N_0} \sum_{q'\lambda'} \delta(\omega_\lambda - \omega_{\lambda'}) \sum_{i\in\text{unit cell}} g(i) |\boldsymbol{e}^*_\lambda(i) \cdot \boldsymbol{e}_{\lambda'}(i)|^2 \tag{2.45}$$

where $\boldsymbol{e}_\lambda(i)$ is the phonon eigenfuntion of mode λ at the ith atom, g is the Pearson deviation coefficient calculated by

$$g(i) = \sum_{i\in\text{Si,Ge}} f_i (1 - \frac{m_i}{m_{\text{vca}}})^2$$

Equation (2.45) is implemented in ShengBTE package [110] to account for scattering from isotopic disorder, and we adapt it for alloy-phonon scattering calculation

since they are essentially the same mass-difference scattering. Klemens and Tamura [112, 70] obtained $\frac{1}{\tau(\omega)} \propto \omega^4$ by further simplifying equation (2.45) using isotropic continuum approximation (which is based on the reasoning that at low temperatures most of the phonons excited in a solid are confined to low-q or long-wavelength acoustic branches. Within this approximation, details of crystal structure are ignored, and the isotropic relation $\omega_{q\lambda} = cq$ with c as the phase velocity, is used for all the normal modes lying within a sphere of radius q). The integration over the Brillouin zone in equation (2.45) is carried out in the ShengBTE package using an $80 \times 80 \times 80$ q-mesh, under the relaxation time approximation to the phonon Boltzmann transport equation. The calculated alloy-phonon scattering rate is shown in figure 2-17. We can see that the alloy-phonon scattering rate is the largest when the silicon content and germanium content are close (approaching the composition of $Si_{0.5}Ge_{0.5}$) which can be intuitively interpreted as that the "randomness" is the greatest at this point. We fit the mass-difference scattering rates with respect to the phonon frequency, and find a good match with Klemens and Tamura's $\frac{1}{\tau(\omega)} \propto \omega^4$ scaling rule for the low-frequency phonons. $Si_{0.6}Ge_{0.4}$ is taken as an example to show the fitting curves in figure 2-17.

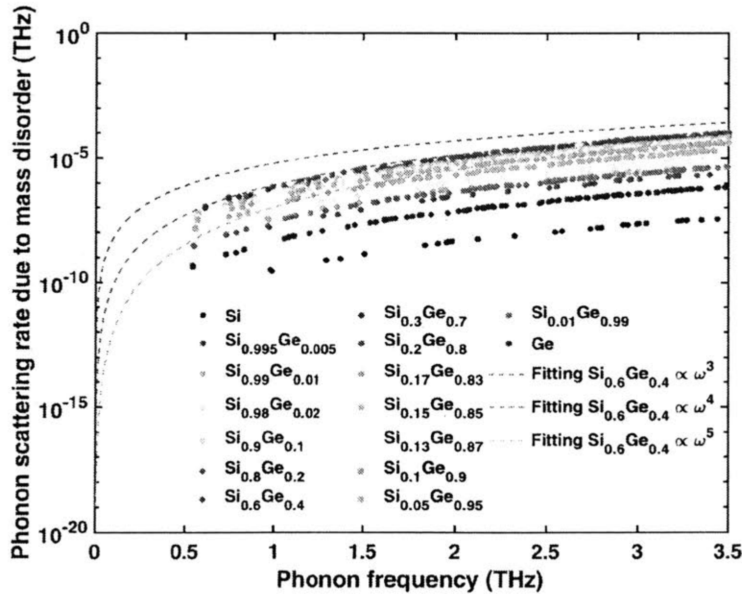

Figure 2-17: Phonon scattering rate due to mass disorder of SiGe alloys.

2.4.4 Boundary Scattering

Sintered (hot pressed) alloys prepared from powder of small grain sizes show marked relative reduction in thermal conductivity over their single crystal (zone-levelled) counterparts. This is because that phonons with mean free path comparable to grain size are likely to suffer strong boundary scattering, over and above other scattering mechanisms listed above, and thus generate extra thermal resistance. Boundary scattering is important for low-dimensional nanostructures, especially at low temperatures when the phonon mean free path is long. We estimate the boundary scattering rate in Casimir limit [114]. The corresponding relaxation time is given by

$$\frac{1}{\tau_{\boldsymbol{q}\lambda,\,\mathrm{boundary}}} = \frac{v_{\boldsymbol{q}\lambda}}{D}$$

where $v_{\boldsymbol{q}\lambda}$ is the phonon's group velocity and D is the characteristic length of the system. This calculation is also carried out using the ShengBTE package.

In our calculation, we use the sample size (the shortest dimension) or the grain size given in the experimental work from [115, 5, 6], as listed in Table 2.4 below.

Table 2.4: Characteristic lengths used in boundary scattering calculations

sample	characteristic length
Si	0.086 cm
Ge	0.13 cm
SiGe alloys	0.0762 cm

In this case, we have found the boundary scattering's contribution to the total phonon scattering rate is minor, compared to the other scattering mechanisms introduced above. This is the case both at 150K and 300K.

Chapter 3

Calculations of Thermoelectric Properties in SiGe Alloys

In this chapter, we will use the electron's and phonon's information (e.g. velocity, energy, relaxation time) obtained from our first-principle calculations to calculate thermoelectric properties of SiGe alloys based on the Boltzmann transport equations for electrons and phonons.

As indicated in the figure of merit zT expression that is given in chapter 1 (equation (1.1)), the thermoelectric properties that we are interested in are electrical conductivity σ, thermal conductivity κ, Seebeck coefficient S. We are going to discuss them separately in the following sections.

3.1 Electrical Properties

3.1.1 Electrical Conductivity and Mobility

Electrical conductivity is the measure of a material's ability to allow the transport of an electric current and it is usually denoted with the Greek letter σ. The field definition gives that $\boldsymbol{J} = \sigma \boldsymbol{E}$ where $\boldsymbol{J}$, $\boldsymbol{E}$ are the current density and the electric field. Generally, σ is a rank-2 tensor. If the material is isotropic, the properties in all directions should be the same. For simplicity, we will derive the properties in x-axis direction and take electrons as the charge carriers (since we are focusing on n-type SiGe alloys) in the following paragraphs.

The energies are defined relative to the conduction band edge ε_c and ε_c is relative to an absolute reference level (and the result should not depend on the reference)[74], recall the linearized Boltzmann transport equation in equation 1.10, for electrons in an electric field only, we have

$$v_{x.\boldsymbol{k}\alpha}\frac{\partial f^0_{\boldsymbol{k}\alpha}}{\partial x} + ev_{x,\boldsymbol{k}\alpha}\frac{\partial \varphi}{\partial x}\frac{\partial f^0_{\boldsymbol{k}\alpha}}{\partial \varepsilon} = -\frac{f_{\boldsymbol{k}\alpha} - f^0_{\boldsymbol{k}\alpha}}{\tau_{\boldsymbol{k}\alpha}} \tag{3.1}$$

where ε is the electron energy, $v_{x,\boldsymbol{k}\alpha}$ is the group velocity along x-axis of the electron with wavevector $\boldsymbol{k}$ at band α, $-e$ is the charge of electron, φ is the electrostatic potential, so the force applied to the electron is $\boldsymbol{F} = -e\boldsymbol{E} = -e(-\frac{\partial \varphi}{\partial x})$. The chain rule gives $\frac{\partial f}{\partial \boldsymbol{k}} = \frac{\partial f}{\partial \varepsilon}\frac{\partial \varepsilon}{\partial \boldsymbol{k}}$. Together with $\boldsymbol{p} = m\boldsymbol{v} = \hbar \boldsymbol{k}$ and $\varepsilon = \frac{1}{2}mv^2$, the $\frac{\boldsymbol{F}}{\hbar}\frac{\partial f}{\partial \boldsymbol{k}}$ term becomes $ev\frac{\partial \varphi}{\partial x}\frac{\partial f}{\partial \varepsilon}$. $f_{\boldsymbol{k}\alpha} - f^0_{\boldsymbol{k}\alpha}$ is the nonequilibrium electrons that contribute to electric flux (equilibrium electrons do not contribute to electric flux) and will be denoted as $\Delta f_{\boldsymbol{k}\alpha}$ below. Equation (3.1) gives

$$\Delta f_{\boldsymbol{k}\alpha} = -\tau_{\boldsymbol{k}\alpha} v_{x,\boldsymbol{k}\alpha}(\frac{\partial f^0_{\boldsymbol{k}\alpha}}{\partial x} + e\frac{\partial \varphi}{\partial x}\frac{\partial f^0_{\boldsymbol{k}\alpha}}{\partial \varepsilon}) \tag{3.2}$$

Then we can write the electric flux in x-axis direction as

$$\begin{aligned} \boldsymbol{J}_{e,x} &= \frac{\sum\limits_{\alpha,\boldsymbol{k}}(-e)v_{x,\boldsymbol{k}\alpha}\Delta f_{\boldsymbol{k}\alpha}}{N_k\Omega} \\ &= \frac{1}{N_k\Omega}(e\sum_{\alpha,\boldsymbol{k}} v_{x,\boldsymbol{k}\alpha}^2\tau_{\boldsymbol{k}\alpha}\frac{\partial f_{\boldsymbol{k}\alpha}^0}{\partial x}) + \frac{1}{N_k\Omega}(e^2\sum_{\alpha,\boldsymbol{k}} v_{x,\boldsymbol{k}\alpha}^2\tau_{\boldsymbol{k}\alpha}\frac{\partial\varphi}{\partial x}\frac{\partial f_{\boldsymbol{k}\alpha}^0}{\partial\varepsilon}) \\ &= e\frac{\partial(an)}{\partial x} + en\mu\boldsymbol{E} \approx ea\frac{\partial n}{\partial x} + en\mu\boldsymbol{E} \end{aligned} \tag{3.3}$$

where Ω is the volume of the unit cell, N_k is the number of the k-points on the discrete k-mesh that we use to sum over the reciprocal space in the calculation, n is the carrier concentration, μ is the mobility and a is the diffusivity. Equation (3.3) tells that the electric flux has contribution both from the drift of electrons driven by the electrostatic field and the diffusion of electrons driven by concentration gradient [74] and the approximation is only valid when the diffusivity is independent of location [116]. From equation (3.3), using $\frac{\partial f^0}{\partial\varepsilon} = \frac{1}{k_BT}f^0(1-f^0)$, the mobility can be written specifically as

$$\mu = -\frac{1}{N_k\Omega}\frac{e^2\sum\limits_{\alpha,\boldsymbol{k}} v_{x,\boldsymbol{k}\alpha}^2\tau_{\boldsymbol{k}\alpha}\frac{\partial f_{\boldsymbol{k}\alpha}^0}{\partial\varepsilon}}{ne} = -\frac{1}{N_k\Omega k_BT}\frac{e^2\sum\limits_{\alpha,\boldsymbol{k}} v_{x,\boldsymbol{k}\alpha}^2\tau_{\boldsymbol{k}\alpha}f_{\boldsymbol{k}\alpha}^0(f_{\boldsymbol{k}\alpha}^0-1)}{ne} \tag{3.4}$$

The electrical conductivity can be obtained as the electrical conductivity σ is related to the mobility μ through

$$\sigma = en\mu \tag{3.5}$$

As discussed in section 2.3, we include the electron-phonon interaction, alloy-electron scattering and ionized impurity scattering while we were calculating the electron relaxation time. Our calculated mobilities at 300K, at four different carrier concentrations are shown in figure 3-1. It is clear that both alloy-electron interaction and ionized impurity scattering have a significant impact on SiGe alloys' mobilities.

We notice that, in the case that the carrier concentration is low or the ionized impurity scattering is not taken into account, the mobilities are the lowest around

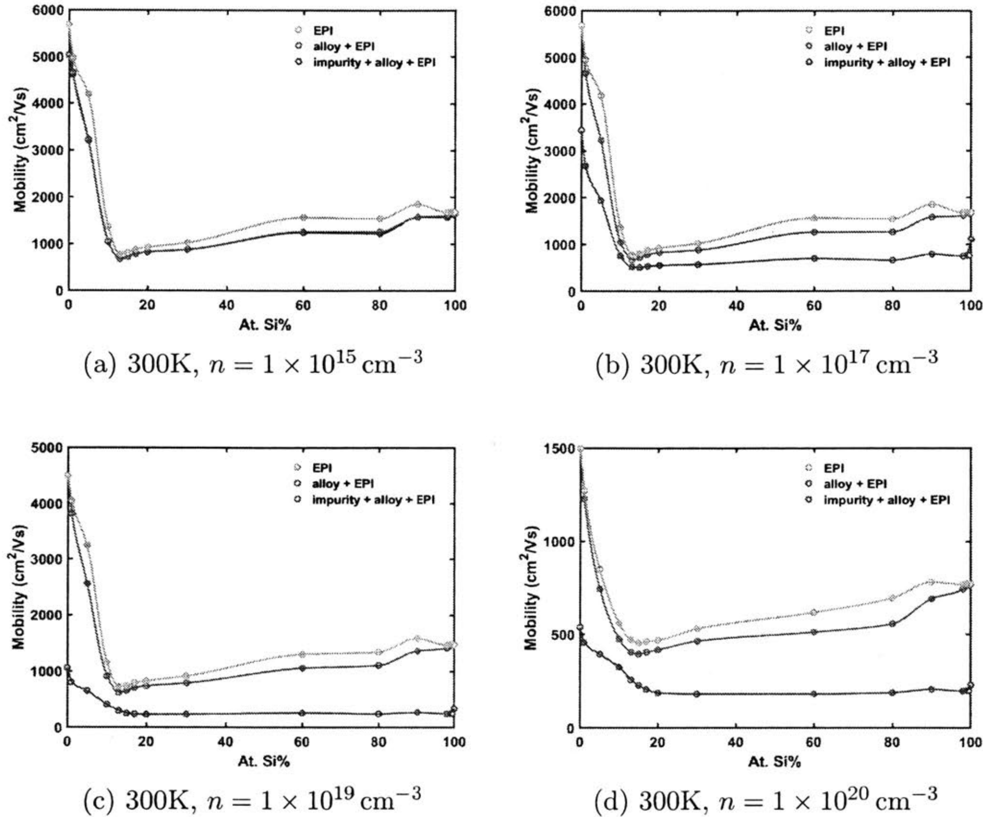

(a) 300K, $n = 1 \times 10^{15}\,\mathrm{cm}^{-3}$

(b) 300K, $n = 1 \times 10^{17}\,\mathrm{cm}^{-3}$

(c) 300K, $n = 1 \times 10^{19}\,\mathrm{cm}^{-3}$

(d) 300K, $n = 1 \times 10^{20}\,\mathrm{cm}^{-3}$

Figure 3-1: Mobilities of SiGe alloys at 300K. Electron-phonon scattering, alloy-electron scattering and ionized impurity scattering are considered.

the composition of $Si_{0}.13Ge_{0.87}$. We attribute it to the band convergence happening at this point that has been discussed in section 2.3.1 and section 2.3.3. Both electron scattering rate by phonons and alloy-electron scattering rate are the highest near the band convergence point as shown in figure 2-3 and figure 2-6 because more electron states that meet the energy conservation and momentum conservation conditions of the electron-phonon or alloy-electron scattering events are available when the two conduction minima are aligned (shown in the lower left corner of figure 2-1). However, when the carrier concentration is high, the long range electrostatic scattering caused by ionized impurity is especially strong and as discussed in section 2.3.3, it has a different trend with the alloy composition (it is stronger at the Si-rich side) from the trends of the other two scattering mechanisms. As the carrier concentration gets higher, the ionized impurity scattering becomes more significant. It lowers the

mobility in Si-rich alloys more than in Ge-rich alloys, thus flattens the mobility curve. The calculated mobilities (considering electron-phonon scattering, alloy-electron scattering and impurity scattering) of SiGe alloys at different carrier concentrations at 150K are shown in figure 3-2. It shared the same trends as what we have discussed before. At lower temperatures, the electron-phonon interaction gets weaker thus the mobility gets higher. The kink in the top curve in figure 3-2 at $Si_{0.8}Ge_{0.2}$ is mostly due to the larger change in alloy-electron scattering rate compared to the change in electron-phonon scattering rate, which can be seen from in figure 2-6 and figure 2-3. And as the carrier concentration increases, this kink is smoothed out by the increasing ionized impurity scattering rate.

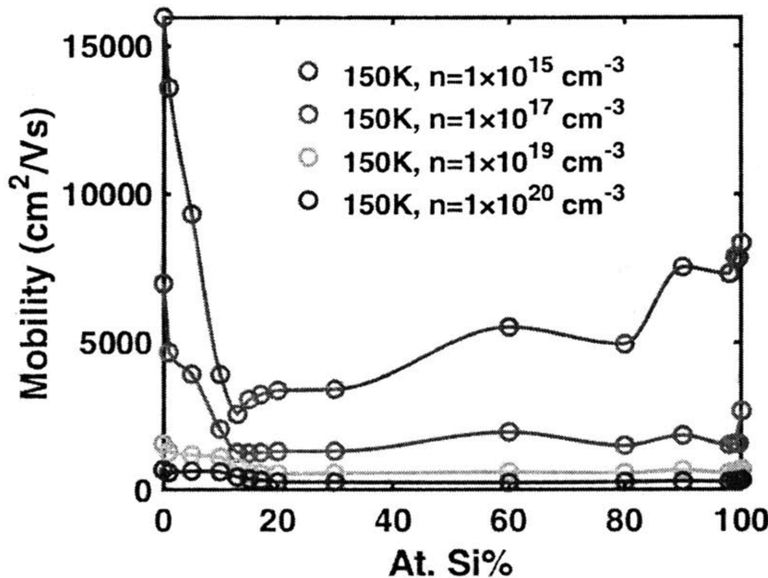

Figure 3-2: Calculated mobilities of SiGe alloys at four different carrier concentrations at 150K. Electron-phonon scattering, alloy-electron scattering and ionized impurity scattering are considered.

The calculated mobilities of pure Ge and $Si_{0.2}Ge_{0.8}$ at different doping concentrations at 300K are compared to the measured results from Fistul et al.'s work [2] and Dismukes et al.'s work [3] in figure 3-3. Again we can see the impurity scattering plays an important role when the carrier concentration is high. After including ionized impurity scattering, the calculated mobility is more in line with the experimental

results.

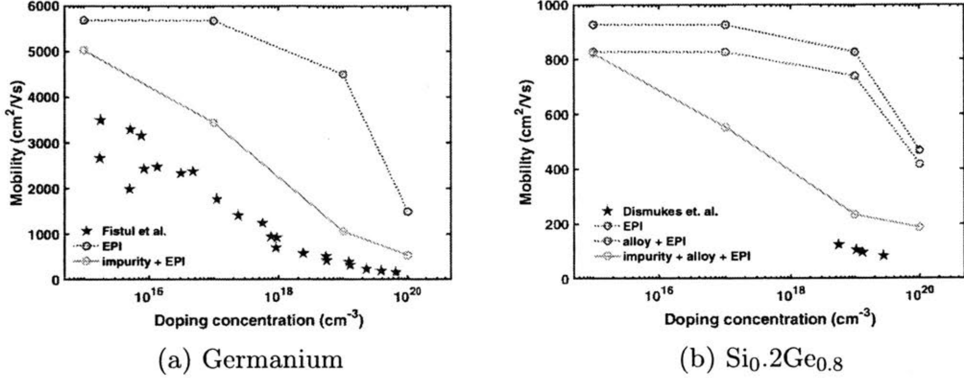

(a) Germanium (b) $Si_0.2Ge_{0.8}$

Figure 3-3: Mobilities of Ge and $Si_0.2Ge_{0.8}$ vs. doping concentration at 300K. The experimental data for germanium is from [2], the experimental data for $Si_{0.2}Ge_{0.8}$ is from [3].

The existing error between our calculated mobilities and experimental data might be due to several things: First, the band structure generated by DFT is not perfectly accurate, especially for the Ge-rich alloys. Secondly, there are other scatters in the materials that we do not take into consideration, e.g. dislocations, stacking faults and other defects. Thirdly, electron-electron scattering tends to equalize the energy among the electrons and thus modifies the mobility [117]. Electron-electron scattering is important for an isotropic material at low concentrations where the electron gas is nondegeneraten[108]. Approximate calculations made by Appel [118] and Bates et al. [119] show electron-electron interaction can further reduce the mobility calculated using the Brooks-Herring model by about 40% at all temperatures. At high concentrations where the electron gas is degenerate, the influence of electron-electron scattering is small because conservation of momentum and energy near the Fermi surface implies conservation of total electron velocity [108]. However, the extra carriers can alter the band structure and there might be more vacancies or vacancy complexes and structural disorder in the material at high concentrations. Other than these three, we also have made many approximations and assumptions while we are dealing with the electron-phonon scattering (e.g. phonons are assumed to be at equilibrium), alloy-electron scattering (e.g. the virtual crystal approximation, only

single scattering is considered and the after-scattering state is described as the undisturbed Bloch state of the periodic host lattice within the first Born approximation) and ionized impurity scattering (e.g. the Brooks-Herring model assigns electrons to plane-wave states, and the core scattering of ionized impurity is not considered), thus our calculations cannot be entirely accurate. Also, there might be certain error in the experimental data itself.

3.1.2 Diffusive Seebeck Coefficient

As introduced in section 1.1, there are two parts that contribute to the Seebeck coefficient, one is caused by the electrons' thermal diffusion due to temperature gradient and the other by phonon drag. The part contributed by electrons' thermal diffusion is sometimes called as diffusive Seebeck coefficient, which is the typical (normal) Seebeck coefficient studied by people.

In section 3.1.1, we wrote down the linearized Boltzmånn transport equation (equation (3.1)) for electrons under the condition of an electric field only. However, it is necessary to include the temperature gradient to study the Seebeck effect. In this case, both the Fermi level and the temperature are functions of location and the $\frac{\partial f^0_{k\alpha}}{\partial x}$ term in the linearized Boltzmann transport equation for electrons becomes $-\frac{\partial f^0_{k\alpha}}{\partial \varepsilon}\frac{d\varepsilon_f}{dx} + \frac{\varepsilon_f-\varepsilon}{T}\frac{\partial f^0_{k\alpha}}{\partial \varepsilon}\frac{dT}{dx}$ using $\frac{\partial f^0}{\partial \varepsilon} = -\frac{\partial f^0}{\partial \varepsilon_f}$ and $\frac{\partial f^0}{\partial T} = \frac{\varepsilon_f-\varepsilon}{T}\frac{\partial f^0}{\partial \varepsilon}$, accordingly equation (3.2) will be changed to

$$\Delta f_{k\alpha} = -\tau_{k\alpha} v_{x,k\alpha}\Big(-\frac{\partial \varepsilon_f}{\partial x} + \frac{\varepsilon_f - \varepsilon}{T}\frac{\partial T}{\partial x} + e\frac{\partial \varphi}{\partial x}\Big)\frac{\partial f^0_{k\alpha}}{\partial \varepsilon} \tag{3.6}$$

Note that equation (3.6) does not take electrons that are driven by nonequilibrium phonons into account. To account for phonon drag effect, an extra term related to the drift of phonon is required [30]. So the "diffusive" contribution to the thermoelectric flux along x-axis which arises when the phonon distribution is held in thermal

equilibrium is

$$
\begin{aligned}
\boldsymbol{J}_{e,x} &= \frac{\sum\limits_{\alpha,\boldsymbol{k}}(-e)v_{x,\boldsymbol{k}\alpha}\Delta f_{\boldsymbol{k}\alpha}}{N_k\Omega} \\
&= -\frac{1}{N_k\Omega}\left(e^2\sum_{\alpha,\boldsymbol{k}} v_{x,\boldsymbol{k}\alpha}^2\tau_{\boldsymbol{k}\alpha}\frac{\partial f_{\boldsymbol{k}\alpha}^0}{\partial\varepsilon}\right)\left(-\frac{\partial\varphi}{\partial x}+\frac{1}{e}\frac{\partial\varepsilon_f}{\partial x}\right) \\
&\quad+\frac{1}{N_k\Omega}\left[e\sum_{\alpha,\boldsymbol{k}} v_{x,\boldsymbol{k}\alpha}^2\tau_{\boldsymbol{k}\alpha}\frac{(\varepsilon-\varepsilon_f)}{T}\frac{\partial f_{\boldsymbol{k}\alpha}^0}{\partial\varepsilon}\right]\left(-\frac{\partial T}{\partial x}\right) \\
&= L_{11}\left(-\frac{\partial\Phi}{\partial x}\right)+L_{12}\left(-\frac{\partial T}{\partial x}\right)
\end{aligned}
\tag{3.7}
$$

As defined in section 3.1.1, the energy of the state ε and the chemical potential ε_f are relative to the conduction band edge ε_c and ε_c is relative to an absolute reference level. With this reference, $\Phi = \varphi - \frac{\varepsilon_f}{e}$ is electrochemical potential, where φ is the electrostatic potential that taken as $-\varepsilon_c/e$ and $(-e)$ is the charge of electron when electrons are taken as the charge carriers [74]. Recall $E_{emf} = -S\nabla T$ in section 1.1 when we introduced the Seebeck coefficient. Here, in the x-axis direction, the electrochemical potential $E_{emf} = -\frac{\partial\Phi}{\partial x}$, we can write the Seebeck coefficient when the drift flux balances out the diffusion flux, i.e. $\boldsymbol{J}_x$ is zero in equation (3.7)

$$
\begin{aligned}
S_{\text{normal}} &= \frac{-\frac{\partial\Phi}{\partial x}}{\frac{\partial T}{\partial x}} = \frac{L_{12}}{L_{11}} = -\frac{1}{eT}\frac{\sum\limits_{\alpha,\boldsymbol{k}} v_{x,\boldsymbol{k}\alpha}^2\tau_{\boldsymbol{k}\alpha}(\varepsilon-\varepsilon_f)\frac{\partial f_{\boldsymbol{k}\alpha}^0}{\partial\varepsilon}}{\sum\limits_{\alpha,\boldsymbol{k}} v_{x,\boldsymbol{k}\alpha}^2\tau_{\boldsymbol{k}\alpha}\frac{\partial f_{\boldsymbol{k}\alpha}^0}{\partial\varepsilon}} \\
&= -\frac{1}{eT}\frac{\sum\limits_{\alpha,\boldsymbol{k}} v_{x,\boldsymbol{k}\alpha}^2\tau_{\boldsymbol{k}\alpha}(\varepsilon-\varepsilon_f)f_{\boldsymbol{k}\alpha}^0(f_{\boldsymbol{k}\alpha}^0-1)}{\sum\limits_{\alpha,\boldsymbol{k}} v_{x,\boldsymbol{k}\alpha}^2\tau_{\boldsymbol{k}\alpha}f_{\boldsymbol{k}\alpha}^0(f_{\boldsymbol{k}\alpha}^0-1)}
\end{aligned}
\tag{3.8}
$$

The calculated normal (diffusive) Seebeck coefficient will be shown in section 3.3.3 together with the phonon drag part.

3.2 Thermal Conductivity

Thermal conductivity is the property of a material's ability to conduct heat and it is often denoted with the Greek letter κ. It appears primarily in Fourier's Law for heat conduction: $\boldsymbol{q} = -\kappa \nabla T$, where $\boldsymbol{q}$ is the local heat flux density and ∇T is the temperature gradient. Like electrical conductivity, thermal conductivity is a rank-2 tensor. But again we will be looking at isotropic materials and in x-axis direction to simplify the problem in the following discussion.

As we know the most common heat carriers are phonon, electron and photon. While in thermoelectric materials, the major ones are phonon and electron and the thermal conductivity could be divided into two parts, $\kappa = \kappa_l + \kappa_e$, where κ_e denotes the part contributed by electron and κ_l denotes the part contributed by phonon. The former is named as the electronic thermal conductivity and the latter as the lattice thermal conductivity.

3.2.1 Lattice Thermal Conductivity

From the definition of the lattice thermal conductivity above, we have

$$\kappa_l = \frac{1}{N_q \Omega} \frac{-\sum\limits_{\lambda,\boldsymbol{q}} \hbar \omega_{\boldsymbol{q}\lambda} v_{\boldsymbol{q}\lambda,x} \Delta n_{\boldsymbol{q}\lambda}}{\frac{\partial T}{\partial x}} \tag{3.9}$$

where $v_{\boldsymbol{q}\lambda,x}$ and $\omega_{\boldsymbol{q}\lambda}$ denote the group velocity along x-axis and the frequency of the phonon with wavevector $\boldsymbol{q}$ at branch λ, $\Delta n_{\boldsymbol{q}\lambda} = n_{\boldsymbol{q}\lambda} - n^0_{\boldsymbol{q}\lambda}$ denotes the nonequilibrium phonons since the equilibrium phonons do not contribute to the heat flux, Ω is the volume of the unit cell and N_q is the number of q-points on the q-mesh on which we sum over in the reciprocal space in our first-principles calculation.

From the linearized Boltzmann transport equation (equation (1.10)) of phonon within the relaxation time approximations

$$v_{q\lambda,x}\frac{\partial n_{q\lambda}^0}{\partial x} = -\frac{n_{q\lambda} - n_{q\lambda}^0}{\tau_{q\lambda}} \tag{3.10}$$

we have

$$\Delta n_{q\lambda} = -\tau_{q\lambda}v_{q\lambda,x}\frac{\partial T}{\partial x}\frac{\partial n_{q\lambda}^0}{\partial T} \tag{3.11}$$

Plug this into the expression of the lattice thermal conductivity above and use $\frac{\partial n_{q\lambda}^0}{\partial T} = -\frac{\hbar\omega_{q\lambda}}{k_B T^2} n_{q\lambda}^0(n_{q\lambda}^0 + 1)$, we get

$$\kappa_l = \frac{1}{k_B T^2 N_q \Omega}\sum_{\lambda,q} n_{q\lambda}^0(n_{q\lambda}^0 + 1)(\hbar\omega_{q\lambda})^2 v_{x,q\lambda}^2 \tau_{q\lambda} \tag{3.12}$$

A previous study in silicon [58] shows that electron-phonon interaction can significantly reduce the lattice thermal conductivity when the carrier concentration is high, thus we take this effect into account while calculating our zT values. However, for the case of SiGe alloy, it has been well-known that the lattice thermal conductivity has already been largely reduced by alloy-phonon scattering, and it was not clear that if electron-phonon interaction would further reduce the lattice thermal conductivity significantly. We investigate the effect of electron-phonon interaction on the lattice thermal conductivity of SiGe alloys by comparing the calculated the lattice thermal conductivities of SiGe alloys in both cases where we consider electron-phonon interaction and do not consider electron-phonon interaction. Other than electron-phonon interaction, as described in section 2.4, we include intrinsic phonon-phonon scattering, alloy-phonon scattering and boundary scattering in the Casimir limit [114] while calculating the lattice thermal conductivity of SiGe alloys. We use the effective relaxation time $\tau_{q\lambda}$ ontained from Matthiessen's rule $\frac{1}{\tau_{q\lambda}} = \sum \frac{1}{\tau_j}$ where j indicates different scattering mechanisms [92]. The integration over the Brillouin zone in equation (3.12) is carried out in the ShengBTE package using a $60 \times 60 \times 60$ q-mesh, under the relaxation time approximation to the phonon Boltzmann transport equation. Figure 3-4 shows the comparison between our calculated lattice thermal conductivity of SiGe alloys at room temperature with literature. Steele's samples include both n-type and

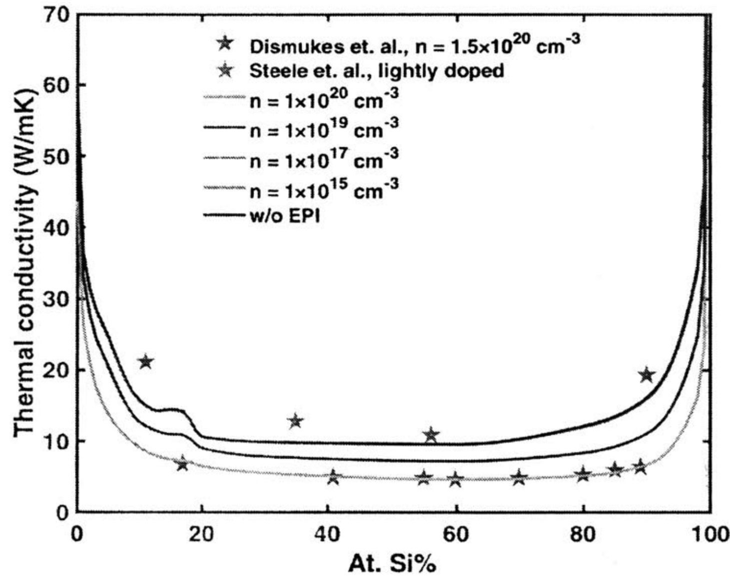

Figure 3-4: Calculated lattice thermal conductivity of SiGe alloys at four different carrier concentrations at 300K compared to experiments [3, 4].

p-type ones, and the electrical resistivity varies from 2 to 70 $\Omega{\cdot}$cm (having an electrical resistivity of $0.006\,\Omega \cdot$ cm is approximately equivalent to having a carrier concentration of $1.2 \times 10^{18}\,\mathrm{cm}^{-3}$) [4]. We can regard them all as lightly doped samples (should be lower than $10^{17}\,\mathrm{cm}^{-3}$). Dismukes et.al. [3] measured the thermal conductivity of n-type SiGe alloys with a carrier concentration of $1.5 \times 10^{20}\,\mathrm{cm}^{-3}$, with which our calculated heavily doped (with a carrier concentration of $1 \times 10^{20}\,\mathrm{cm}^{-3}$) SiGe alloys' lattice thermal conductivity shows very good agreement. We should note that, in figure 3-4, the experimental data includes the electronic component of the thermal conductivity, while our result here is the lattice thermal conductivity only. We also calculate the electronic part of thermal conductivity and show it in figure 3-10. It is around $1.5\,W/mK$ at the carrier concentration of $1 \times 10^{20}\,\mathrm{cm}^{-3}$. However, since the experimental data from Dismukes is with a larger carrier concentration, it makes sense that its lattice thermal conductivity plus the electronic thermal conductivity matches our calculated lattice thermal conductivity reasonably well. Our calculated lattice thermal conductivity of SiGe alloys at 150K is also given in figure 3-5. The curves basically share the same trend with the ones in figure 3-4 but the absolute

values of the lattice thermal conductivity increase compared to 300K. This is due to that phonon-phonon interaction becomes much weaker for less phonons are populated at lower temperatures. While phonon scattering by electrons is less affected by temperature as discussed in section 2.4.1, and electron-phonon scattering becomes more significant at higher carrier concentrations, the increase in the lattice thermal conductivity with decreasing temperature is more prominent at low carrier concentrations than at high carrier concentrations.

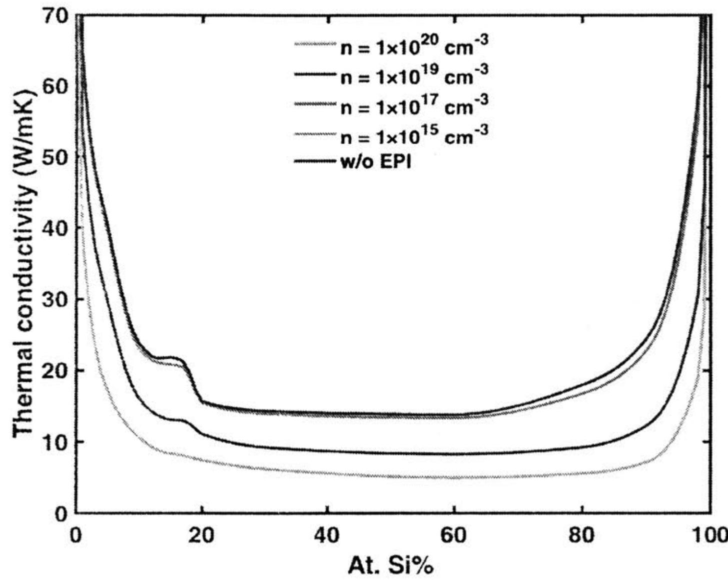

Figure 3-5: Calculated lattice thermal conductivity at four different carrier concentrations of SiGe alloys at 150K.

As we can see in figure 3-4, the last three curves ($n = 10^{17}\,\mathrm{cm}^{-3}$, $n = 10^{15}\,\mathrm{cm}^{-3}$ and without EPI) almost overlap completely, which means that at low carrier concentration, electron-phonon interaction has a minor effect on the lattice thermal conductivity, intrinsic phonon scattering and alloy-phonon scattering are the dominant scattering mechanisms. However, as the carrier concentration goes above $n = 10^{20}\,\mathrm{cm}^{-3}$, the reduction of the lattice thermal conductivity due to electron-phonon interaction (EPI) becomes much more significant. We further plot the reduction in terms of percentage in figure 3-6, which shows at 300K, the reduction in the lattice thermal conductivity due to EPI ranges from $30 - 60\%$ across all the alloys compositions,

and the reduction increases to 35 – 70% at 150K. The degree of reduction is intuitively determined by the relative strength of electron-phonon scattering compared to the sum of intrinsic phonon scattering and alloy-phonon scattering. As shown in figure 2-13 and figure 2-17, the phonon-phonon scattering rate increases with Ge content, while the alloy-phonon scattering rate would first increases with Ge content when Ge content is low (< 50%) and then decreases with Ge content when it is high (> 50%). The opposite trends and relatively close absolute values of the slopes of intrinsic phonon scattering rate vs. alloy composition and alloy-phonon scattering rate vs. alloy composition lead to the short plateau in the last three curves as well as and the peak in the lattice thermal conductivity reduction in figure 3-6 around the composition of $Si_{0.15}Ge_{0.85}$. In other words, since the intrinsic phonon scattering and alloy-phonon scattering are the dominant scattering mechanisms at low carrier concentrations, as Si content increases, there will be a point at which the increase in alloy-phonon scattering rate compensates the decrease in intrinsic phonon scattering thus the lattice thermal conductivity will stay almost constant near this point. As the electron-phonon interaction keeps getting stronger with increasing Si content (shown in figure 2-16), the reduction percentage will reach a local maximum around this point shown in figure 3-6. There is no alloy-phonon scattering for pure Si or pure

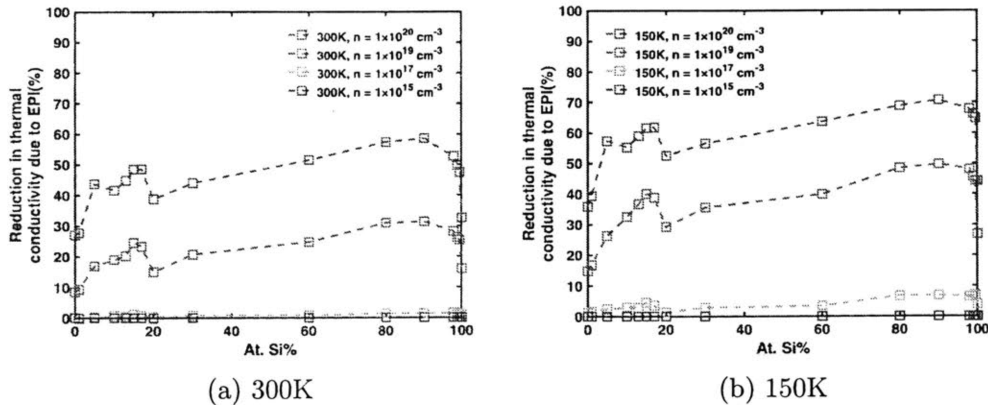

(a) 300K (b) 150K

Figure 3-6: Reduction in SiGe alloys' lattice thermal conductivity in terms of percentage due to electron-phonon interaction.

Ge. The intrinsic phonon scattering is the weakest and the electron-phonon interac-

tion is the strongest at pure Si while Ge has the opposite case according to figure 2-13 and figure 2-16, therefore the reduction percentage in Ge is lower than in Si. However, it is not clear why the reduction percentage in pure Si is much smaller than its neighboring Si-rich alloys, since both intrinsic phonon scattering rate and alloy-phonon scattering rate decreases while electron-phonon scattering rate increases with increasing Si content in this region. We further do some spectrum analysis to explain this counter-intuitive feature. Figure 3-7 shows accumulated lattice thermal conduc-

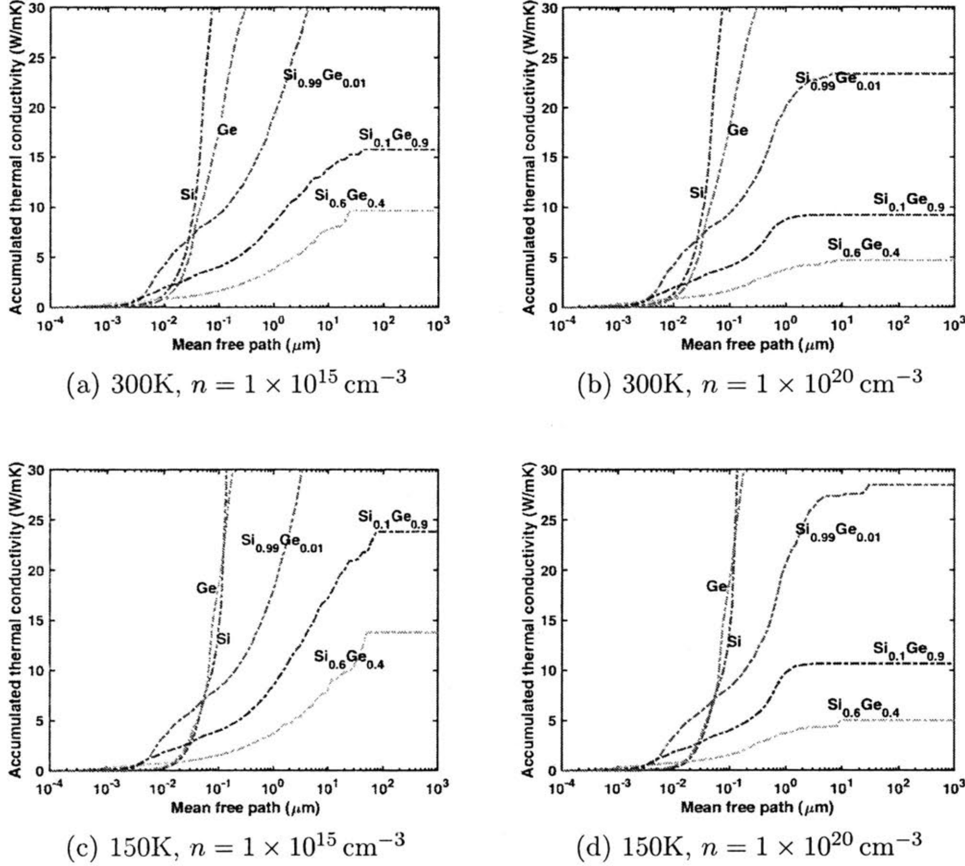

(a) 300K, $n = 1 \times 10^{15}\,\mathrm{cm}^{-3}$ (b) 300K, $n = 1 \times 10^{20}\,\mathrm{cm}^{-3}$

(c) 150K, $n = 1 \times 10^{15}\,\mathrm{cm}^{-3}$ (d) 150K, $n = 1 \times 10^{20}\,\mathrm{cm}^{-3}$

Figure 3-7: Accumulated lattice thermal conductivity vs. phonon mean free path in lightly doped and heavily doped SiGe alloys. (a)(b)T = 300K, (c)(d) T = 150K. The y-axis is cut and the maximum value is set to $30W/mK$ to show the difference between the curves of alloys at different temperatures and different doping concentrations more clearly.

tivity versus phonon mean free path in lightly doped and heavily doped SiGe alloys. By comparing the curves of pure Si and Ge and the curves of alloys in each subfigure,

we know that alloy scatters heavily on phonons with mean free path of $\leq 10\,\mu m$. By comparing figure 3-7a and figure 3-7b, as well as figure 3-7c and figure 3-7d, we know that electron-phonon interaction has an impact on phonons with mean free path $\geq 1\,\mu m$ thus can further reduce the lattice thermal conductivity. In other words, the phonons scattered by electrons and the phonons scattered by mass difference in the alloys are spectrally different. This justifies that the reduction in the lattice thermal conductivity caused by electron-phonon interaction in Si-rich alloys is more significant than in pure Si in terms of percentage. Figure 3-8 takes $Si_{0.1}Ge_{0.9}$ as an example and shows the mean free path distribution for phonons with different frequencies in three cases. Similarly, the phonon scattering rate of phonons with different frequencies of

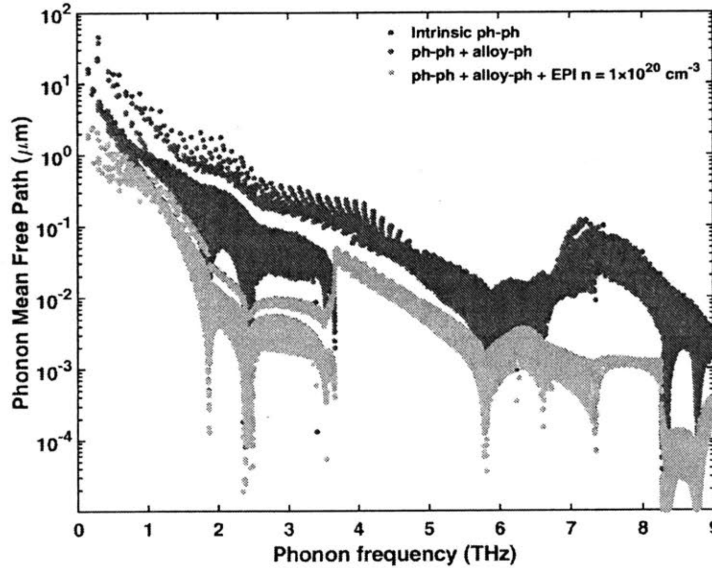

Figure 3-8: Phonon mean free path determined by intrinsic phonon scattering, alloy-phonon scattering and electron-phonon scattering vs. phonon frequency, taking $Si_{0.1}Ge_{0.9}$ as an example.

$Si_{0.1}Ge_{0.9}$ is plotted in figure 3-9 in three cases. By comparing the three cases, we can see the low frequency phonons are greatly scattered by the electrons over and above other phonons and mass disorder in alloys, while the high frequency ones are heavily scattered by mass disorder in the alloy. Figure 3-8 and figure 3-9 together show that, at high carrier concentration (here $n = 1 \times 10^{20}\,\mathrm{cm}^{-3}$) electron-phonon scattering is

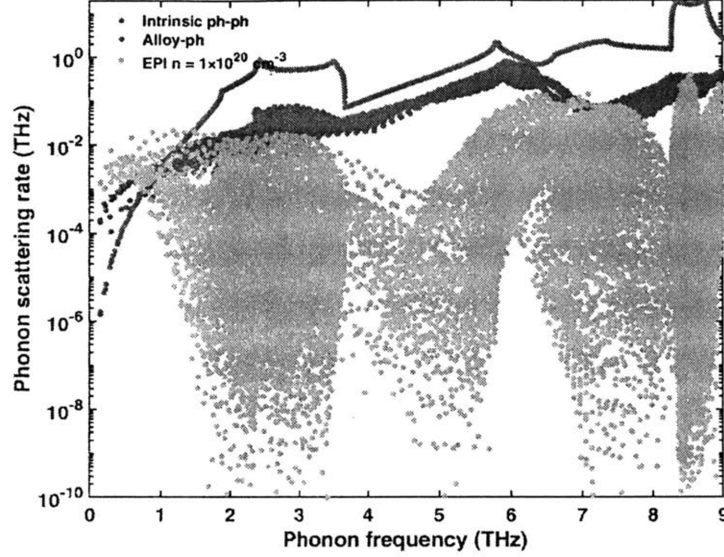

Figure 3-9: Intrinsic phonon scattering rate, alloy-phonon scattering rate and electron-phonon scattering rate vs. phonon frequency, taking $Si_{0.1}Ge_{0.9}$ as an example.

the dominant scattering mechanism for low-frequency and long-wavelength phonons hence it is important to include EPI in the lattice thermal conductivity calculations.

3.2.2 Electronic Thermal Conductivity

Similar to equation (3.7) of electric flux, we can write down the expression of the heat flow when there are both electric field and temperature gradient as below [74]

$$\boldsymbol{J}_{q,x} = \boldsymbol{J}_{\varepsilon,x} - \varepsilon_f \boldsymbol{J}_{n,x} = \frac{\sum_{\alpha,\boldsymbol{k}} (\varepsilon - \varepsilon_f) v_{x,\boldsymbol{k}\alpha} \Delta f_{\boldsymbol{k}\alpha}}{N_k \Omega} \tag{3.13}$$

where $\boldsymbol{J}_{q,x}$, $\boldsymbol{J}_{\varepsilon,x}$, $\boldsymbol{J}_{n,x}$ are the heat flux, the energy flux, and the particle flux along x-axis. Again $v_{x,\boldsymbol{k}\alpha}$ and ε are the group velocity along x-axis and energy of the electron with wavevector $\boldsymbol{k}$ at band α, ε_f is the Fermi level, $\Delta f_{\boldsymbol{k}\alpha} = f_{\boldsymbol{k}\alpha} - f^0_{\boldsymbol{k}\alpha}$ is the nonequilibrium electrons that contributes to heat flux, Ω is the volume of the unit cell and N_k is the number of the k-points on the k-mesh on which we sum over in the

calculation. Plug equation (3.6) into equation (3.13), we will get

$$
\begin{aligned}
\boldsymbol{J}_{q,x} &= \frac{1}{N_k \Omega}\Big[\sum_{\alpha,k}(\varepsilon - \varepsilon_f) v_{x,k\alpha}^2 \tau_{k\alpha} \frac{\partial f_{k\alpha}^0}{\partial \varepsilon}\Big]\Big(-\frac{\partial \varphi}{\partial x} + \frac{1}{e}\frac{\partial \varepsilon_f}{\partial x}\Big) \\
&+ \frac{1}{N_k \Omega}\Big[\sum_{\alpha,k}(\varepsilon - \varepsilon_f)^2 v_{x,k\alpha}^2 \tau_{k\alpha} \frac{\partial f_{k\alpha}^0}{\partial \varepsilon}\Big]\Big(-\frac{\partial T}{\partial x}\Big) \\
&= L_{21}\Big(-\frac{\partial \Phi}{\partial x}\Big) + L_{22}\Big(-\frac{\partial T}{\partial x}\Big)
\end{aligned}
\tag{3.14}
$$

We can use equation (3.7) to eliminate the electrochemical potential term and obtain

$$
\boldsymbol{J}_{q,x} = \frac{L_{21}}{L_{11}} \boldsymbol{J}_{e,x} + \left(L_{22} - \frac{L_{12}L_{21}}{L_{11}}\right)\Big(-\frac{\partial T}{\partial x}\Big) \tag{3.15}
$$

where $\Pi = \frac{L_{21}}{L_{11}} = T\frac{L_{12}}{L_{11}} = TS$ is the Peltier coefficient and $\kappa_e = L_{22} - \frac{L_{12}L_{21}}{L_{11}}$ is the electronic thermal conductivity.

While for metals, the electron density is very large and the transport does not affect the Fermi level, and a common method to estimate the electronic thermal conductivity is the Wiedemann-Franz law,

$$
\kappa_e = L\sigma T \tag{3.16}
$$

where T is the temperature, L is the Lorenz number, usually treated as a constant ($2.44 \times 10^{-8}\, W\Omega K^{-2}$) with slight changes for most of metals (for semiconductors, the Lorenz number needs to be calculated using $L = \kappa_e/(\sigma T)$ for doping would change the Fermi level, but the magnitude of it would not vary much [74]). This is based upon the fact that the heat transport (electrons are the dominant heat carriers in metals) and the electrical transport both involve the free electrons in the metal: the thermal conductivity increases with increasing average particle velocity since that increases the forward transport of energy. The electrical conductivity decreases with increasing particle velocity because the collisions divert the electrons from forward transport of charge. This means that the ratio of thermal to electrical conductivity depends upon the average velocity squared, which is proportional to the kinetic temperature.

Our calculated results at room temperature (all the scattering mechanisms discussed in chapter 2 are considered) in figure 3-10 show that, at the carrier concentration of $10^{19}\,\mathrm{cm}^{-3}$, the electronic thermal conductivity is still much smaller ($\kappa_e/\kappa_l < 3\%$) than the lattice thermal conductivity with electron-phonon interaction taken in to account. The electronic thermal conductivity is typically about $1.5\,W/mK$ and the κ_e/κ_l ratio varies from 2% to 35% when the carrier concentration goes to $10^{20}\,\mathrm{cm}^{-3}$. In most semiconductors, the electronic thermal conductivity is generally much smaller than the lattice thermal conductivity in the considered range of carrier concentrations (lower than $10^{20}\,\mathrm{cm}^{-3}$).

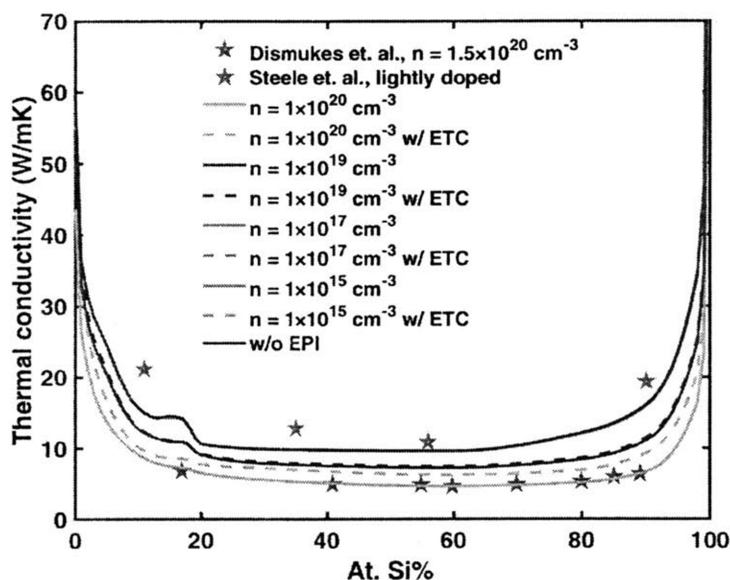

Figure 3-10: Thermal conductivity (including the electronic part) of SiGe alloys at 300K compared to experiments [3, 4]

3.3 Seebeck Coefficient Contributed by Phonon Drag

3.3.1 Formula Derivation

As given in section 1.2, the previous diffusive picture of Seebeck effect only accounts for the case where there is no phonon flowing between the two ends of the material. But when there is a temperature gradient, there are phonons travelling from hot side to cold side and during this process, phonons could "drag" the electrons to travel with them, and this increases the Seebeck coefficient.

Below we will derive the phonon drag formula in the Peltier picture (the isothermal electric field produces a heat flow, actually in this case it is "electron drag" rather than phonon drag: electrons driven by the electric field drag phonons to travel with them), solving the coupled electron-phonon linearized Boltzmann transport equations by partially decoupling the electron and phonon transport [30]. Again we take the material to be isotropic, thus we can simplify the problem by looking at one direction (e.g. along x-axis) since the three directions are equivalent.

In the Peltier picture below, there is no temperature gradient along x-axis at the beginning so we assume the phonons are at equilibrium. There is 1-D electric current along x-axis so there are nonequilibrium electrons at the initial state. The Peltier effect will gradually form a temperature difference and the equilibrium of phonon will be disturbed.

Writing down the linearized Boltzmann transport equation (equation (1.10)) for electron

$$v_{x,\boldsymbol{k}\alpha}\frac{\partial f^0_{\boldsymbol{k}\alpha}}{\partial T}\frac{\partial T}{\partial x}+ev_{x,\boldsymbol{k}\alpha}\frac{\partial f^0_{\boldsymbol{k}\alpha}}{\partial \varepsilon}\frac{\partial \varphi}{\partial x}=-\frac{f_{\boldsymbol{k}\alpha}-f^0_{\boldsymbol{k}\alpha}}{\tau_{\boldsymbol{k}\alpha}}+\left(\frac{\partial f_{\boldsymbol{k}\alpha}}{\partial t}\right)_{\text{e-ph}} \tag{3.17}$$

In the first term on the right hand side of equation (3.17), we assume that all other scattering mechanisms except the electron-phonon interaction can be described

by the mode-dependent relaxation time model, that is, the relaxation time approximation can include interactions like alloy-electron, impurity-electron by using an effective relaxation time $\tau_{\boldsymbol{k}\alpha}$, according to the Matthiessen's rule $\tau_{\boldsymbol{k}\alpha} = \sum \frac{1}{\tau_{\boldsymbol{k}\alpha, j}}$ where j indicates different scattering mechanisms [92].

Denote the distribution function as $n_{\boldsymbol{q}\lambda}$ for the phonon at branch λ with wavevector $\boldsymbol{q}$, the linearized Boltzmann transport equation for phonons is

$$v_{\boldsymbol{q}\lambda,x} \frac{\partial n^0_{\boldsymbol{q}\lambda}}{\partial T} \frac{\partial T}{\partial x} = -\frac{n_{\boldsymbol{q}\lambda} - n^0_{\boldsymbol{q}\lambda}}{\tau_{\boldsymbol{q}\lambda}} + \left(\frac{\partial n_{\boldsymbol{q}\lambda}}{\partial t} \right)_{\text{e-ph}} \tag{3.18}$$

Similarly, the first term on the right hand side of equation (3.18) can include interactions like phonon-phonon scattering, alloy-phonon scattering and boundary scattering by using the Matthiessen's rule to obtain an effective relaxation time [92].

In the Peltier picture, there is no thermal gradient, this simplifies equation (3.18) to

$$\frac{n_{\boldsymbol{q}\lambda} - n^0_{\boldsymbol{q}\lambda}}{\tau_{\boldsymbol{q}\lambda}} = \frac{\Delta n_{\boldsymbol{q}\lambda}}{\tau_{\boldsymbol{q}\lambda}} = \left(\frac{\partial n_{\boldsymbol{q}\lambda}}{\partial t} \right)_{\text{e-ph}} \tag{3.19}$$

The Peltier coefficient

$$\Pi = TS = \frac{\text{induced heat flux}}{\text{electric current flux}}$$

$$= \frac{\text{heat carried by charge carriers + by phonons dragged by travelling charge carriers}}{\text{electric current flux}}$$

$$= \Pi_{\text{normal}} + \Pi_{\text{phonon drag}} = T(S_{\text{normal}} + S_{\text{phonon drag}})$$

where in our calculations,

$$\Pi_{\text{normal}} = \frac{\frac{1}{N_k} \sum\limits_{\alpha,\boldsymbol{k}} v_{x,\boldsymbol{k}\alpha} (\varepsilon_{\boldsymbol{k}\alpha} - \varepsilon_f) \Delta f_{\boldsymbol{k}\alpha}}{\frac{1}{N_k} \sum\limits_{\alpha,\boldsymbol{k}} (-e) v_{x,\boldsymbol{k}\alpha} \Delta f_{\boldsymbol{k}\alpha}} \tag{3.20}$$

$$\Pi_{\text{phonon drag}} = \frac{\frac{1}{N_q}\sum_{\lambda,\boldsymbol{q}} \hbar\omega_{\boldsymbol{q}\lambda} v_{x,\boldsymbol{q}\lambda} \Delta n_{\boldsymbol{q}\lambda}}{\frac{1}{N_k}\sum_{\alpha,\boldsymbol{k}} (-e) v_{x,\boldsymbol{k}\alpha} \Delta f_{\boldsymbol{k}\alpha}} \tag{3.21}$$

To find out the $\left(\frac{\partial f_{\boldsymbol{k}\alpha}}{\partial t}\right)_{\text{e-ph}}$ term, let us go back to equation (2.22). As we assume that at the initial state, phonons are at equilibrium, though afterwards its equilibrium will be disturbed by the nonequilibrium electrons, the effect of the nonequilibrium phonons caused by the "electron drag" on electrons' state is a higher order effect which is relatively minor. We will use the first-order approximation to neglect the $\Delta n_{\boldsymbol{q}\lambda}$ term and replace the $n_{\boldsymbol{q}\lambda}$ with the Bose-Einstein distribution $n^0_{\boldsymbol{q}\lambda}$. We will also neglect the $\Delta f_{\boldsymbol{k}\alpha} \Delta f_{\boldsymbol{k}'\beta}$ term as a first-order approximation. After some algebra, equation (2.22) can be rearranged as:

$$\begin{aligned}\left(\frac{\partial f_{\boldsymbol{k}\alpha}}{\partial t}\right)_{\text{e-ph}} = \frac{2}{N_q}\frac{2\pi}{\hbar}\Bigg\{ &- \Big[\sum_{\boldsymbol{q}\lambda,\boldsymbol{k}'\beta} (n^0_{\boldsymbol{q}\lambda} + f^0_{\boldsymbol{k}'\beta})G^- + (n^0_{\boldsymbol{q}\lambda} + 1 - f^0_{\boldsymbol{k}'\beta})G^+ \Big] \Delta f_{\boldsymbol{k}\alpha} \\ &+ \sum_{\boldsymbol{q}\lambda,\boldsymbol{k}'\beta} \left[(n^0_{\boldsymbol{q}\lambda} + 1 - f^0_{\boldsymbol{k}\alpha})G^- + (n^0_{\boldsymbol{q}\lambda} + f^0_{\boldsymbol{k}\alpha})G^+ \right] \Delta f_{\boldsymbol{k}'\beta} \Bigg\}\end{aligned} \tag{3.22}$$

where G^- and G^+ are given in equation (2.25)

Notice that the first term on the right hand side of equation (3.22) can be combined with the first term on the right hand side of the linearized Boltzmann transport equation (equation (3.17)) using the relaxation time approximation. And another approximation is to assume the second term on the right hand side on equation (3.22) will vanish [107]. With these approximations listed above, equation (3.17) is simplified to

$$e v_{x,\boldsymbol{k}\alpha} \frac{\partial f^0_{\boldsymbol{k}\alpha}}{\partial \varepsilon} \frac{\partial \varphi}{\partial x} = -\frac{f_{\boldsymbol{k}\alpha} - f^0_{\boldsymbol{k}\alpha}}{\tau_{\boldsymbol{k}\alpha}} = -\frac{\Delta f_{\boldsymbol{k}\alpha}}{\tau_{\boldsymbol{k}\alpha}} \tag{3.23}$$

Rewrite equation (3.23) and equation (3.19), we have

$$\Delta f_{\boldsymbol{k}\alpha} = -e\tau_{\boldsymbol{k}\alpha} v_{x,\boldsymbol{k}\alpha} \frac{\partial f^0_{\boldsymbol{k}\alpha}}{\partial \varepsilon} \frac{\partial \varphi}{\partial x} \tag{3.24}$$

$$\Delta n_{\boldsymbol{q}\lambda} = \tau_{\boldsymbol{q}\lambda} \left(\frac{\partial n_{\boldsymbol{q}\lambda}}{\partial t} \right)_{\text{e-ph}} \tag{3.25}$$

If the carrier concentration is assumed to be uniform throughout the material, we can neglect the diffusion term in equation 3.3 and have

$$\boldsymbol{J}_{e,x} = \frac{\sum\limits_{\alpha,\boldsymbol{k}} (-e) v_{x,\boldsymbol{k}\alpha} \Delta f_{\boldsymbol{k}\alpha}}{N_k \Omega} = \sigma(-\frac{\partial \varphi}{\partial x}) \tag{3.26}$$

Plug equations (3.24) and (3.26) into equation 3.20, the expression of the normal Peltier coefficient, we get

$$\begin{aligned} \Pi_{\text{normal}} &= \frac{\sum\limits_{\alpha,\boldsymbol{k}} v_{x,\boldsymbol{k}\alpha} (\varepsilon_{\boldsymbol{k}\alpha} - \varepsilon_f) \Delta f_{\boldsymbol{k}\alpha}}{\sum\limits_{\alpha,\boldsymbol{k}} (-e) v_{x,\boldsymbol{k}\alpha} \Delta f_{\boldsymbol{k}\alpha}} = \frac{\sum\limits_{\alpha,\boldsymbol{k}} v_{x,\boldsymbol{k}\alpha} (\varepsilon_{\boldsymbol{k}\alpha} - \varepsilon_f) \Delta f_{\boldsymbol{k}\alpha}}{-\sigma N_k \Omega \frac{\partial \varphi}{\partial x}} \\ &= \frac{\sum\limits_{\alpha,\boldsymbol{k}} e\tau_{\boldsymbol{k}\alpha} v^2_{x,\boldsymbol{k}\alpha} (\varepsilon_{\boldsymbol{k}\alpha} - \varepsilon_f) \frac{\partial f^0_{\boldsymbol{k}\alpha}}{\partial \varepsilon}}{\sigma N_k \Omega} \end{aligned} \tag{3.27}$$

This is exactly what we got in equation (3.8) if divided it by T, as σ is given by plugging equation (3.4) into equation (3.5), which proves the second Thomson relation $\Pi = TS$ mentioned in chapter 1.

To figure out the phonon drag part,

$$\Pi_{\text{phonon drag}} = \frac{\frac{1}{N_q} \sum\limits_{\lambda,\boldsymbol{q}} \hbar\omega_{\boldsymbol{q}\lambda} v_{x,\boldsymbol{q}\lambda} \tau_{\boldsymbol{q}\lambda} \left(\frac{\partial n_{\boldsymbol{q}\lambda}}{\partial t} \right)_{\text{e-ph}}}{\frac{1}{N_k} \sum\limits_{\alpha,\boldsymbol{k}} (-e) v_{x,\boldsymbol{k}\alpha} \Delta f_{\boldsymbol{k}\alpha}} \tag{3.28}$$

we need to start again from counting the possible scattering events relating to the

phonon with wavevector q at branch λ to determine the $\left(\frac{\partial n_{q\lambda}}{\partial t}\right)_{\text{e-ph}}$ term. Slightly different from equation (2.40), here we need a factor of 2 as we need to count in consistency with the electron case above (count the events according to Table 2.2 instead of Table 2.3), and represent the emission and absorption rate elements as N_{emit} and N_{absorb} that are given in equation (2.41).

$$\left(\frac{\partial n_{q\lambda}}{\partial t}\right)_{\text{e-ph}} = \frac{2}{N_k}\frac{2\pi}{\hbar}\sum_{\alpha,\beta}\sum_{\boldsymbol{k},\boldsymbol{k}'}\Big[+f_{\boldsymbol{k}\alpha}(1-f_{\boldsymbol{k}'\beta})(n_\lambda+1)N_{emit} \\ - f_{\boldsymbol{k}\alpha}(1-f_{\boldsymbol{k}'\beta})n_\lambda N_{absorb}\Big] \tag{3.29}$$

Noticing the summations of α and β are over the same possible electronic bands so they are equivalent, same as $\boldsymbol{k}$ and $\boldsymbol{k}'$, we can switch α with β and $\boldsymbol{k}$ with $\boldsymbol{k}'$ at the same time in N_{absorb} to combine N_{emit} and N_{absorb} terms. Again, we will use the Bose-Einstein distribution $n^0_{q\lambda}$ for phonon's distribution $n_{q\lambda}$ and also neglect the $\Delta f_{\boldsymbol{k}\alpha}\Delta f_{\boldsymbol{k}'\beta}$ term as a first-order approximation.

From equation (3.24), we can write

$$\Delta f_{\boldsymbol{k}\alpha} = -e\tau_{\boldsymbol{k}\alpha}v_{x,\boldsymbol{k}\alpha}\frac{\partial f^0_{\boldsymbol{k}\alpha}}{\partial\varepsilon}\frac{\partial\varphi}{\partial x} \tag{3.30}$$

$$\Delta f_{\boldsymbol{k}'\beta} = -e\tau_{\boldsymbol{k}'\beta}v_{\boldsymbol{k}'\beta,x}\frac{\partial f^0_{\boldsymbol{k}'\beta}}{\partial\varepsilon}\frac{\partial\varphi}{\partial x} \tag{3.31}$$

again using $\frac{\partial f^0}{\partial\varepsilon} = \frac{1}{k_BT}f^0(1-f^0)$, after some algebra, equation (3.29) is rearranged to

$$\begin{aligned}\left(\frac{\partial n_{q\lambda}}{\partial t}\right)_{\text{e-ph}} &= \frac{4\pi}{\hbar N_k}\sum_{\alpha,\beta}\sum_{\boldsymbol{k},\boldsymbol{k}'}\left(\frac{\hbar}{2m_0\omega_{\boldsymbol{q}\lambda}}\right)|\langle\boldsymbol{k}'\beta|\partial_{\boldsymbol{q}\lambda}V|\boldsymbol{k}\alpha\rangle|^2\delta(\boldsymbol{k}-\boldsymbol{k}'-\boldsymbol{q}) \\ &\quad \delta(\varepsilon_{\boldsymbol{k}\alpha}-\varepsilon_{\boldsymbol{k}'\beta}-\hbar\omega_{\boldsymbol{q}\lambda})[\Delta f_{\boldsymbol{k}\alpha}(n^0_{\boldsymbol{q}\lambda}+1-f^0_{\boldsymbol{k}'\beta})-\Delta f_{\boldsymbol{k}'\beta}(n^0_{\boldsymbol{q}\lambda}+f^0_{\boldsymbol{k}\alpha})] \\ &= \frac{4\pi e\frac{\partial\varphi}{\partial x}}{\hbar N_k k_BT}\sum_{\alpha,\beta}\sum_{\boldsymbol{k},\boldsymbol{k}'}\left(\frac{\hbar}{2m_0\omega_{\boldsymbol{q}\lambda}}\right)|\langle\boldsymbol{k}'\beta|\partial_{\boldsymbol{q}\lambda}V|\boldsymbol{k}\alpha\rangle|^2\delta(\boldsymbol{k}-\boldsymbol{k}'-\boldsymbol{q}) \\ &\quad \delta(\varepsilon_{\boldsymbol{k}\alpha}-\varepsilon_{\boldsymbol{k}'\beta}-\hbar\omega_{\boldsymbol{q}\lambda})[(\tau_{\boldsymbol{k}\alpha}v_{x,\boldsymbol{k}\alpha}-\tau_{\boldsymbol{k}'\beta}v_{x,\boldsymbol{k}'\beta})(1-f^0_{\boldsymbol{k}\alpha})f_{\boldsymbol{k}'\beta}n^0_{\boldsymbol{q}\lambda}]\end{aligned} \tag{3.32}$$

Now plug equation (3.32) into the expression of the phonon drag part of Peltier coefficient equation (3.28) with equation (3.26),

$$\Pi_{\text{phonon drag}} = \frac{4\pi e}{\sigma N_q N_k \Omega k_B T} \sum_{q\lambda} \tau_{q\lambda} v_{x,q\lambda} \omega_{q\lambda} \sum_{\alpha,\beta} \sum_{k,k'} \left(\frac{\hbar}{2m_0 \omega_{q\lambda}} \right) |\langle k'\beta | \partial_{q\lambda} V | k\alpha \rangle|^2$$
$$\delta(k - k' - q)\delta(\varepsilon_{k\alpha} - \varepsilon_{k'\beta} - \hbar\omega_{q\lambda})[(\tau_{k\alpha} v_{x,k\alpha} - \tau_{k'\beta} v_{x,k'\beta})(1 - f^0_{k\alpha}) f_{k'\beta} n^0_{q\lambda}] \quad (3.33)$$

With the second Thomson relation $\Pi_{\text{phonon drag}} = T S_{\text{phonon drag}}$, the phonon drag part of Seebeck is

$$S_{\text{phonon drag}} = \frac{4\pi e}{\sigma N_q N_k \Omega k_B T^2} \sum_{q\lambda} \tau_{q\lambda} v_{x,q\lambda} \omega_{q\lambda} \sum_{\alpha,\beta} \sum_{k,k'} \left(\frac{\hbar}{2m_0 \omega_{q\lambda}} \right) |\langle k'\beta | \partial_{q\lambda} V | k\alpha \rangle|^2$$
$$\delta(k - k' - q)\delta(\varepsilon_{k\alpha} - \varepsilon_{k'\beta} - \hbar\omega_{q\lambda})[(\tau_{k\alpha} v_{x,k\alpha} - \tau_{k'\beta} v_{x,k'\beta})(1 - f^0_{k\alpha}) f_{k'\beta} n^0_{q\lambda}] \quad (3.34)$$

Note that the $\Pi_{\text{phonon drag}}$ and $S_{\text{phonon drag}}$ above are derived along x-axis and they should have the same value along different directions for an isotropic material. While in our calculation, we calculate them as tensors and the values on the diagonal are substantially the same, which reflects the isotropy of the crystal structure of SiGe alloys.

3.3.2 Validation in Silicon

Before going to the calculated phonon drag results of SiGe alloys, we need to make sure that our method above is reliable. We validate our calculation of the two parts of Seebeck coefficient by reproducing Zhou et al.'s result for the Si case [32]. Our result of Si in figure 3-11 shows that by incorporating the phonon drag part of Seebeck coefficient, we are able to match our calculated Seebeck coefficient of silicon with the experimental data very well and thus we would like to expand this methodology to the cases of SiGe alloys.

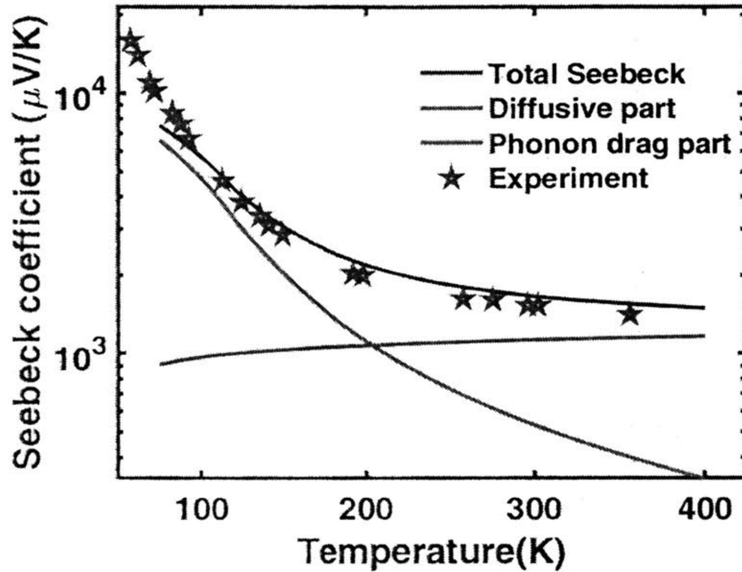

Figure 3-11: Seebeck coefficient of silicon ($n = 2.75 \times 10^{14}\,\mathrm{cm}^{-3}$) as a function of temperature. The experimental data is from [5].

3.3.3 SiGe Alloys Results

The calculated Seebeck coefficients of SiGe alloys at 300K and 150K are shown in figures 3-12. Our calculated total Seebeck coefficients show good agreement with the experimental data from Amith [6]. We notice several regions with interesting changes and we would like to explain several important features of the results in the respect of the trend.

According to equation (3.34), the expression of the phonon drag part of Seebeck, we know the phonon drag part of Seebeck is related to the phonon mean free path. As temperature goes lower, the intrinsic phonon scattering gets weaker, which means phonons will be able to travel longer distance before getting scattered, hence the phonon drag effect is more significant at low temperatures. As discussed in section 1.3, alloying might be able to filter the phonons that contribute more to the thermal conductivity while retaining the phonons that contribute to phonon drag. However, we found that alloy scattering is not that ideal in maintaining the phonon drag part

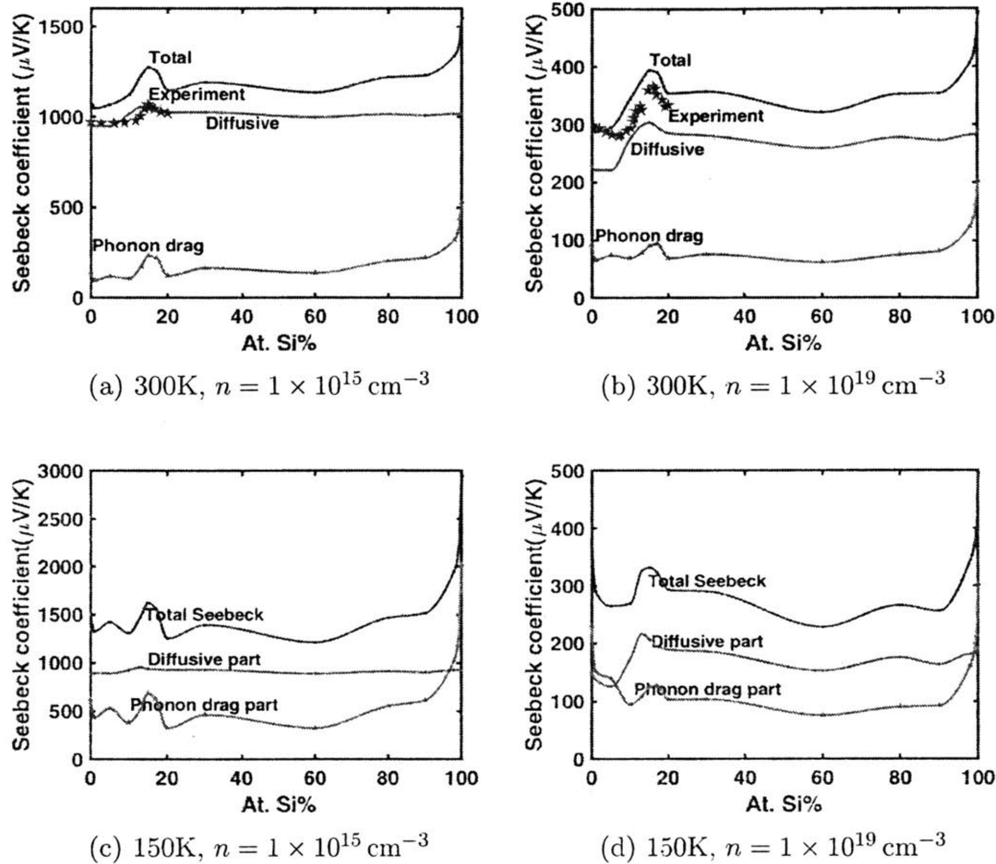

(a) 300K, $n = 1 \times 10^{15}\,\mathrm{cm}^{-3}$

(b) 300K, $n = 1 \times 10^{19}\,\mathrm{cm}^{-3}$

(c) 150K, $n = 1 \times 10^{15}\,\mathrm{cm}^{-3}$

(d) 150K, $n = 1 \times 10^{19}\,\mathrm{cm}^{-3}$

Figure 3-12: Calculated Seebeck coefficients of SiGe alloys vs. composition. The experimental data is from [6]. (a)(b)T = 300K, (c)(d) T =150K.

of Seebeck coefficient while suppressing thermal conductivity as the phonon drag part would also decrease with alloying in the the Si-rich and the Ge-rich regions. That is, though the mass disorder in alloys tends to scatter phonons with high frequency and short mean free path more, it is not having zero effect on phonons with low frequency and long mean path and it still scatters those phonons to a certain extent. Nonetheless, if we look closer, the degrees of influence on these two properties are different. For example, in the Si-rich region in figure 3-12a, when we add 10% Ge to pure Si, the total Seebeck coefficient drops to about three fourths of pure silicon's, while the thermal conductivity is almost an order of magnitude smaller than pure silicon's thermal conductivity (around $145\,W/mK$ at 300K at low carrier concentrations, the maximum of y-axis in figure 3-10 is set to $70\,W/mK$ to show SiGe alloys'

thermal conductivity more clearly) as shown in figure 3-10. By comparing figure 3-12a and figure 3-12b as well as figure 3-12c and figure 3-12d, we can see the phonon drag effect is less significant at high carrier concentration. This can be understood as that, as shown in figure 3-8, when the carrier concentration is high, the strong electron-phonon interaction would reduce the phonon mean free path and weaken the phonon drag effect.

Recall the expression of the diffusive Seebeck coefficient (equation (3.8)), the diffusive Seebeck coefficient is mostly determined by $\varepsilon - \varepsilon_f$, that is how much heat can an electron carry. At a fixed carrier concentration, Fermi level gets higher when the temperature gets lower. And at a given temperature, Fermi level gets higher with increasing carrier concentration. This explains the trend in the diffusive Seebeck coefficient with respect to the carrier concentration and the temperature.

As briefly mentioned in section 2.3 while discussing our calculated band structure (figure 2-1), another feature of alloying effect that is worth noticing is band convergence, which is shown in the region near the composition of $Si_{0.13}Ge_{0.87}$ (hereinafter band convergence region). As we know, Si and Ge have different band structures (shown in figure 2-1). Their conduction band minima are located at different valleys of the electronic band structure (germanium's is at L valley and silicon's is near X valley). When the two materials are being alloyed, their conduction bands start to cross over each other, and there will be a particular composition at which the two conduction band minima align with each other. At this point, the density of states at the conduction band minimum is the largest and there are more electron states available for free electrons which can participate both in the normal (diffusive) Seebeck effect and phonon drag effect, resulting in a peak in the Seebeck coefficient as shown in figure 3-12 in the band convergence region, which is also supported by the experimental data from Amith [6]. We can further justify this band convergence feature by plotting the density of states near the conduction band edge of SiGe alloys in this composition region (figure 3-13). It can be seen clearly that among our calculated compositions, the conduction band minima (the one at L point and the one

near X point) align with each other the best (according to the lower left subfigure in figure 2-1) and the density of states near conduction band edge becomes the largest at 13 At.Si%, which is in line with the peak in the Seebeck coefficient in the band convergence region shown in figure 3-12.

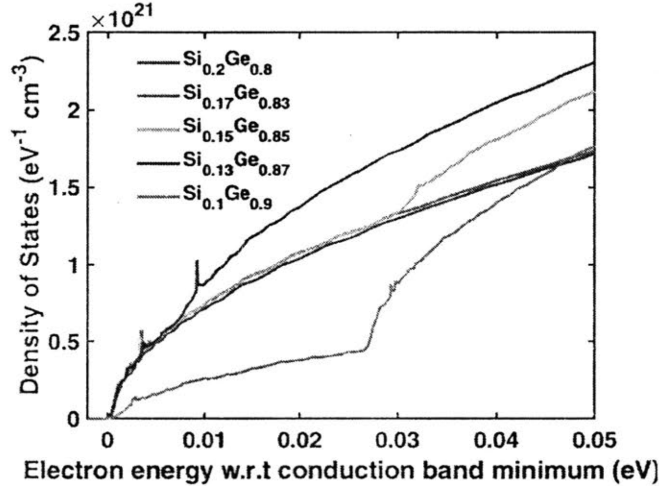

Figure 3-13: Density of states of SiGe alloys in the band convergence region. At $Si_{0.87}Ge_{0.13}$ the density of states is the highest.

3.3.4 Convergence Test Results

Every first-principles calculation is an approximate one given the physical approximations (e.g. Born-Oppenheimer, exchange-correlation functionals, relaxation time approximation, etc.) we have mentioned in chapter 2 as well as numerical approximations (e.g. basis-set size, integral evaluation cutoffs, sampling mesh density, iterative schemes: number of iterations and exit criteria, system size etc.) in real implementation. In fact, no first-principles calculation is ever fully-converged. This does not mean that first-principles calculations cannot provide reliable result or valuable insight. The appropriate numerical setting can be determined by means of a convergence test and calculations using current computing resource with accuracy comparable to experiment can be achieved.

We believe our choices in the size of supercell, the kinetic energy cut-off for wave-

functions, the convergence threshold for self-consistency and other parameters in our first-principles calculations have been set to the values that are good enough to capture the transport properties of SiGe alloys. Our major concern in terms of convergence lies in the k-mesh and q-mesh (introduced in section 2.1) sampling density. Theoretically, the denser the sampling mesh is, the more accurate the result will be. Limited by the computing power in hand, we cannot make our sampling k-mesh and q-mesh as dense as desired (e.g. $200 \times 200 \times 200$). However, most of time, a relatively dense mesh (e.g. $80 \times 80 \times 80$) can capture the major features well and provide reasonably converged results. In this section, we show our convergence test (mesh density from $30 \times 30 \times 30$ to $100 \times 100 \times 100$) on the q-mesh density used in ShengBTE package for the lattice thermal conductivity calculations, as well as the fine mesh density (both k-mesh and q-mesh) in Wannier interpolation for mobility calculations and Seebeck coefficients calculations.

The convergence test on the lattice thermal conductivity at low carrier concentrations (without considering electron-phonon interaction) at 300K and 150K is plotted in figure 3-14. It shows that for the lattice thermal conductivities of SiGe alloys, convergence is well guaranteed when the density of the mesh is denser than $60 \times 60 \times 60$ for the values actually change very little across the entire range of the mesh density we have tested.

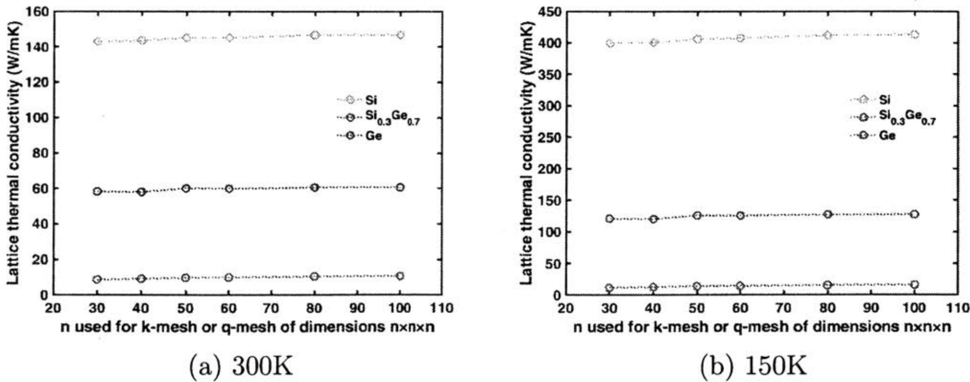

(a) 300K (b) 150K

Figure 3-14: Calculated lattice thermal conductivity vs. sampling mesh density

The convergence test on calculated mobility, diffusive part of Seebeck coefficient

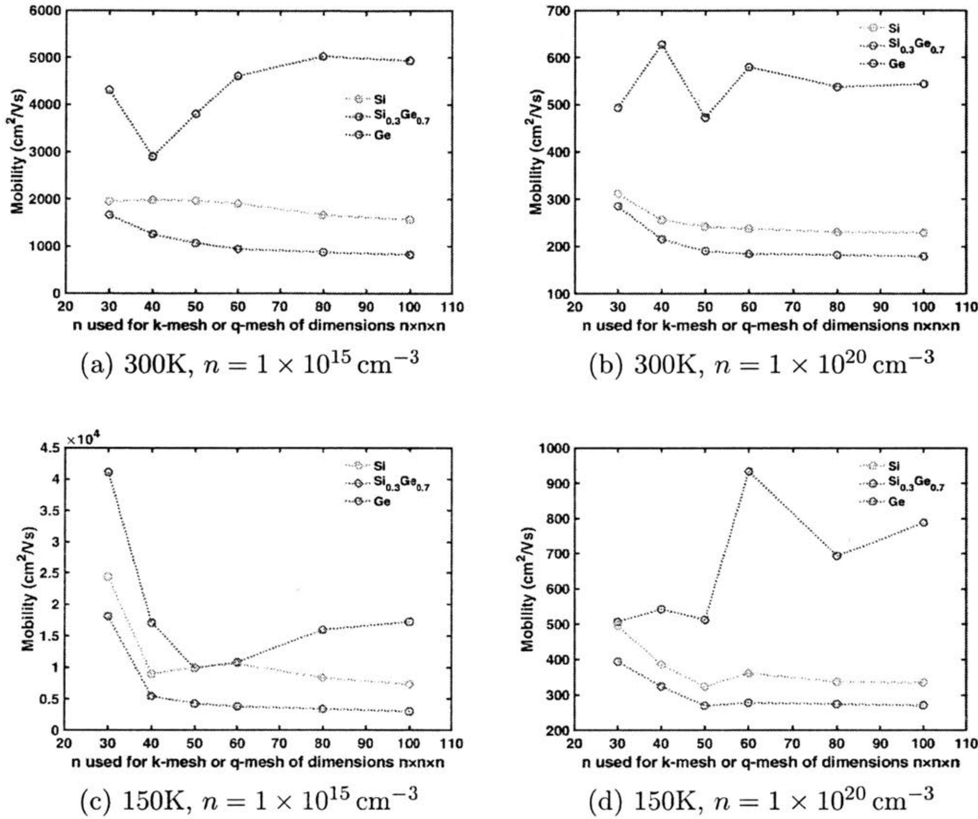

(a) 300K, $n = 1 \times 10^{15}\,\mathrm{cm}^{-3}$

(b) 300K, $n = 1 \times 10^{20}\,\mathrm{cm}^{-3}$

(c) 150K, $n = 1 \times 10^{15}\,\mathrm{cm}^{-3}$

(d) 150K, $n = 1 \times 10^{20}\,\mathrm{cm}^{-3}$

Figure 3-15: Calculated mobility vs. sampling mesh density for lightly doped and heavily doped SiGe alloys. (a)(b)T = 300K, (c)(d) T = 150K.

and the phonon drag part of Seebeck coefficient in figure 3-15, figure 3-16 and figure 3-17 show that the convergence in germanium's calculated electrical properties is harder to achieve, which might be due to the more complex band structure (compared to Si or $\mathrm{Si_{0.3}Ge_{0.7}}$, Ge has more valleys involved near the conduction band minimum as shown in figure 2-1), especially at low temperatures and high carrier concentrations when the Fermi level is entering the conduction band. Also, the convergence demand becomes more stringent at low temperatures for that the populated phonons are more centered around the Γ point, as well as that the populated electrons are more centered at the conduction band edge at low temperatures, thus denser sampling meshes are required to sufficiently capture phonons' information and electrons' information.

We use q-mesh of dimensions $60\times60\times60$ for our thermal conductivity calculations,

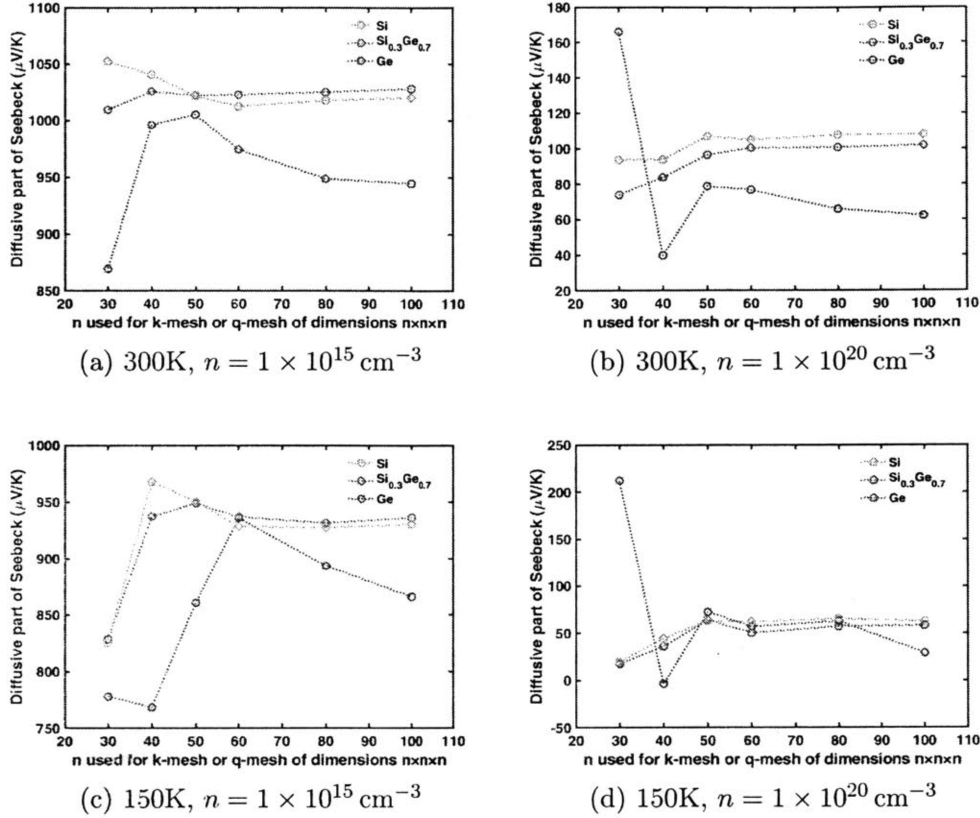

(a) 300K, $n = 1 \times 10^{15}\,\mathrm{cm}^{-3}$

(b) 300K, $n = 1 \times 10^{20}\,\mathrm{cm}^{-3}$

(c) 150K, $n = 1 \times 10^{15}\,\mathrm{cm}^{-3}$

(d) 150K, $n = 1 \times 10^{20}\,\mathrm{cm}^{-3}$

Figure 3-16: Calculated diffusive part of Seebeck coefficient vs. sampling mesh density for lightly doped and heavily doped SiGe alloys. (a)(b)T = 300K, (c)(d) T = 150K.

k-mesh and q-mesh both of dimensions $80 \times 80 \times 80$ for the calculations of mobility and Seebeck coefficients. In short, the convergence test results show that the calculated thermoelectric properties obtained with our chosen mesh densities in the previous sections should be reliable in terms of convergence.

3.4 Thermoelectric Figure of Merit

As given in section 1.1, the dimensionless figure of merit $zT = \frac{S^2 \sigma T}{\kappa}$ is directly related to the maximum energy conversion efficiency of the thermoelectric material. Now we have much confidence in our calculated thermal conductivity, electrical conductivity and Seebeck coefficients based on the discussion in the previous sections, we would

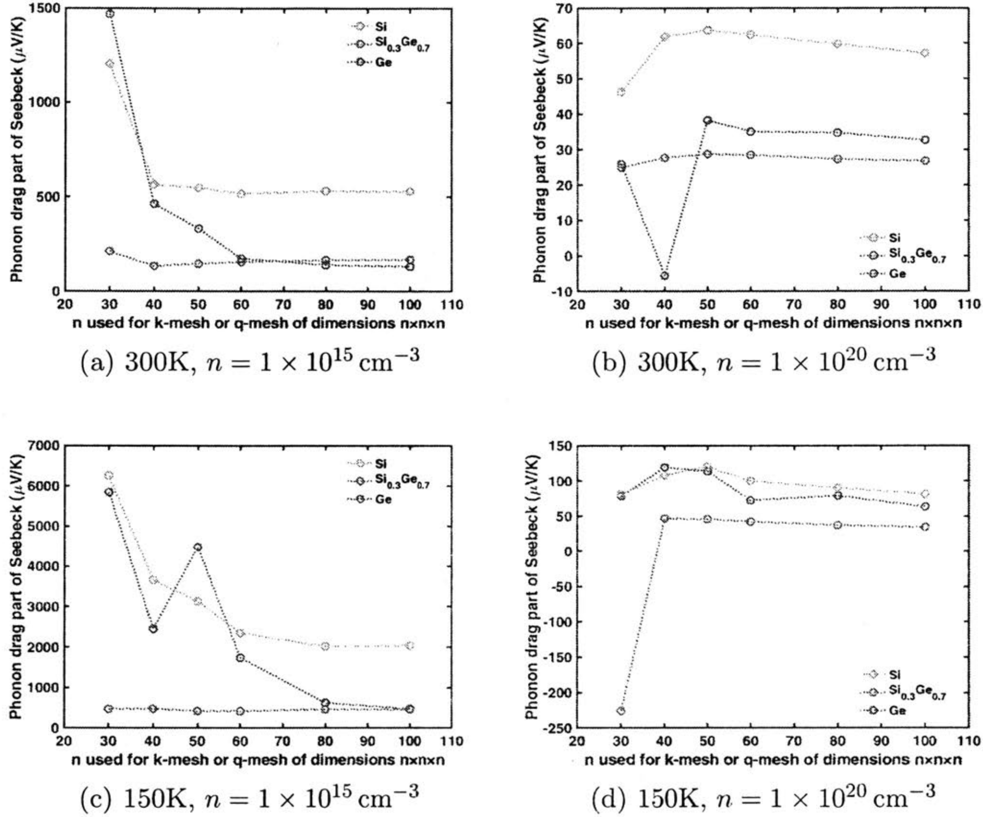

(a) 300K, $n = 1 \times 10^{15}\,\mathrm{cm}^{-3}$ (b) 300K, $n = 1 \times 10^{20}\,\mathrm{cm}^{-3}$

(c) 150K, $n = 1 \times 10^{15}\,\mathrm{cm}^{-3}$ (d) 150K, $n = 1 \times 10^{20}\,\mathrm{cm}^{-3}$

Figure 3-17: Calculated phonon drag part of Seebeck coefficient vs. sampling mesh density for lightly doped and heavily doped SiGe alloys. (a)(b)T = 300K, (c)(d) T = 150K.

like to put our results above together, calculate the zTs and examine the thermoelectric performance of n-type SiGe alloys at different carrier concentrations (from $n = 1 \times 10^{15}\,\mathrm{cm}^{-3}$ to $1 \times 10^{20}\,\mathrm{cm}^{-3}$) over the complete range of compositions at low temperature (150K) and room temperature (300K).

We further plot the power factor and the thermal conductivity along with the figure of merit in figure 3-19 for heavily doped SiGe alloys at 300K and 150K, in both cases where we consider phonon drag and do not consider phonon drag. From the comparison between the two cases, we conclude that phonon drag effect contributes significantly to SiGe alloys' thermoelectric performance and it is essential to include it while we are calculating the Seebeck coefficient.

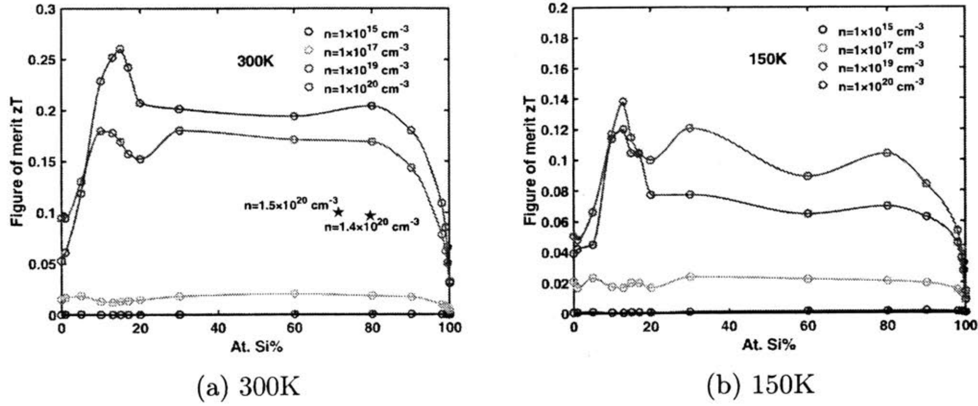

(a) 300K (b) 150K

Figure 3-18: Calculated zT values of SiGe alloys vs. composition at four different carrier concentrations. (a) T = 300K, the experimental data is from [3], (b) T = 150K.

As the carrier concentration gets higher, the lattice thermal conductivity would decrease while the electronic thermal conductivity would increase. We have shown in section 3.2 that the former effect is more important in SiGe alloys when the carrier concentration is not extremely high ($n <= 1 \times 10^{20}\,\mathrm{cm}^{-3}$). Though the mobility would decrease with increasing carrier concentration for the impurity scattering would get stronger, the electrical conductivity would still increase (the decrease in μ is less significant than the increase in n in equation 3.5). The Seebeck coefficient will be lower at higher carrier concentrations as discussed in section 3.3.3. Therefore, the trend in power factor $S^2\sigma$ and zT with respect to the carrier concentration cannot be described with a simple conclusion, and this is exactly why trial-and-error experiments on finding and optimizing alloy recipes for thermoelectric use are very time-consuming and first-principle studies are much need as guidelines. As the temperature goes lower, the Seebeck coefficient drops while the electrical conductivity increases as electrons are less scattered by phonon. The intrinsic phonon interaction gets weaker thus the lattice thermal conductivity increases. The degree of the changes in these properties varies with the temperature as well as the alloy composition that we cannot draw a simple universal conclusion saying one specific SiGe alloy compositions will have the best thermoelectric performance at all temperatures. And the results of our first-principles calculation shown in figure 3-18 and figure 3-19 can make the screening

and optimizing processes of the alloys' composition and doping concentration for thermometric use under different conditions much more efficient.

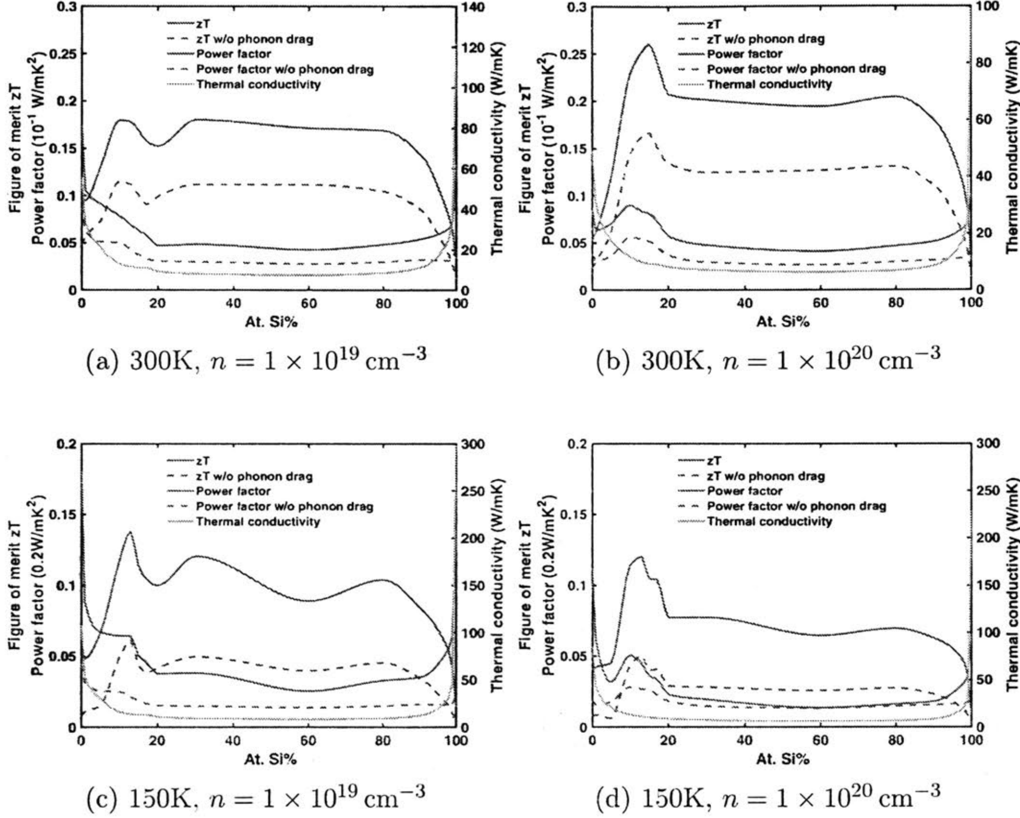

(a) 300K, $n = 1 \times 10^{19}\,\mathrm{cm}^{-3}$ (b) 300K, $n = 1 \times 10^{20}\,\mathrm{cm}^{-3}$

(c) 150K, $n = 1 \times 10^{19}\,\mathrm{cm}^{-3}$ (d) 150K, $n = 1 \times 10^{20}\,\mathrm{cm}^{-3}$

Figure 3-19: Calculated zT values of SiGe alloys vs. composition, at carrier concentration of $10^{19}\,\mathrm{cm}^{-3}$ and $10^{20}\,\mathrm{cm}^{-3}$, with and without phonon drag. (a)(b) T = 300K, (a)(b) T = 150K.

Taking all the factors of zT into account, our calculated results show that heavily doped SiGe alloys have much better thermoelectric performance than lightly doped SiGe alloys (this is mostly due to that the electrical conductivity gets much larger at high carrier concentrations). At 300K, an optimal zT value of 0.26 is obtained near the composition of $\mathrm{Si}_{0.15}\mathrm{Ge}_{0.85}$ with a carrier concentration of $10^{20}\,\mathrm{cm}^{-3}$. At 150K, an optimal zT value of 0.18 is obtained near the composition of $\mathrm{Si}_{0.1}\mathrm{Ge}_{0.9}$ with a carrier concentration of $10^{19}\,\mathrm{cm}^{-3}$.

The gap between our calculated figure of merit zT and the experimental data from Dismukes et al. should be mostly due to the existing error in our calculated

electron mobility, which has been discussed thoroughly in section 3.1.1. Our entire calculation is based on the virtual crystal approximation, which is only a first-order approximation. As discussed in section 1,4, it models alloy systems as homogeneous crystals and cannot capture many other disordered features in real alloy materials. This will definitely result in a certain amount of error in our calculations compared to the experiments. And we estimate that there might be an error of $5 - 20\%$ in our current results compared to the ideally converged results if denser meshes are allowed by computing power according our convergence test in section 3.3.4.

In conclusion, from the results we discussed above, combining phonon drag and alloying effect together is beneficial to thermoelectric performance.

Chapter 4

Summary and Future Work

4.1 Summary

In summary, we have presented the first-principles calculations of the Seebeck coefficients, electrical conductivity and thermal conductivity of n-type SiGe alloys with different carrier concentrations (from $10^{15}\,\mathrm{cm}^{-3}$ to $10^{20}\,\mathrm{cm}^{-3}$) over the complete range of compositions within virtual crystal approximation at 300K and 150K. In particular, we have included the phonon drag part contribution in our Seebeck calculation and taken both alloy scattering of phonons and alloy scattering of electrons into account.

We found that phonon drag effect contributes significantly to the total Seebeck coefficient in SiGe alloys, especially at lower temperatures. The band convergence happens around the composition of $Si_{0.13}Ge_{0.87}$. As a result, there are peaks both in the normal(diffusive) part of Seebeck coefficient and the phonon drag part of Seebeck coefficient. However, the mobility is low in this region due to stronger electron-phonon scattering and ionized impurity scattering for the aligned conduction band minima give a larger density of states.

Taking all the factors of zT into account, our calculated zT values show that

combining phonon drag and alloying effect together is beneficial to thermoelectric performance. Heavily doped SiGe alloys have much better thermoelectric performance than lightly doped ones. An optimal zT value around 0.26 is obtained near the composition of $Si_{0.15}Ge_{0.85}$ with a carrier concentration of $10^{20}\,cm^{-3}$ at 300K and an optimal zT value around 0.18 is obtained near the composition of $Si_{0.1}Ge_{0.9}$ with a carrier concentration of $10^{19}\,cm^{-3}$ at 150K.

4.2 Future Work

The agreement of our calculated results and reported experimental data validates the methodology that we have adopted and we would like to apply this methodology to other alloy systems of interest (e.g. BiSb alloys) in the future.

We are aware of the limitations of our approximations and possible errors that might exist in our calculations. For example, the band structure generated by DFT is not perfectly accurate, especially for the Ge-rich alloys. In the alloy-electron scattering calculations, only single scattering is considered and the after-scattering state is described as the undisturbed Bloch state of the periodic host lattice within the first Born approximation. The ionized impurity scattering is estimated using the Brooks-Herring model, which assigns electrons to plane-wave states and does not take the core scattering of ionized impurity into account. We found that the calculated optimal recipe of SiGe alloys as thermoelectric materials is sensitive to the calculated mobilities. Therefore, our next step is to work on obtaining more accurate band structure and better pictures of alloy-electron scattering and ionized impurity scattering to further improve the accuracy of our mobility calculations. Our entire work is based on the virtual crystal approximation, which is only a first-order approximation. It models alloy systems as homogeneous crystals and cannot capture many other disordered features in real alloy materials (e.g. vacancies, interstitial atoms and dislocations). We would like to include the effects of those defects in our future calculations.

Bibliography

[1] Niraj Kumar Singh, Juhi Pandey, Somnath Acharya, and Ajay Soni. Charge carriers modulation and thermoelectric performance of intrinsically p-type Bi_2Te_3 by Ge doping. *Journal of Alloys and Compounds*, 746:350–355, 2018.

[2] VI Fistul, MI Iglitsyn, and EM Omelyanovskii. Mobility of electrons in germanium strongly doped with arsenic, 1962.

[3] J P Dismukes, L Ekstrom, E F Steigmeier, I Kudman, and D S Beers. Thermal and Electrical Properties of Heavily Doped Ge-Si Alloys up to 1300°K. *Journal of Applied Physics*, 35, 1964.

[4] MC Steele and FD Rosi. Thermal conductivity and thermoelectric power of germanium-silicon alloys. *Journal of Applied Physics*, 29(11):1517–1520, 1958.

[5] T. H. Geballe and G. W. Hull. Seebeck effect in Silicon. *Physical Review*, 98(4):940–947, 1955.

[6] A. Amith. Seebeck coefficient in N-type germanium-silicon alloys: "competition" region. *Physical Review*, 139(5A):1624–1627, 1965.

[7] Thomas Johann Seebeck. Ueber die magnetische polarisation der metalle und erze durch temperaturdifferenz. *Annalen der Physik*, 82(3):253–286, 1826.

[8] JC Peltier. Nouvelles expériences sur la caloricité des courants électrique. *Ann. Chim. Phys*, 56(371):371–386, 1834.

[9] Lars Onsager. Reciprocal relations in irreversible processes. i. *Physical review*, 37(4):405, 1931.

[10] Herbert B Callen. The application of Onsager's reciprocal relations to thermoelectric, thermomagnetic, and galvanomagnetic effects. *Physical Review*, 73(11):1349, 1948.

[11] G Jeffrey Snyder and Eric S Toberer. Complex thermoelectric materials. *Nature Materials*, 7(2):105, 2008.

[12] AF Ioffe. Semiconductor thermoelements and thermoelectric cooling (infosearch, london, 1957). *Google Scholar*, page 146.

[13] George S Nolas, Jeffrey Sharp, and Julian Goldsmid. *Thermoelectrics: basic principles and new materials developments*, volume 45. Springer Science & Business Media, 2013.

[14] Lon E Bell. Cooling, heating, generating power, and recovering waste heat with thermoelectric systems. *Science*, 321(5895):1457–1461, 2008.

[15] AJ Minnich, MS Dresselhaus, ZF Ren, and G Chen. Bulk nanostructured thermoelectric materials: current research and future prospects. *Energy & Environmental Science*, 2(5):466–479, 2009.

[16] Joseph R Sootsman, Duck Young Chung, and Mercouri G Kanatzidis. New and old concepts in thermoelectric materials. *Angewandte Chemie International Edition*, 48(46):8616–8639, 2009.

[17] Conyers Herring. Theory of the thermoelectric power of semiconductors. *Physical Review*, 96(5):1163, 1954.

[18] Jun Kondo. Resistance minimum in dilute magnetic alloys. *Progress of theoretical physics*, 32(1):37–49, 1964.

[19] Peijie Sun, Beipei Wei, Jiahao Zhang, Jan M Tomczak, AM Strydom, M Søndergaard, Bo B Iversen, and Frank Steglich. Large Seebeck effect by charge-mobility engineering. *Nature communications*, 6:7475, 2015.

[20] Anton Tamtögl, Patrick Kraus, Nadav Avidor, Martin Bremholm, Ellen MJ Hedegaard, Bo B Iversen, Marco Bianchi, Philip Hofmann, John Ellis, William Allison, et al. Electron-phonon coupling and surface debye temperature of bi 2 te 3 (111) from helium atom scattering. *Physical Review B*, 95(19):195401, 2017.

[21] JL Cohn, SA Wolf, V Selvamanickam, and K Salama. Thermoelectric power of $YBa_2Cu_3O_{7-\delta}$: Phonon drag and multiband conduction. *Physical review letters*, 66(8):1098, 1991.

[22] Akram I Boukai, Yuri Bunimovich, Jamil Tahir-Kheli, Jen-Kan Yu, William A Goddard III, and James R Heath. Silicon nanowires as efficient thermoelectric materials. *Nature*, 451:168–171, 2008.

[23] Yew San Hor, A Richardella, Pedram Roushan, Yuqi Xia, Joseph G Checkelsky, A Yazdani, Md Zahid Hasan, NP Ong, and Robert Joseph Cava. p-type Bi_2Se_3 for topological insulator and low-temperature thermoelectric applications. *Physical Review B*, 79(19):195208, 2009.

[24] Hiromichi Ohta, SungWng Kim, Yoriko Mune, Teruyasu Mizoguchi, Kenji Nomura, Shingo Ohta, Takashi Nomura, Yuki Nakanishi, Yuichi Ikuhara, Masahiro Hirano, et al. Giant thermoelectric Seebeck coefficient of a two-dimensional electron gas in $SrTio_3$. *Nature materials*, 6(2):129, 2007.

[25] JM Ziman and Paul W Levy. Electrons and phonons. *Physics Today*, 14:64, 1961.

[26] HPR Frederikse. Thermoelectric power of germanium below room temperature. *Physical Review*, 92(2):248, 1953.

[27] M Bailyn. Transport in metals: effect of the nonequilibrium phonons. *Physical Review*, 112(5):1587, 1958.

[28] ME Brinson and W Dunstant. Thermal conductivity and thermoelectric power of heavily doped n-type silicon. *Journal of Physics C: Solid State Physics*, 3(3):483, 1970.

[29] Erwin Behnen. Quantitative examination of the thermoelectric power of n-type si in the phonon drag regime. *Journal of applied physics*, 67(1):287–292, 1990.

[30] DG Cantrell and PN Butcher. A calculation of the phonon-drag contribution to the thermopower of quasi-2d electrons coupled to 3d phonons. i. general theory. *Journal of Physics C: Solid State Physics*, 20(13):1985, 1987.

[31] GD Mahan, L Lindsay, and DA Broido. The Seebeck coefficient and phonon drag in silicon. *Journal of Applied Physics*, 116(24):245102, 2014.

[32] Jiawei Zhou, Bolin Liao, Bo Qiu, Samuel Huberman, Keivan Esfarjani, Mildred S Dresselhaus, and Gang Chen. Ab initio optimization of phonon drag effect for lower-temperature thermoelectric energy conversion. *Proceedings of the National Academy of Sciences*, 112(48):14777–14782, 2015.

[33] B. Abeles. Lattice Thermal Conductivity of Disordered Semiconductor Alloys at High Temperatures. *Physical Review*, 1046(1959), 1963.

[34] CM Bhandari and David M Rowe. CRC handbook of thermoelectrics. *CRC Press, Boca Raton, FL*, page 49, 1995.

[35] Yanzhong Pei, Heng Wang, and G J Snyder. Band Engineering of Thermoelectric Materials. *Advanced Materials*, 24(46):6125–6135, 2012.

[36] PG Klemens. Theory of phonon drag thermopower. In *Thermoelectrics, 1996., Fifteenth International Conference on*, pages 206–208. IEEE, 1996.

[37] Irving Weinberg. Phonon-drag thermopower in dilute copper alloys. *Physical Review*, 146(2):486, 1966.

[38] CC Lee and PA Schroeder. Phonon drag thermopower in silver alloys. *Philosophical Magazine*, 25(5):1161–1168, 1972.

[39] VA Matveev, GV Fedorov, and NV Volkenshtein. Thermoelectric power of pdmn alloys: the phonon-drag effect. *Zh. Eksp. Teor. Fiz*, 85:567, 1983.

[40] Alfred Levitas. Electrical properties of germanium-silicon alloys. *Physical Review*, 99(6):1810, 1955.

[41] Maurice Glicksman. Mobility of electrons in germanium-silicon alloys. *Physical Review*, 111(1):125, 1958.

[42] V. Joffe and A. F. Joffe. *Izv. Akad. Nauk SSSR Ser. Fiz.*, 20:1517–1520, 1956.

[43] B Abeles, DS S Beers, GD D Cody, and JP P Dismukes. Thermal conductivity of Ge-Si alloys at high temperatures. *Physical Review*, 125(1):44–46, 1962.

[44] HJ Goldsmid and AW Penn. Boundary scattering of phonons in solid solutions. *Physics Letters A*, 27(8):523–524, 1968.

[45] JE Parrott. The thermal conductivity of sintered semiconductor alloys. *Journal of Physics C: Solid State Physics*, 2(1):147, 1969.

[46] CM Bhandari and DM Rowe. Boundary scattering of phonons. *Journal of Physics C: Solid State Physics*, 11(9):1787, 1978.

[47] X. W. Wang, H. Lee, Y. C. Lan, G. H. Zhu, G. Joshi, D. Z. Wang, J. Yang, A. J. Muto, M. Y. Tang, J. Klatsky, S. Song, M. S. Dresselhaus, G. Chen, and Z. F. Ren. Enhanced thermoelectric figure of merit in nanostructured n -type silicon germanium bulk alloy. *Applied Physics Letters*, 93(19):1–4, 2008.

[48] Giri Joshi, Hohyun Lee, Yucheng Lan, Xiaowei Wang, Gaohua Zhu, Dezhi Wang, Ryan W Gould, Diana C Cuff, Ming Y Tang, Mildred S Dresselhaus, et al. Enhanced thermoelectric figure-of-merit in nanostructured p-type silicon germanium bulk alloys. *Nano letters*, 8(12):4670–4674, 2008.

[49] FD Rosi. Thermoelectricity and thermoelectric power generation. *Solid-State Electronics*, 11(9):833–868, 1968.

[50] Fred D Rosi. The research and development of silicon-germanium thermoelements for power generation. *MRS Online Proceedings Library Archive*, 234, 1991.

[51] C M Bhandarit and D M Rowe. Silicon-Germanium Alloys as High-Temperature Thermoelectric Materials. 21(3):219–242, 1980.

[52] DM Rowe. Recent advances in silicon-germanium alloy technology and an assessment of the problems of building the modules for a radioisotope thermoelectric generator. *Journal of power sources*, 19(4):247–259, 1987.

[53] C Wood. Materials for thermoelectric energy conversion. *Reports on progress in physics*, 51(4):459, 1988.

[54] JS Nelson, AF Wright, and CY Fong. First-principles virtual-crystal calculations of Al_xGa_{1-x} as disordered alloys and heterostructures: Band offsets and absolute alloy energies. *Physical Review B*, 43(6):4908, 1991.

[55] Jivtesh Garg, Nicola Bonini, Boris Kozinsky, and Nicola Marzari. Role of disorder and anharmonicity in the thermal conductivity of silicon-germanium alloys: A first-principles study. *Physical review letters*, 106(4):045901, 2011.

[56] Felipe Murphy-Armando and S. Fahy. First-principles calculation of alloy scattering in Ge_xSi_{1-x}. *Physical review letters*, 97(9):096606, 2006.

[57] Felipe Murphy-Armando and S Fahy. First-principles calculation of carrier-phonon scattering in n-type $Si_{1-x}Ge_x$ alloys. *Physical Review B*, 78(3):035202, 2008.

[58] Bolin Liao, Bo Qiu, Jiawei Zhou, Samuel Huberman, Keivan Esfarjani, and Gang Chen. Significant reduction of lattice thermal conductivity by the electron-phonon interaction in silicon with high carrier concentrations: A first-principles study. *Physical review letters*, 114(11):115901, 2015.

[59] Samuel Huberman, Vazrik Chiloyan, Ryan A Duncan, Lingping Zeng, Roger Jia, Alexei A Maznev, Eugene A Fitzgerald, Keith A Nelson, and Gang Chen. Unifying first-principles theoretical predictions and experimental measurements of size effects in thermal transport in SiGe alloys. *Physical Review Materials*, 1(5):054601, 2017.

[60] OD Restrepo, K Varga, and ST Pantelides. First-principles calculations of electron mobilities in silicon: Phonon and coulomb scattering. *Applied Physics Letters*, 94(21):212103, 2009.

[61] Bo Qiu, Zhiting Tian, Ajit Vallabhaneni, Bolin Liao, Jonathan M Mendoza, Oscar D Restrepo, Xiulin Ruan, and Gang Chen. First-principles simulation of electron mean-free-path spectra and thermoelectric properties in silicon. *EPL (Europhysics Letters)*, 109(5):57006, 2015.

[62] Wu Li. Electrical transport limited by electron-phonon coupling from boltzmann transport equation: An ab initio study of si, al, and mos 2. *Physical Review B*, 92(7):075405, 2015.

[63] Bolin Liao, Jiawei Zhou, Bo Qiu, Mildred S Dresselhaus, and Gang Chen. Ab initio study of electron-phonon interaction in phosphorene. *Physical Review B*, 91(23):235419, 2015.

[64] Te-Huan Liu, Jiawei Zhou, Bolin Liao, David J Singh, and Gang Chen. First-principles mode-by-mode analysis for electron-phonon scattering channels and mean free path spectra in gaas. *Physical Review B*, 95(7):075206, 2017.

[65] Te-Huan Liu, Bai Song, Laureen Meroueh, Zhiwei Ding, Qichen Song, Jiawei Zhou, Mingda Li, and Gang Chen. Simultaneously high electron and hole mobilities in cubic boron-V compounds: BP, BAs, and BSb. *Physical Review B*, 98(8):081203, 2018.

[66] Lars Hedin. New method for calculating the one-particle Green's function with application to the electron-gas problem. *Physical Review*, 139(3A):A796, 1965.

[67] Jack Deslippe, Georgy Samsonidze, David A Strubbe, Manish Jain, Marvin L Cohen, and Steven G Louie. Berkeleygw: A massively parallel computer package for the calculation of the quasiparticle and optical properties of materials and nanostructures. *Computer Physics Communications*, 183(6):1269–1289, 2012.

[68] Lothar Nordheim. Zur elektronentheorie der metalle. i. *Annalen der Physik*, 401(5):607–640, 1931.

[69] JA Van Vechten and TK Bergstresser. Electronic structures of semiconductor alloys. *Physical Review B*, 1(8):3351, 1970.

[70] Shin-ichiro Tamura. Isotope scattering of dispersive phonons in Ge. *Physical Review B*, 27(2):858, 1983.

[71] Jonathan Mendoza, Keivan Esfarjani, and Gang Chen. An ab initio study of multiple phonon scattering resonances in silicon germanium alloys. *Journal of Applied Physics*, 117(17):174301, 2015.

[72] Paolo Giannozzi, Stefano Baroni, Nicola Bonini, Matteo Calandra, Roberto Car, Carlo Cavazzoni, Davide Ceresoli, Guido L Chiarotti, Matteo Cococcioni, Ismaila Dabo, et al. Quantum espresso: a modular and open-source software project for quantum simulations of materials. *Journal of physics: Condensed matter*, 21(39):395502, 2009.

[73] Bassano Vacchini and Klaus Hornberger. Quantum linear Boltzmann equation. *Physics Reports*, 478(4-6):71–120, 7 2009.

[74] Gang Chen. *Nanoscale energy transport and conversion: a parallel treatment of electrons, molecules, phonons, and photons.* Oxford University Press, 2005.

[75] L.D. Landau and E.M. Lifshitz. *Quantum Mechanics*, volume chapter 6. Pergamon Press, Oxford, 1977.

[76] Joseph Callaway. Model for lattice thermal conductivity at low temperatures. *Physical Review*, 113(4):1046, 1959.

[77] John C Slater. Note on hartree's method. *Physical Review*, 35(2):210, 1930.

[78] Vladimir Fock. Näherungsmethode zur lösung des quantenmechanischen mehrkörperproblems. *Zeitschrift für Physik*, 61(1-2):126–148, 1930.

[79] Douglas Rayner Hartree. The calculation of atomic structures. 1957.

[80] Douglas R Hartree. The wave mechanics of an atom with a non-coulomb central field. part i. theory and methods. In *Mathematical Proceedings of the Cambridge Philosophical Society*, volume 24, pages 89–110. Cambridge University Press, 1928.

[81] Werner Heisenberg. Mehrkörperproblem und resonanz in der quantenmechanik. *Zeitschrift für Physik*, 38(6-7):411–426, 1926.

[82] Paul Adrien Maurice Dirac. On the theory of quantum mechanics. *Proc. R. Soc. Lond. A*, 112(762):661–677, 1926.

[83] Pierre Hohenberg and Walter Kohn. Inhomogeneous electron gas. *Physical review*, 136(3B):B864, 1964.

[84] Walter Kohn and Lu Jeu Sham. Self-consistent equations including exchange and correlation effects. *Physical review*, 140(4A):A1133, 1965.

[85] Hendric J Monkhorst. Hj monkhorst and jd pack, phys. rev. b 13, 5188 (1976). *Phys. Rev. B*, 13:5188, 1976.

[86] NE Zein. Non-local approximation for the exchange part of the density functional. *Journal of Physics C: Solid State Physics*, 17(12):2107, 1984.

[87] Stefano Baroni, Paolo Giannozzi, and Andrea Testa. Greens-function approach to linear response in solids. *Physical Review Letters*, 58(18):1861, 1987.

[88] Xavier Gonze. Adiabatic density-functional perturbation theory. *Physical Review A*, 52(2):1096, 1995.

[89] Stefano Baroni, Stefano De Gironcoli, Andrea Dal Corso, and Paolo Giannozzi. Phonons and related crystal properties from density-functional perturbation theory. *Reviews of Modern Physics*, 73(2):515, 2001.

[90] Xavier Gonze and Changyol Lee. Dynamical matrices, born effective charges, dielectric permittivity tensors, and interatomic force constants from density-functional perturbation theory. *Physical Review B*, 55(16):10355, 1997.

[91] Gregory H Wannier. The structure of electronic excitation levels in insulating crystals. *Physical Review*, 52(3):191, 1937.

[92] N.W. Ashcroft and N.D. Mermin. *Solid State Physics*. HRW international editions. Holt, Rinehart and Winston, 1976.

[93] Nicola Marzari, Arash A Mostofi, Jonathan R Yates, Ivo Souza, and David Vanderbilt. Maximally localized Wannier functions: Theory and applications. *Reviews of Modern Physics*, 84(4):1419, 2012.

[94] Walter Kohn. Localized basis for lattice vibrations. *Physical Review B*, 7(6):2285, 1973.

[95] Feliciano Giustino and Alfredo Pasquarello. Mixed wannier-bloch functions for electrons and phonons in periodic systems. *Physical review letters*, 96(21):216403, 2006.

[96] Feliciano Giustino, Marvin L Cohen, and Steven G Louie. Electron-phonon interaction using Wannier functions. *Physical Review B*, 76(16):165108, 2007.

[97] Samuel Poncé, Elena R Margine, Carla Verdi, and Feliciano Giustino. Epw: Electron–phonon coupling, transport and superconducting properties using maximally localized Wannier functions. *Computer Physics Communications*, 209:116–133, 2016.

[98] Arash A Mostofi, Jonathan R Yates, Young-Su Lee, Ivo Souza, David Vanderbilt, and Nicola Marzari. wannier90: A tool for obtaining maximally-localised wannier functions. *Computer physics communications*, 178(9):685–699, 2008.

[99] Ph Lambin and JP Vigneron. Computation of crystal Green's functions in the complex-energy plane with the use of the analytical tetrahedron method. *Physical Review B*, 29(6):3430, 1984.

[100] PA Flinn. Electronic theory of local order. *Physical Review*, 104(2):350, 1956.

[101] George L Hall. Nordheim's theory of the resistivity of alloys. *Physical Review*, 116(3):604, 1959.

[102] Arlyn E Asch and George L Hall. Quantum theory of the residual electrical resistivity of disordered alloys. *Physical Review*, 132(3):1047, 1963.

[103] JW Harrison and JR Hauser. Alloy scattering in ternary III-V compounds. *Physical Review B*, 13(12):5347, 1976.

[104] F Murphy-Armando and S Fahy. First-principles calculation of carrier-phonon scattering in n-type $Si_{1-x}Ge_x$ alloys.

[105] E Conwell and VF Weisskopf. Theory of impurity scattering in semiconductors. *Physical review*, 77(3):388, 1950.

[106] H Brooks. Scattering by ionized impurities in semiconductors. In *Physical Review*, volume 83, pages 879–879. AMERICAN PHYSICAL SOC ONE PHYSICS ELLIPSE, COLLEGE PK, MD 20740-3844 USA, 1951.

[107] Mark Lundstrom. *Fundamentals of carrier transport.* Cambridge university press, 2009.

[108] D Chattopadhyay and HJ Queisser. Electron scattering by ionized impurities in semiconductors. *Reviews of Modern Physics*, 53(4):745, 1981.

[109] Gyaneshwar P Srivastava. *The physics of phonons.* CRC press, 1990.

[110] Wu Li, Jesús Carrete, Nebil A Katcho, and Natalio Mingo. Shengbte: A solver of the boltzmann transport equation for phonons. *Computer Physics Communications*, 185(6):1747–1758, 2014.

[111] Keivan Esfarjani, Gang Chen, and Harold T Stokes. Heat transport in silicon from first-principles calculations. *Physical Review B*, 84(8):085204, 2011.

[112] PG Klemens. The scattering of low-frequency lattice waves by static imperfections. *Proceedings of the Physical Society. Section A*, 68(12):1113, 1955.

[113] Anupam Kundu, Natalio Mingo, DA Broido, and DA Stewart. Role of light and heavy embedded nanoparticles on the thermal conductivity of SiGe alloys. *Physical Review B*, 84(12):125426, 2011.

[114] HBG Casimir. Note on the conduction of heat in crystals. *Physica*, 5(6):495–500, 1938.

[115] T. H. Geballe and G. W. Hull. Seebeck effect in Germanium. *Physical Review*, 94(5):1134–1140, 1954.

[116] Karl Hess. Advanced theory of semiconductor devices. 2000.

[117] Lyman Spitzer Jr and Richard Härm. Transport phenomena in a completely ionized gas. *Physical Review*, 89(5):977, 1953.

[118] Joachim Appel. Electron-electron scattering and transport phenomena in nonpolar semiconductors. *Physical Review*, 122(6):1760, 1961.

[119] RT Bate, RD Baxter, FJ Reid, and AC Beer. Conduction electron scattering by ionized donors in insb at 80 K. *Journal of Physics and Chemistry of Solids*, 26(8):1205–1214, 1965.